THÈSE DE DOCTORAT
DE L'UNIVERSITÉ PIERRE ET MARIE CURIE

Specialité : Physique

École doctorale : «ED 564 Physique en Île-de-France»

réalisée au

Département de physique de l'École Normale Supérieure
Laboratoire Kastler Brossel

présentée par

Simeon Leander HOHMANN

pour obtenir le grade de :

DOCTEUR DE L'UNIVERSITÉ PIERRE ET MARIE CURIE

Sujet de la thèse :

Using optical fibre cavities to create multi-atom entanglement by quantum Zeno dynamics

soutenue le 24 février 2015

devant le jury composé de :

M.	Claude Fabre	Président
M.	Carsten Klempt	Rapporteur
M.	Sébastien Tanzilli	Rapporteur
M.	Gerhard Birkl	Examinateur
M.	Augusto Smerzi	Examinateur
M.	Jakob Reichel	Directeur de thèse

Résumé

Nous démontrons la création d'états intriqués dans un ensemble d'atomes neutres fondée sur la dynamique Zénon quantique (QZD), à l'aide d'un microrésonateur optique. Notre dispositif expérimental combine une puce à atomes avec une cavité Fabry-Perot fibrée (FFP) et nous permet de piéger un ensemble d'atomes de ^{87}Rb dans un seul ventre d'un piège dipolaire créé dans la cavité. Les atomes sont couplés fortement et identiquement au mode lumineux de la cavité, ce qui permet une mesure non-destructive de leur état collectif.

Nous réalisons la QZD en modifiant, par des mesures fréquentes, la dynamique induite par radiation micro-ondes. Nous démontrons que la QZD créé des états intriqués multiparticules de façon déterministe et rapide. Nous caractérisons ces états à l'aide de mesures de la fonction de Husimi Q, donnant accès à la partie symétrique de la matrice densité. Nous étudions l'évolution temporelle d'états impliquant un minimum de 3 à 11 atomes intriqués, qui présentent une fidélité par rapport à l'état W à 36 atomes atteignant 0.37. Nous étudions l'influence de la force de la mesure et des imperfections expérimentales et nous montrons que notre système est bien décrit par des modèles simples sans paramètres ajustables.

Nous présentons aussi un travail réalisé en vue de l'amélioration des cavités FFP. Nous discutons notamment la limitation due à l'écart en fréquence des modes propres de polarisation dans des cavités formées par deux fibres optiques microfabriquées avec un laser CO_2. Nous démontrons que cet effet dépend de la symétrie des structures microfabriquées et qu'il peut être contrôlé tant au niveau de la fabrication que pendant l'assemblage de la cavité.

Abstract

In this thesis, we show how an optical microcavity setup can create multiparticle entanglement in an ensemble of neutral atoms by means of quantum Zeno dynamics (QZD).

Our setup combines an atom chip with a fibre Fabry-Perot (FFP) resonator and allows us to load an ensemble of ^{87}Rb atoms into a single node of an intracavity dipole trap, coupling the atoms strongly and identically to the cavity light field which enables us to perform a quantum non-destructive measurement of their collective state.

We realise QZD by modifying the dynamics of the collective state (encoded in atomic hyperfine states addressed with MW radiation) by means of frequent cavity measurements at optical frequency. This QZD is shown to create multiparticle entanglement in a fast and deterministic scheme. To analyse the created states, we reconstruct the symmetric part of the atomic density matrix from 2d measurements of the ensemble's Husimi Q-distribution. We give a time-resolved account of the creation of states with at least 3-11 entangled atoms and fidelity of up to 0.37 with respect to a W state of 36 atoms. Studying the influence of measurement strength and experimental imperfections, we show that our experiments are well described by simple models with no free parameters.

This thesis also presents work towards improved FFP cavities. We discuss the problem of frequency splitting of polarisation eigenmodes in cavities made from two fibres microfabricated with a CO_2 laser. We show that this effect depends on the symmetry of the microfabricated structures and demonstrate that it can be controlled both at the level of fabrication and when assembling a cavity.

Contents

Introduction

The 20th century brought the fundamental insight that, on very small scales, nature behaves very differently from what we are used to in our macroscopic lives. Studied on the scale of single particles, light and matter - the basic elements describing the macroscopic physical world - have proven to be strange and unintuitive to our classical minds. We ascribe these observations to the fact that these two building blocks only come in certain quanta and describe this microscopically granular world through the framework of quantum physics.

Quantum physics has been at the heart of several of the developments that have shaped our world in the last decades [1]: semiconductor technology has enabled the computer revolution, lasers and associated optical devices have transformed information and telecommunication technology, atomic clocks allow us to measure time with unprecedented accuracy, effects at the quantum level are the basis for most definitions in the new SI system of units.

The main challenge to harnessing the power of quantum systems is to obtain strong control over their state while at the same time isolating them from the influence of the environment that tends to drown out the non-classical behaviour in most cases. To control the interaction between quantum matter and light, powerful experimental techniques have been developed, one of them being the use of a resonator. Purcell predicted in 1946 that the spontaneous decay of an atom can be modified by placing it in a cavity [2]. The cavity mirrors change the mode structure of the electromagnetic field inside the resonator which changes the decay channels to which the atom is coupled. This concept of tailoring and amplifying the interaction between matter and light is the basis for the research field of cavity quantum electrodynamics (cQED). Designing the cavity in a way that reduces the losses induced by the mirrors while increasing the coupling between light and atom leads to the strong coupling regime of cQED where coherent energy exchange between atom and light field is faster than all loss processes. This situation has been implemented in the microwave domain to enable remarkable experiments [1], ranging from the realisation of a two-photon maser [3] to the creation and active stabilisation of Fock field states [4]. Strong coupling in the optical domain [5, 6, 7] has been used to observe the trajectories of single atoms [8], create single photons on demand [9, 10] or to realise a light switch operated by a single atom [11]. Cavities are also used to manipulate trapped ions [12] and the strong coupling regime has been realised in other quantum systems such as superconducting qubits [13] or quantum dots [14]. These diverse efforts are echoed by the Nobel prize 2012 awarded (in part) to Serge Haroche "for ground-breaking experimental methods that enable measuring and manipulation of individual quantum systems".

1

Firm control over quantum systems allows one to study a particularly interesting phenomenon, entanglement. This term was introduced by Schrödinger [15, 16] to describe the fact that the state of two initially separate quantum systems that have interacted with each other, in general, can no longer be described in terms of the single systems. Instead, their state has become "interwoven" or entangled [17]. There exist numerous ideas to use the fundamentally non-classical character of entanglement for practical applications. Subsumed under the term quantum information technology, these developments promise advancements in several of today's key technological sectors:

- Quantum communication aims at transmitting information encoded in quantum states [18]. Using entangled states as information carriers allows communication protocols that are secure against manipulation as well as eavesdropping [19]. A major challenge is to develop means of relaying entanglement from one system to another to transport it over long distances [20].

- Quantum computing is centred around the idea of processing data not with classical bits (that are in one of two well-defined states) but with qubits that can be in superposition states [21]. In some applications, the increased information content available to quantum superpositions then allows higher performance than that of a classical computer. Computations are performed in quantum gate operations where individual qubits are entangled, or alternatively by preparing a multiparticle entangled resource state and performing measurements on it. In any case, the qubits need to be precisely manipulable, strongly isolated from disturbing influences of the environment and implemented so that their number is scalable.

- Quantum metrology improves the precision of interferometric measurements by exploiting the correlations present in multiparticle entangled quantum states [22]. The direction of the total effective spin of an ensemble of uncorrelated particles necessarily carries a minimum uncertainty which limits the accuracy achievable in a phase measurement. In entangled states, the spin uncertainty can be redistributed to produce higher sensitivity in the spin direction that is measured.

Since multiparticle entangled quantum states are a useful resource specifically for quantum computation and quantum metrology, significant effort is devoted to their creation and characterisation. Typical methods are based on unitary operations in an ensemble of quantum systems. These implementations can be based on addressing and manipulating individual qubits, for example ions in a linear Paul trap [23, 24**? **] or superconducting qubits [25, 26], or based on the evolution arising from collective interactions, leading to specific forms of entanglement such as spin-squeezing [27, 28, 29] or Dicke-like states [30].

In these schemes, entanglement is generated by coherent operations exclusively and coupling to the environment is, by all accounts, a detrimental influence that needs to be minimised as much as possible, or completely eliminated. However, recent research in quantum technology has shown that there exist complementary methods in which coupling to the environment can be a useful tool to create interesting quantum states. It has been shown theoretically that purely dissipative processes can be used to implement universal quantum computation [31] and to create multiparticle entangled states [32] when a number of quantum particles are connected to a set of environments with specifically engineered couplings. Experimentally, dissipative dynamics have been exploited to create squeezing in an atomic ensemble coupled to an optical cavity [33], to create EPR-type entanglement in two atomic ensembles [34], Bell and GHZ states in trapped ions [35, 36] and Bell states in superconducting qubits [37].

Quantum Zeno dynamics (QZD) is another intriguing example of the powerful forms of quantum dynamics that can arise from combining coherent manipulation and environment coupling. QZD is based on the fundamental phenomenon that in quantum physics, measuring frequently enough the state of a system can constrain its time evolution. This was first pointed out by Misra and Sudarshan who showed that a measurement that projects a quantum system back on its initial state can freeze it in place, even if the state is otherwise unstable, which they termed the quantum Zeno paradox [38]. However, when the measurement projects on a multidimensional subspace of the system's Hilbert space, the freezing gives way to dynamics which are restricted to the subspace but free within its boundaries. Adding a Zeno measurement to a regular coherent evolution, the system can reach quantum states that are inaccessible to the regular evolution alone. The resulting quantum Zeno dynamics has been studied theoretically for more than a decade [? ?]. Experimentally, it has been proposed for tailoring entangled states of a cavity light field [39]. QZD has been demonstrated in a BEC system with losses induced on a specific atomic state [40] and has been realised very recently in a single Rydberg atom [41], and with photons in a superconducting microwave cavity [42].

The experimental realisation of QZD is challenging since it requires measuring the state of a quantum system without disturbing or destroying it. In practice, such a non-demolition measurement is difficult to implement, given that it means coupling a microscopic quantum system to a macroscopic metre. Previous work in our group has demonstrated that we can perform a suitable non-demolition measurement in our experimental system, an ensemble of ultracold ^{87}Rb atoms coupled to a high finesse Fabry-Perot cavity [43, 44]. Our setup combines an atom chip with a fibre-based micro-resonator and allows us to load the atomic ensemble into a single node of an intracavity dipole trap, identically coupling the atoms to the cavity light field. The unique properties of the fibre Fabry-Perot cavity make it possible to achieve the strong coupling regime of cQED for each atom.

In this thesis, we use our atom chip/fibre cavity setup to implement QZD in an ensemble of several tens of atoms. The cavity serves to perform a non-destructive measurement of the collective atomic state which we combine with coherent collective rotations to realise QZD. Through suitable choice of the coherent evolution, the QZD leads to the creation of multiparticle entanglement in a fast and deterministic scheme. We can create different types of entangled states which we analyse by performing quantum state tomography based on a measurement of the atomic ensemble's Husimi Q-distribution. Extending this tomography technique (developed in [45]) to 2d enables us to give a time-resolved account of the entanglement generation. We also study the influence of the measurement strength and of imperfections in the experimental setup and find that our QZD is well described by simple models with no free parameters.

Based on these results, we demonstrate, to our knowledge for the first time, the creation of multiparticle entanglement via QZD and show that QZD can be a versatile, experimentally feasible tool for quantum engineering applications.

In addition, this thesis also presents work towards improving fibre Fabry-Perot (FFP) cavities. The FFP cavity at the heart of our current experimental setup is constructed from two optical fibres whose end facets have been microfabricated with a CO_2 laser. The fabrication process can create concave structures with parameters not achievable with macroscopic mirror substrates and makes it possible to build optical resonators with low losses, high finesse and small mode volume, which is the key to achieving strong coupling [46]. However, our current FFP cavity features two orthogonally polarised eigenmodes at different frequencies. This effect is detrimental to the experimental performance, limiting for example the purity of the entangled states created by QZD. On the way towards building an improved FFP setup, we have systematically investigated the origin of this frequency splitting. We have found that the effect depends on the symmetry of the concave structure and that it can be controlled both at the level of the microfabrication and when assembling a cavity made from two fibres. These insights inform current work performed in the group towards the realisation of next generation FFP resonators.

4

Outline

The first chapter presents the theoretical description of our experiments which realise quantum Zeno dynamics in an ensemble of trapped atoms strongly coupled to an optical cavity. We first consider a basic model describing QZD in a spin-$N/2$ system in which the dynamics of a unitary rotation is modified by an infinitely strong measurement of the collective state. We then develop a more realistic model, describing our system in a cQED framework with a finite-strength, non-destructive cavity-based measurement.

In the second chapter, we give a summary on the experimental setup and describe the steps to prepare a sample of ultra-cold atoms from a vapour at room temperature, load it into the intracavity dipole trap, and initialise it in a well-defined quantum state.

The third chapter details how we analyse the quantum state of the atomic ensemble. We show how a tomographic measurement of the ensemble's Husimi Q-distribution allows us to reconstruct its density matrix. We also present the two criteria used to characterise the entanglement properties of the corresponding multiparticle state.

The fourth chapter presents the preparation and characterisation of multiparticle entangled states by means of QZD. We first show the experimental sequence that leads to the creation of different entangled states and discuss the influence of experimental imperfections. We then present the results of our measurements, following the temporal evolution of the ensemble by means of 2d tomographic snapshots of its Q-distribution. The dynamics agree quantitatively with our models and the experimentally created states are shown to be entangled according to the criteria.

Chapter five is devoted to our investigation of the frequency splitting of polarisation modes in fibre Fabry-Perot cavities.

Finally, a conclusion summarises the main results and gives an outlook on future experiments.

Chapter 1

Quantum Zeno dynamics in an atomic ensemble

This chapter presents the basic concepts necessary to understand our experiments. We start with a brief description of quantum Zeno dynamics, showing how frequent measurements can partition the state space accessible to a quantum system (Section 1.1). Section 1.2 shows the most basic model that describes our QZD experiments, a spin-$N/2$ system in which the dynamics of a unitary rotation is modified by a measurement of the collective state. We finally show in Section 1.3 how we implement this model experimentally in an ensemble of cold atoms strongly coupled to an optical resonator. Specifically, we show how the cavity can be used to implement a strong, non-destructive measurement of the collective state of the atomic ensemble.

1.1 From Zeno's paradox to Quantum Zeno dynamics

To give an intuitive idea of the origin of quantum Zeno dynamics, we start this section with an elementary example of the quantum Zeno effect which we then extend towards a basic description of QZD. Our account of these phenomena will neglect the mathematical rigour which is a large point of the theoretical work devoted to them. Instead, we focus on a minimal description that is sufficient for the experimental considerations presented in the subsequent section. Our presentation follows the review in [47] which also contains ample references with a formally stringent approach.

1.1.1 The quantum Zeno effect

> "An unstable particle observed continuously whether it has decayed or not will *never* be found to decay! Since this evokes the famous paradox of Zeno denying the possibility of motion to a flying arrow, we call this result the Zeno's paradox in quantum theory."

This quote summarises the key idea that B. Misra and E. Sudarshan discuss in their seminal 1977 paper [38]. Let us illustrate their result by considering the short scale time evolution of a quantum system under the action of an hermitian Hamiltonian H. The

system could, for example, describe a quantum particle in an unstable state that would decay into an orthogonal state under the action of H. We assume that the system is initially prepared in the pure state $|\psi(t=0)\rangle = |\psi_0\rangle$. After a short time t, the system will be in the state:

$$|\psi(t)\rangle = e^{-\frac{i}{\hbar}\hat{H}t}|\psi_0\rangle = |\psi_0\rangle - \frac{i}{\hbar}\hat{H}t|\psi_0\rangle - \frac{1}{2\hbar}\hat{H}^2t^2|\psi_0\rangle + O(t^3)\,. \tag{1.1}$$

The probability that the system has not evolved away from its initial state is then given by:

$$p(t) = |\langle\psi(t)|\psi_0\rangle|^2 = 1 - \frac{t^2}{\tau_z^2} + O(t^4)\,, \tag{1.2}$$

with the "Zeno time" τ_Z:

$$\tau_Z^2 = \frac{1}{\hbar^2}\left(\langle\psi_0|H^2|\psi_0\rangle - \langle\psi_0|H|\psi_0\rangle^2\right)\,. \tag{1.3}$$

Let us now perform N projective measurements at regular time intervals $\tau = t/N$ to check whether the system is still in $|\psi_0\rangle$. If the intervals are short enough, the survival probability for each measurement is high, so that after every interval τ, the system will be projected back onto its initial state. The total survival probability at time t is then:

$$p^N(t) = p(t/N)^N \approx \left(1 - \left(\frac{t}{N}\frac{1}{\tau_Z}\right)^2\right)^N \xrightarrow{N \gg 1} \exp\left(-\frac{t^2}{N\tau_Z^2}\right)\,. \tag{1.4}$$

For large N, the evolution is slowed down and in the limit of $N \to \infty$, $t = $ const., the survival probability tends towards unity. This phenomenon is what Misra and Sudarshan called the quantum Zeno paradox: observing frequently enough whether the system is still in its initial state will freeze its evolution. While this result can seem paradoxical at first, it really is a direct consequence of the quantum mechanical law of time evolution, specifically the initially quadratic decrease in probability prescribed by the Schrödinger equation.

Eventually, the "paradox" was renamed the quantum Zeno effect and was demonstrated experimentally, first in a cloud of trapped ions [48] and later in various different physical systems, among them photons [49], individual ions [50], unstable atoms [51] and BECs [52].

1.1.2 Quantum Zeno dynamics

In the example of the previous section (as well as in Misra and Sudarshan's original paper), the "observation" took the form of a projective measurement in the sense of von Neumann that was applied in regular pulses. We now show that there are more general conditions that lead to the Zeno effect. Additionally, we only considered two outcomes

of the measurement, decay or no decay from the initial state, which lead to completely restricting the evolution of the system. In this section, we will see that an observation that leaves more freedom to the system results in richer dynamics, the quantum Zeno dynamics introduced in [53].

Let us extend the example of the previous section to a more general case. Let ρ be a density matrix that describes a quantum system in the Hilbert space $\mathcal{H}$. We assume that the time evolution of ρ is governed by the unitary operator $\hat{U} = \exp(-i\hat{H}t)$ where the Hamiltonian H is time-independent and lower-bounded. We describe the measurement still in terms of pulsed projections, however, we now follow the evolution of ρ in the complete Hilbert space $\mathcal{H}$ instead of just asking if our system is in one specific state or not. Specifically, we assume the measurement to consist of a (countable) set of projectors $\left\{\hat{P}_n\right\}$ so that

$$\hat{P}_n\hat{P}_m = \delta_{nm}\hat{P}_m, \quad \sum_n \hat{P}_n = \mathbb{1} \,. \tag{1.5}$$

Each projector spans a subspace $\mathcal{H}_n$, so that the total Hilbert space is partitioned as $\mathcal{H} = \sum \mathcal{H}_n$. The measurement described by these projectors is given by the superoperator

$$\mathcal{P}\rho = \sum_n \hat{P}_n\rho\hat{P}_n \,. \tag{1.6}$$

Equation 1.6 is seen to transform ρ into a block-diagonal form by eliminating off-diagonal elements between blocks corresponding to the different P_n, i.e. different subspaces. By performing this measurement, we prepare the system in the initial state

$$\rho_0 = \mathcal{P}\rho(t=0) \,. \tag{1.7}$$

The free evolution of the system is then given by

$$\rho(t) = \mathcal{U}(t) = \hat{U}(t)\rho_0\hat{U}^\dagger(t), \quad \hat{U}(t) = \exp(-i\hat{H}t) \,. \tag{1.8}$$

We now consider performing N measurements at regular time intervals $\tau = t/N$. This leads to the evolution

$$\rho^{(N)}(t) = \mathcal{V}^{(N)}(t)\rho_0 \,, \tag{1.9}$$

governed by the superoperator

$$\mathcal{V}^{(N)}(t) = \mathcal{P}\left(\mathcal{U}(t/N)\mathcal{P}\right)^{N-1} \,. \tag{1.10}$$

We now want to take the limit $N \to \infty$, $t = $ const. that produces the Zeno effect. It can be shown that if the Hamiltonian H is bounded and the subspaces $\mathcal{H}_n$ are of finite
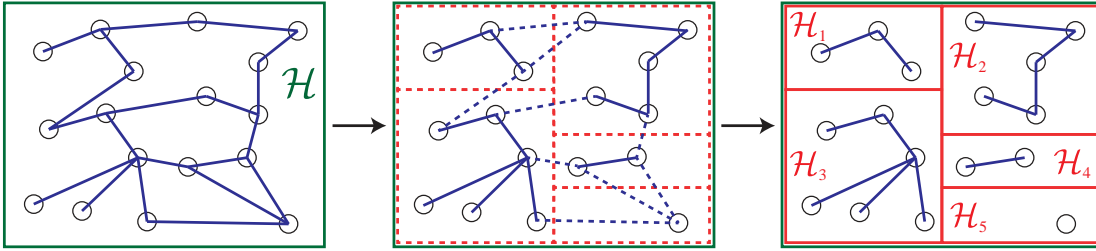
Figure 1.1: Illustration of Quantum Zeno dynamics. Left: A system in the Hilbert space $\mathcal{H}$ can occupy a number of states (black circles) coupled by an interaction Hamiltonian (blue lines). Centre: Introducing a Zeno measurement hinders the evolution between the different subspaces $\mathcal{H}_n$. Right: In the limit of infinitely frequent or infinitely strong measurement, the dynamics is completely confined in each subspace.

dimension (both conditions are met in our experiments), this limit is well defined and Equations 1.9 and 1.10 take the form [53]:

$$\rho^Z(t) \;=\; \sum_n V_n^Z(t)\rho_0 \left(V_n^Z\right)^{\dagger}(t)\,, \tag{1.11}$$

$$\left(V_n^Z\right)^{\dagger} V_n^Z = \hat{P}_n \quad \forall n \tag{1.12}$$

$$V_n^Z(t) \;=\; \hat{P}_n \exp(-i\hat{H}_Z t)\,, \tag{1.13}$$
$$\hat{H}_Z = \sum_n \hat{P}_n \hat{H} \hat{P}_n\,.$$

Equation 1.11 shows that $\rho^Z(t)$ is in a block-diagonal form in which any coherences between different subspaces $\mathcal{H}_n$ is eliminated (cf. Equation 1.6). This also means that

$$p_n(t) = \mathrm{Tr}(\rho(t)\hat{P}_n) = \mathrm{Tr}(\rho_0 \hat{P}_n) = p_n(0)\,, \tag{1.14}$$

i.e. the probability for the system to be in any of the subspaces in conserved during the modified evolution. In the limit of infinitely frequent measurements, the resulting quantum Zeno dynamics takes place in a Hilbert space partitioned by hard walls that prevent any leakage between the individual Zeno subspaces. Equation 1.13 shows that the dynamics contained in each subspace is unitary and governed by the effective Zeno Hamiltonian H_Z. This situation is illustrated in Figure 1.1. We note that if $p_n(0) = 1$, the system is initially completely contained in one of the subspaces which corresponds to the situation originally examined by Misra and Sudarshan (and to the example discussed in Section 1.1.1 if the subspace is additionally formed by a single state).

1.2 Measurement-based QZD in a spin $N/2$ system

In its most basic form, our experimental implementation of QZD can be modelled as a spin $N/2$ system in which we modify regular Rabi dynamics by a projective measurement. In the following, we present our Hilbert space (which is given by the collective qubit state of N atoms), the unitary dynamics taking place in the absence of the Zeno measurement and the QZD that is induced from a projective state measurement.

1.2.1 Multiparticle state space

The multiparticle system we study in our experiments consists of an ensemble of N atoms. Each atom can be considered as a qubit with a ground state $|0\rangle$ and an excited state $|1\rangle$. For our purposes, it is useful to describe the state of the ensemble in terms of Dicke states.

Dicke states

The state of a single qubit is completely determined by the expectation value of the vector $\hat{\mathbf{S}} = \frac{1}{2}(\hat{\sigma}_x, \hat{\sigma}_y, \hat{\sigma}_z)$ composed of the three Pauli spin-$1/2$ operators. For an ensemble of N identical spin-$1/2$ particles, we can then define a collective spin vector $\hat{\mathbf{J}} = \sum_{i=1}^{N} \hat{\mathbf{S}}_i$ which is the sum over the individual spin vectors $\hat{\mathbf{S}}_i$.

In analogy to angular-momentum formalism, a convenient basis for the N-particle space are the states $\{|J, m\rangle\}$ which are simultaneous eigenstates of $\hat{J}_z$ and $\hat{\mathbf{J}}^2$ with

$$\hat{\mathbf{J}}^2 |J, J_z\rangle = J(J+1)|J, J_z\rangle \quad \text{and} \quad \hat{J}_z |J, J_z\rangle = J_z |J, J_z\rangle, \tag{1.15}$$

where $J = N/2, N/2 - 1, \ldots; J \geq 0$ and $J_z = -J, -J + 1, \ldots J$. The structure of these states is depicted in Figure 1.2. Of special importance for us are the states with maximal spin $J = N/2$: they are symmetric and invariant under particle exchange. In the N-particle Hilbert space (of dimension $(2S+1)^N = 2^N$), these states span the symmetric subspace $\mathcal{H}_s$ (of dimension $2NS + 1 = N + 1$) which is closed under operations that affect all particles in the same way. $\mathcal{H}_s$ is spanned by the Dicke states [54] :

$$\{|n_N\rangle \equiv |J = N/2, J_z = -N/2 + n\rangle\} \quad n = 0, 1, \ldots, N. \tag{1.16}$$

In the Dicke state $|n_N\rangle$, the total spin is $J = N/2$ while the projection along the z-axis is $J_z = -J + n$. This means that n individual particle spins are in $|1\rangle$ and $N - n$ are in $|0\rangle$. The Dicke states describe a well defined number of excitations in the spin system which makes them the atomic analoga to the Fock states describing a well defined number of excitations of a light field. They are non-classical and an atomic ensemble in a qubit Dicke state features multiparticle entanglement, as detailed in Section 3.3.1.
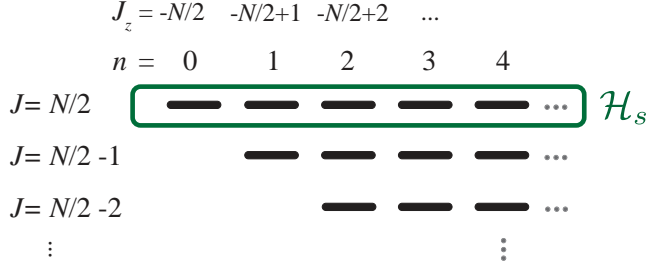
Figure 1.2: Structure of the angular momentum states $|J, J_z\rangle$ for N two-level atoms. The subspace $\mathcal{H}_s$ of fully symmetric states is spanned by the Dicke states $\{|n_N\rangle \equiv |J = N/2, J_z = -N/2 + n\rangle\}$.

Collective spin rotation

In our experiments, the qubit states are two hyperfine ground states of ^{87}Rb. This allows us to induce coherent rotations of the collective spin by means of MW radiation. In the following, we consider a rotation around the x-axis, generated by the operator $\hat{J}_x$ which, in the basis of Dicke states, has the following form:

$$\hat{J}_x = \frac{1}{2} \begin{pmatrix} 0 & \sqrt{n - n^2 + 2n\frac{N}{2}} & 0 & \cdots \\ \sqrt{n - n^2 + 2n\frac{N}{2}} & 0 & \ddots & \\ 0 & \ddots & \ddots & \\ \vdots & & & \end{pmatrix} \tag{1.17}$$

$$= \frac{1}{2} \begin{pmatrix} 0 & \sqrt{N} & 0 & \cdots \\ \sqrt{N} & 0 & \sqrt{2N-2} & \\ 0 & \sqrt{2N-2} & \ddots & \ddots \\ \vdots & & \ddots & \end{pmatrix}. \tag{1.18}$$

Driving this rotation with the Rabi frequency Ω is described by the Hamiltonian

$$\hat{H}_{\mathrm{MW}} = \hbar\Omega\hat{J}_x. \tag{1.19}$$

1.2.2 Unitary QZD in a spin $N/2$ system

Let us consider the dynamics that arises when driving a unitary rotation of the collective spin of N atoms while measuring the population of one of the Dicke states $|n_N\rangle$. The measurement is then described by a projection either on this state, given by the projector

$$\hat{P}_{|n_N\rangle} = |n_N\rangle\langle n_N|, \tag{1.20}$$

Figure 1.3: Comparison of Rabi and quantum Zeno dynamics in a spin $N/2$ system. The plots show the populations $\rho_{ii}(t)$ for a system of $N = 7$ atoms driven at Rabi frequency $\Omega = \pi/T$. Left: Rabi dynamics in the absence of Zeno measurement. Centre: unitary QZD when measuring the state $|4_N\rangle$. Right: unitary QZD when measuring the state $|7_N\rangle$.

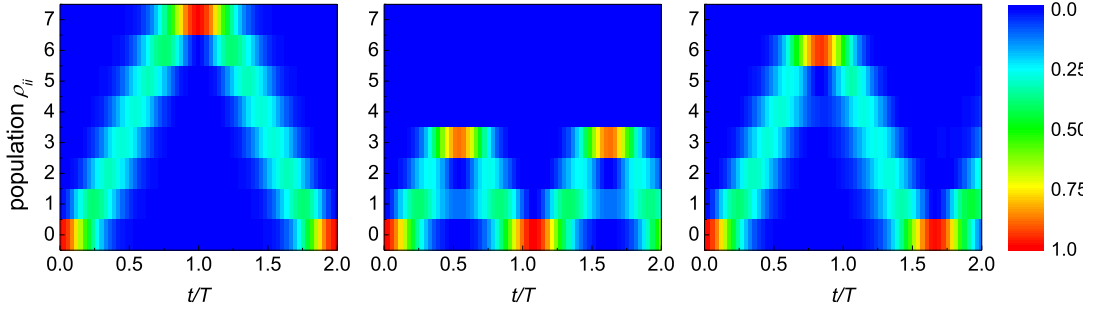or on the complementary Zeno subspace $\mathcal{H}_Z$

$$\hat{P}_{\mathcal{H}_Z} = \mathbb{1} - \hat{P}_n \,. \tag{1.21}$$

To obtain QZD (as opposed to a quantum Zeno effect), we prepare the system so that it is initially in a state $\rho(0)$ within $\mathcal{H}_Z$. The probability to populate the state $|n_N\rangle$ is then zero at all times so that the time evolution of $\rho(t)$, given by Equations 1.11 - 1.13, reads

$$\rho^Z(t) = \hat{V}_Z(t)\rho(0)\hat{V}_Z^\dagger(t) \quad \hat{V}_Z(t) = \hat{P}_{\mathcal{H}_{\mathscr{Z}}} \exp(-\frac{i}{\hbar}\hat{H}_Z t) \,, \tag{1.22}$$

$$\hat{H}_Z = \hat{P}_{\mathcal{H}_{\mathscr{Z}}} \hat{H}_{\mathrm{MW}} \hat{P}_{\mathcal{H}_{\mathscr{Z}}} = \hbar\Omega \hat{P}_{\mathcal{H}_{\mathscr{Z}}} \hat{J}_x \hat{P}_{\mathcal{H}_{\mathscr{Z}}} \,, \tag{1.23}$$

where $\hat{H}_Z$ is the effective Zeno Hamiltonian resulting from the measurement.

The evolution according to Equations 1.22 and 1.23 is plotted in Figure 1.3 for $N = 7$. In the absence of measurement (left frame), Rabi oscillations populate all states of the system, transferring the population from $|0_N\rangle$ at $t = 0$ to $|7_N\rangle$ at $t = T = \pi/\Omega$. Introducing a Zeno measurement of the state $|4_N\rangle$ (centre frame), the dynamics is heavily modified. As the system cannot cross the boundary to $|4_N\rangle$, it highly populates the state$|3_N\rangle$ before "bouncing" back towards $|0_N\rangle$. This dynamics is also faster than normal Rabi oscillations, with the maximal population $\rho_{33} \approx 0.9$ being reached at $t \approx \frac{4}{7}T$. If the measurement is instead performed on state $|7_N\rangle$ (right frame), the QZD leads to strong population of the state $|6_N\rangle$, with a maximum of $\rho_{66} \approx 0.95$ reached at $t \approx \frac{6}{7}T$.

In both examples, we see that the QZD creates states that are not accessible to the unitary dynamics alone. In the work presented in this thesis, we use this feature to experimentally create multiparticle-entangled states in an atomic ensemble.

1.3 QZD in an atomic ensemble coupled to an optical resonator

In this section, we present our experimental implementation of QZD. We work with an ensemble of ^{87}Rb atoms coupled to a high finesse Fabry-Perot cavity according to the configuration shown in Figure 1.4. By means of an atom chip, we prepare an atomic ensemble and load it into an intra-cavity dipole trap. An external magnetic bias field of 12.5 G lifts the degeneracy of the Zeeman states which allows us to implement an atomic qubit in the hyperfine states $|0\rangle = |F = 1, m_F = 0\rangle$ and $|1\rangle = |F = 2, m_F = 0\rangle$ of the $5\,^2S_{\frac{1}{2}}$ ground state multiplet. These states are magnetically insensitive which reduces the effect of ambient magnetic fields. They are split by about 6.8 GHz so that we can realise unitary rotations of the ensemble's collective spin through pulses of MW radiation. The cavity can be probed with a laser tuned to the transition $|1\rangle \to |e\rangle = F' = 3, m_F = 0\rangle$ close to the D$_2$-line at 780 nm. As the atoms are well confined in real and momentum space, the MW and probe radiation affects all of them near-identically so that we can coherently manipulate the collective quantum state of the ensemble. Due to slight asymmetries in the mirrors, our cavity features two orthogonally polarised eigenmodes with a frequency splitting of about 540 MHz. In the present experiments, probe and dipole lights are coupled to the higher frequency cavity mode. The magnetic bias field is oriented parallel to the corresponding eigenaxis of the cavity so that both lasers are π-polarised.

With this configuration, we can realise in good approximation a QZD scheme similar to the spin-$N/2$ model described in the previous section. The key point is to modify the collective qubit dynamics driven with the MW by means of a Zeno measurement arising from probing the cavity on the $|1\rangle \to |e\rangle$ transition. In the following sections we show that, in the case of strong atom-cavity coupling, this makes it possible to realise a measurement that projects the atomic ensemble either on the Dicke state $|0_N\rangle$, corresponding to all atoms in the cavity being in state $|0\rangle$, or on the complementary subspace in which at least one atom is in $|1\rangle$.

1.3.1 Multiparticle cQED in the strong-coupling limit

In this section, we present the fundamental concepts of cavity quantum electrodynamics (cQED) with which we can describe our experimental system, an ensemble of three-level atoms strongly coupled to an optical resonator.

The Jaynes-Cummings Hamiltonian

The simplest cQED model is that of a single two-level system (in our case an atom) coupled to one cavity mode. Neglecting the decay channels of the atom and the light field in the cavity, this system is described by the Jaynes-Cummings Hamiltonian [55]. In the dipole and rotating wave approximations and setting the energy of the vacuum field to zero, it is given by:
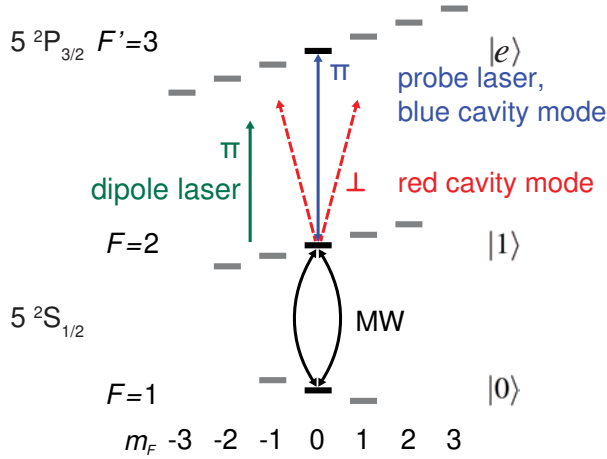
Figure 1.4: Experimentally relevant part of the ^{87}Rb level scheme. A magnetic field is applied along the polarization direction of the blue cavity mode, which is also the polarization of the probe beam. A resonant microwave (MW) at 6.8 GHz allows applying arbitrary rotations to the atomic qubit implemented in the states $|0\rangle = |F = 1, m_F = 0\rangle$ and $|1\rangle = |F = 2, m_F = 0\rangle$. Probe laser and the blue cavity eigenmode are resonant with the transition $|1\rangle \to |F' = 3, m_F = 0\rangle$.

$$\hat{H} = \hbar\omega_a\hat{\sigma}^+\hat{\sigma}^- + \hbar\omega_c\hat{a}^\dagger\hat{a} + \hbar g(\hat{a}^\dagger\hat{\sigma}^- + \hat{\sigma}^+\hat{a}) \,, \tag{1.24}$$

where $\hat{\sigma}^+ = |e\rangle\langle g|$ and $\hat{\sigma}^- = |g\rangle\langle e|$ are the atomic raising and lowering operators between the ground state $|g\rangle$ and the excited state $|e\rangle$, $\omega_a/2\pi$ and $\omega_c/2\pi$ are the frequencies of the atomic and cavity resonance, $\hat{a}^\dagger$ and $\hat{a}$ are the photon creation and annihilation operators (with the bosonic commutation relation $\left[\hat{a}, \hat{a}^\dagger\right] = 1$), and g describes the coupling between atom and light field. In Equation 1.24, the first two terms give the energy of the atom and light mode, respectively, and the third one the interaction between them, where $\hat{a}^\dagger\hat{\sigma}^-$ describes a photon exciting the atom and $\hat{\sigma}^+\hat{a}$ the atom relaxing by coherent emission of a photon. The coupling constant g is given by

$$g = \sqrt{\frac{\omega_c}{2\hbar\epsilon_0 V}}\mu_{ge} \,, \tag{1.25}$$

where V is the resonator mode volume and μ_{ge} is the dipole matrix element between $|g\rangle$ and $|e\rangle$. Note that in our experiment, we use a miniaturised resonator with small mode volume resulting in strong coupling.

By diagonalising Equation 1.24, the eigenstates of the coupled atom-cavity system can be obtained. They consist of a ground state $|g, 0\rangle$ (atom in the ground state zero photons in the cavity mode) and a ladder of excited doublet states corresponding to n excitations in the system. These "dressed" states are:
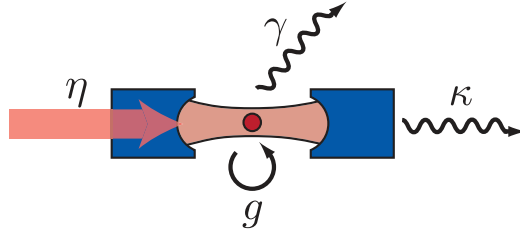
Figure 1.5: Schematic of the relevant processes in the open atom-cavity system. Photons are coherently added to the cavity at a pump rate η, atom and cavity are coupled with strength g and photons get lost due to spontaneous emission (at a rate γ) or leaking from the cavity mirrors (at a rate κ). Adapted from [45].

$$
\begin{aligned}
|+, n\rangle &= \sin \vartheta_n |g, n\rangle + \cos \vartheta_n |e, n-1\rangle \,, & \text{(1.26)} \\
|-, n\rangle &= \cos \vartheta_n |g, n\rangle - \sin \vartheta_n |e, n-1\rangle \,, & \text{(1.27)}
\end{aligned}
$$

with the mixing angle

$$
\tan \vartheta_n = \frac{\sqrt{n} g_0}{\Delta_{ac}/2 + \sqrt{g_0^2 n + (\Delta_{ac}/2)^2}} \quad \Delta_{ac} = \omega_a - \omega_c \,. \tag{1.28}
$$

Their energy eigenvalues are:

$$
E_{n,\pm} = n\hbar\omega_c + \frac{\hbar}{2} \left(\Delta_{ac} \pm \sqrt{\Delta_{ac}^2 + 4n g_0^2} \right) \,. \tag{1.29}
$$

The energy eigenvalues of the excited states form a ladder, spaced by $n\hbar\omega_c$, of doublets with splitting increasing proportional to $\sqrt{n} g_0$. For $n = 1$, this phenomenon is known as vacuum Rabi splitting: one excited atom coupled to the cavity leads to a splitting of the resonance frequency into two peaks.

Open system description of the Jaynes-Cummings model

In the experiment, we cannot study the closed system described by the Jaynes-Cummings Hamiltonian. Instead, we need to take into account that our quantum system is coupled to an environment. In our case, depicted schematically in Figure 1.5, one effect of the coupling is decoherence. Firstly, an atom in the cavity can decay by spontaneously emitting a photon into free space, described by the decay rate γ. Secondly, photons leak through the cavity mirrors with the rate κ. Additionally, we can add photons to the resonator by coherently pumping it with the rate η.

Master equation

This open system can be well described with a master equation approach [56, 57]. Given a quantum system described by the density operator ρ, its evolution under coupling to a reservoir can be described by a master equation of the form:

$$\frac{\mathrm{d}}{\mathrm{dt}}\rho = -\frac{i}{\hbar}\left[\hat{H}, \rho\right] + \sum_i 2\gamma_i \mathcal{D}\left[\hat{d}_i, \rho\right] , \tag{1.30}$$

$$\mathcal{D}\left[\hat{d}_i, \rho\right] = \hat{d}_i \rho \hat{d}_i^\dagger - \hat{d}_i^\dagger \hat{d}_i \hat{\rho}/2 - \rho \hat{d}_i^\dagger \hat{d}_i/2 , \tag{1.31}$$

where the hermitian $\hat{H}$ describes the evolution of the unperturbed system and the effect of the interaction with the environment is given by the super-operators $\mathcal{D}\left[\hat{d}_i, \hat{\rho}\right]$ that model decay processes with respective decay rates $2\gamma_i$. In our case, we need to include spontaneous emission at rate 2γ with the jump operator $\hat{d}_\gamma = \hat{\sigma}$ and cavity decay at rate 2κ with the jump operator $\hat{d}_\kappa = \hat{a}$. To describe the pump process with photons of frequency ω_p, we incorporate the following term into $\hat{H}$ [58]:

$$\hat{H}_p = -i\hbar\eta\left(\exp(i\omega_p t)\hat{a} - \exp(-i\omega_p t)\hat{a}^\dagger\right) . \tag{1.32}$$

Transforming into the frame rotating with ω_p the complete master equation reads:

$$\frac{\mathrm{d}}{\mathrm{dt}}\rho = -\frac{i}{\hbar}\left[\hat{H}, \rho\right] + 2\gamma\mathcal{D}\left[\hat{\sigma}, \rho\right] + 2\kappa\mathcal{D}\left[\hat{a}, \rho\right] , \tag{1.33a}$$

$$\hat{H} = -\Delta_{ap}\hbar\hat{\sigma}^+\hat{\sigma}^- + \Delta_{cp}\hbar\hat{a}^\dagger\hat{a} + g\hbar(\hat{a}^\dagger\hat{\sigma}^- + \hat{\sigma}^+\hat{a}) - i\hbar\eta\left(\hat{a} - \hat{a}^\dagger\right) , \tag{1.33b}$$

where $\Delta_{ap} = \omega_a - \omega_p$ and $\Delta_{cp} = \omega_c - \omega_p$.

Analytical solution for the steady-state

In the limit of weak excitation[1], Equations 1.33a and 1.33b can be solved analytically by restricting the state space to the three states $|g, 0\rangle$, $|e, 0\rangle$ and $|g, 1\rangle$. Specifically, the steady-state solutions for the atom excitation probability p_{ex} and the average photon number in the cavity n_{cav} can be calculated to be [60]:

$$p_{\mathrm{exc}} = \langle\hat{\sigma}^+\hat{\sigma}^-\rangle = \frac{\eta^2 g^2}{\left(g^2 - \Delta_{ap}\Delta_{cp} - \kappa\gamma\right)^2 + \left(\gamma\Delta_{cp} + \kappa\Delta_{ap}\right)^2} \tag{1.34}$$

$$n_{\mathrm{cav}} = \langle\hat{a}^\dagger\hat{a}\rangle = \frac{\eta^2/\kappa^2}{\left(1 + \frac{g^2}{\gamma\kappa}\frac{1}{1+\Delta_{ap}^2/\gamma^2}\right)^2 + \left(\frac{\Delta_{cp}}{\kappa} - \frac{g^2}{\kappa\gamma}\frac{\Delta_{ap}/\gamma}{1+\Delta_{ap}^2/\gamma^2}\right)^2} . \tag{1.35}$$

---

[1] As discussed in [59], the analytical solution renders the atomic excited state probability well if $\eta^2/g^2 \ll 1$. The results for the average photon number, however, are only valid as long as $\eta^2/g^2 \ll 1/C^2$.
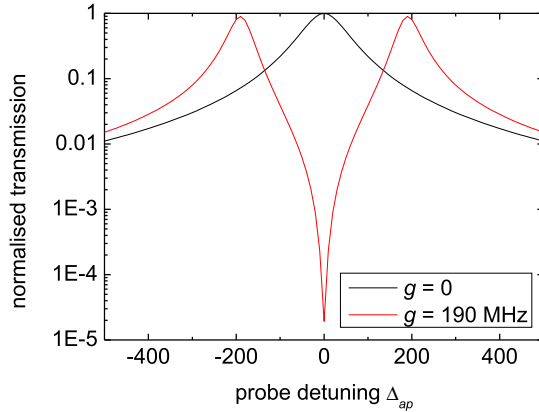
Figure 1.6: Transmission of the uncoupled (black) and coupled (red) atom-cavity system as a function of probe detuning with the cavity resonant to the atomic resonance ($\Delta_{cp} = \Delta_{ap}$). Our experimental parameters are $(\gamma, \kappa, g) = 2\pi(3, 53, 190)\,\mathrm{MHz}$.

The cavity transmission T is related to the steady state photon number by:

$$T = \kappa n_{\mathrm{cav}}\,. \tag{1.36}$$

Since we assume lossless mirrors, the transmission for an empty cavity on resonance is equal to the photon flux Φ that enters the cavity:

$$T_{\mathrm{empty}} = \kappa \frac{\eta^2}{\kappa^2} = \frac{\eta^2}{\kappa} = \Phi\,. \tag{1.37}$$

Figure 1.6 shows a plot of Equation 1.36 with and without an atom coupled to the cavity for the parameters of our experiment. The characteristic splitting of the resonance frequency in the coupled system can be clearly seen. Additionally, we observe that for $\Delta_{cp} = \Delta_{ap} = 0$, i.e. for cavity and probe both resonant with the atomic transition, the transmission of the coupled system T is strongly decreased compared to the one of the empty cavity T_{empty}. From Equation 1.35, we find:

$$\frac{T}{T_{\mathrm{empty}}} = \frac{1}{\left(1 + \frac{g^2}{\gamma\kappa}\right)^2} = \frac{1}{(1 + 2C)^2}\,, \tag{1.38}$$

where we define the single atom cooperativity parameter C as:

$$C \equiv \frac{g^2}{2\gamma\kappa}\,. \tag{1.39}$$

The cooperativity characterises how strong the coherent atom-cavity coupling is compared to the incoherent loss mechanisms. The situation $g \gg \gamma, \kappa$ (and consequently

17

$C \gg 1$) is known as the "strong coupling" limit of cQED, where already a single excitation changes the behaviour of the coupled system significantly. The parameters of our experimental system are $(\gamma, \kappa, g) = 2\pi(3, 53, 190)\,\mathrm{MHz}$ which corresponds to a cooperativity $C \approx 110$.

The atomic excitation probability allows us to calculate Γ_{eff}, the rate of spontaneous emission events in the coupled system. On resonance and for $g \gg \gamma, \kappa$, Equation 1.34 gives:

$$\Gamma_{\mathrm{eff}} = 2\gamma p_{\mathrm{exc}} = 2\gamma \frac{\eta^2 g^2}{(g^2 - \kappa\gamma)^2} \approx \frac{2\gamma\eta^2}{g^2} = \frac{1}{C}\Phi \,. \tag{1.40}$$

Tavis-Cummings model

So far, we have considered the coupling of one atom to the cavity, in our experiments, however, we work with ensembles of tens to hundreds of atoms. We describe this situation with the Tavis-Cummings model of n identical two-level systems all equally coupled with strength g to one mode of the light field. The Tavis-Cummings Hamiltonian reads [61]:

$$\hat{H}_n = \hbar\omega_c \hat{a}^\dagger \hat{a} + \hbar\omega_a \sum_{i=1}^{n} \hat{\sigma}_i^+ \hat{\sigma}_i^- + \hbar g \underbrace{\sum_{i=1}^{n}(\hat{a}^\dagger \hat{\sigma}_i^- + \hat{\sigma}_i^+ \hat{a})}_{\hat{H}_n^I} \,. \tag{1.41}$$

Let us consider the lowest eigenstates of the Tavis-Cummings model, starting with the uncoupled system. The states can be characterised by the number of excitations M in the system. For $M = 0$, all atoms are in the ground state and there are no photons in the cavity:

$$|M = 0\rangle_n = |g_1 \ldots g_n\rangle |0\rangle_{\mathrm{cav}} \,. \tag{1.42}$$

For $M = 1$, we can distinguish two cases. Either the atoms are in the ground state and there is a single photonic excitation:

$$|M = 1\rangle_{n,\mathrm{cav}} = |g_1 \ldots g_n\rangle |1\rangle_{\mathrm{cav}} \,, \tag{1.43}$$

or there is a single atomic excitation. If this weak excitation was applied in a process that acts identically on all atoms, the system will be described by the state:

$$|M = 1\rangle_{n,\mathrm{atoms}} = |\tilde{1}_n\rangle |0\rangle_{cav} \,, \tag{1.44}$$

$$|\tilde{1}_n\rangle = \frac{1}{\sqrt{n}} \left(|eg \ldots g\rangle + |geg \ldots g\rangle + \ldots + |g \ldots ge\rangle\right) \,, \tag{1.45}$$

where $|\tilde{1}_n\rangle$ is the first Dicke state, a symmetric, coherent superposition describing one excitation shared by the atomic ensemble.[2]

How strong is the coupling between the atomic ensemble and the light field? Defining a collective coupling g_n as the matrix element of the interaction Hamiltonian $\hat{H}_n^I$ in Equation 1.47 between the states with one atomic and one photonic excitation, we find:

$$g_n = \langle M = 1|_{n,\text{atoms}} \hat{H}_n^I |M = 1\rangle_{n,\text{cav}} = \sqrt{n}g \,. \tag{1.46}$$

The coupling of the ensemble to the light mode can be considered as that of one "super atom" with an effective coupling of $g_n = \sqrt{n}g$. With this approach, we can extend Equation 1.29, derived from the Jaynes-Cummings model, to obtain the vacuum Rabi splitting for n atoms coupled to the resonator:

$$E_{\pm,n} = \hbar\omega_a \pm \hbar\sqrt{n}g \,. \tag{1.47}$$

The corresponding eigenstates are, similar to the Jaynes-Cummings model, dressed states containing atomic and photonic contributions. On resonance $\omega_a = \omega_c$, the dressed states for $M = 1$ are:

$$|\pm, M = 1\rangle_n = \frac{1}{\sqrt{2}} \left(|M = 1\rangle_{n,\text{cav}} \pm |M = 1\rangle_{n,\text{atoms}} \right) \,. \tag{1.48}$$

Similarly, we find from Equations 1.39 and 1.38 the collective cooperativity

$$C_n = \frac{g_N^2}{2\gamma\kappa} = n \cdot C \tag{1.49}$$

and the transmission drop at resonance due to the vacuum Rabi splitting:

$$\frac{T_n}{T_0} = \frac{1}{(1 + 2Cn)^2} \approx \frac{1}{n^2} \frac{1}{4C^2} \,. \tag{1.50}$$

The behaviour described by Equation 1.50 is at the centre of our cQED experiments. Specifically, the strong reduction in cavity transmission (and increase in reflection) for $N > 1$ can be used to detect with high fidelity whether no atoms or at least one atom is coupled to the cavity [62, 45]. In the present work, we exploit this effect to implement the Zeno measurement discussed in the next section, as well as the quantum state tomography presented in Section 3.1.

What is the effective spontaneous emission rate if N atoms are coupled to the cavity? From Equation 1.40, we find:

$$\Gamma_{\text{eff},n} = 2\gamma p_{\text{exc},n} = \frac{1}{C_n}\Phi = \frac{1}{Cn}\Phi \,. \tag{1.51}$$

---

[2]Distinguish the state $|\tilde{1}_n\rangle$, describing one of n atoms coupled to the cavity being optically excited, from the state $|1_N\rangle$ introduced in see Section 1.2.1 which describes one atom in an ensemble of N being in the qubit state $|1\rangle$.

In this calculation, we assume that the spontaneous decay of the excited ensemble is not enhanced by super-radiance. This corresponds to the assumption that the spatial separation of the atoms in the ensemble is large compared to the emission wavelength λ. In our experiments, we work with a thermal ensemble of atoms in a dipole trap and estimate the dimensions of the ensemble on the trap axis and perpendicular to it to be on the order of $\sigma_\parallel \approx 40\,\mathrm{nm}$ and $\sigma_\perp \approx 800\,\mathrm{nm} \gtrsim \lambda$ respectively (see Section 2.8.1).

1.3.2   Implementing the Zeno measurement

In the following, we show how we generate QZD by a process that has the character of a strong, continuous, non-destructive quantum measurement which distinguishes the collective atomic state $|0_N\rangle$ from all other states in the symmetric subspace.

Measurement by coupling to a metre

So far, we have considered the measurement that induces the QZD to consist of instantaneous projections. This description is an idealisation of the physical process of a measurement. From a practical point of view, a quantum measurement comes about when the system under study interacts with an external metre which is macroscopic in the sense that we do not know or care about the details of its quantum state. The metre performs a measurement not necessarily in a way that makes the result known to the experimenter, for example with a detector that clicks or has an indicator. The important points are that the measurement is irreversible (like a von Neumann projection) and that it discriminates between different states. In this way, the experiments of [52, 40] have made use of spontaneous emission to realise an effective Zeno measurement: this process is irreversible and entangles the state of the system under consideration with the environment. In our case, we measure the state of the atomic ensemble through the photons decaying from the cavity light field.

Continuous state selective measurement

We now consider the evolution that takes place when we apply MW radiation and probe light at the same time. The unitary evolution due to the MW drive and the optical measurement with the cavity are simultaneous and continuous processes. It is therefore natural to describe the system in a master equation approach. Neglecting for now spontaneous emission, the evolution of the atomic density matrix ρ is given by:

$$\frac{\mathrm{d}}{\mathrm{dt}}\rho \;=\; -\frac{i}{\hbar}\left[\hat{H}_{MW},\rho\right] + \hat{d}\rho\hat{d}^\dagger - \frac{1}{2}\rho\hat{d}^\dagger\hat{d} - \frac{1}{2}\hat{d}^\dagger\hat{d}\rho\,. \tag{1.52}$$

The first term describes the unitary evolution due to the microwave field with $\hat{H}_{MW} = \hbar\Omega\hat{J}_x$ (cf. Section 1.2.1). The last three terms account for the loss of photons from the cavity with the jump operator $\hat{d} = \sqrt{2\kappa}\hat{a}$, where $\hat{a}$ annihilates a cavity photon.

Supposing the atoms are in the Dicke state $|n_N\rangle$ and the photon flux is Φ, a coherent field $|\alpha_n\rangle$ builds up in the cavity. Its amplitude is given by Equations 1.35 and 1.50:

$$\alpha_n = n_{cav} = \sqrt{\frac{\Phi}{\kappa} \frac{1}{1 + 2Cn}}\,. \tag{1.53}$$

As the photons carry information about the atomic state, the loss of a photon corresponds to an effective measurement. In our case, we keep both the flux Φ and the Rabi frequency Ω small compared to the cavity decay rate κ. We can then assume that the cavity field follows the number of atoms in state $|1\rangle$ instantly. Neglecting transient effects and tracing out the cavity, the loss of a cavity photon transforms into a jump operator for the atoms, which is given by

$$\begin{aligned}
\hat{d} &= \sum_{m,n} |m_N\rangle\langle\alpha_m|\sqrt{2\kappa}\hat{a}|\alpha_n\rangle\langle n_N| \tag{1.54}\\
&= \sum_{m,n} |m_N\rangle\sqrt{2\kappa}\alpha_n\, e^{-\frac{1}{2}|\alpha_n - \alpha_m|^2}\langle n_N| \tag{1.55}\\
&\simeq \sum_{n} \sqrt{r_m^{(n)}}|n_N\rangle\langle n_N|\,, \tag{1.56}
\end{aligned}$$

where the approximation is valid for sufficiently low flux Φ and where $r_m^{(n)}$ is the effective measurement rate

$$r_m^{(n)} = \frac{2\Phi}{(1 + 2Cn)^2}\,. \tag{1.57}$$

In the strong-coupling limit of cQED, $C \gg 1$, Equation 1.57 describes a highly state-selective measurement: for $n > 0$, the effective measurement rate $r_m^{(n)}$ is strongly suppressed compared to the case $n = 0$. This situation can be understood in terms of the Tavis-Cummings model as depicted schematically in Figure 1.7. Our Hilbert space is given by the symmetric subspace $\mathcal{H}_s$ which is spanned by the qubit Dicke states $|n_N\rangle$. We can couple the states $|n_N\rangle$ with the MW leading to dynamics with Rabi frequency Ω. The qubit Dicke states $|n_N\rangle$ without optical excitation correspond to the states $|M = 0\rangle_n$ of Equation 1.42. Pumping the cavity (weakly) with photons at rate η couples the states $|M = 0\rangle_n$ to the states with one excitation $|M = 1\rangle_n$. In the case of $n = 0$, there exists only one state $|M = 1\rangle_{0,cav}$ (Equation 1.43). The population of this state is "measured" by photons leaving the cavity at rate κ which leads to the effective measurement rate of the qubit state $|0_N\rangle$

$$r_m = 2\frac{\eta^2}{\kappa} = 2\Phi\,.$$

For the higher Dicke states $|n_N\rangle$, coupling to the excited states $|\pm, 1\rangle_n$ is strongly reduced due to the vacuum Rabi splitting. This leads to the reduced measurement rate $r_m^{(n)} \propto r_m/(Cn)^2$.
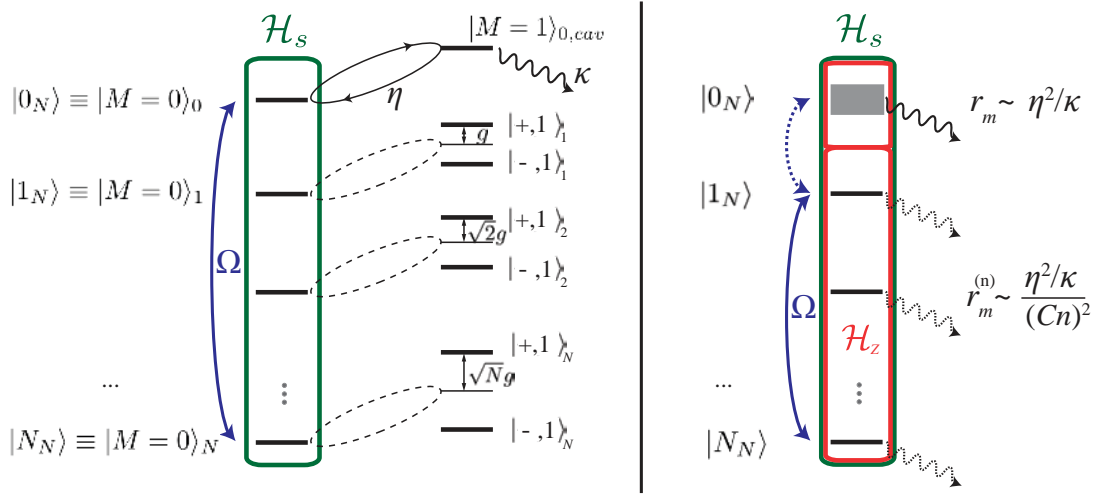
Figure 1.7: Implementing a state selective measurement with the cavity. A description in terms of the Tavis-Cummings model (left) translates into an effective continuous measurement (right). For $r_m^{(0)} > N\Omega > r_m^{(n)}$, the measurement confines the system in the Zeno subspace $\mathcal{H}_Z$.

Degeneracy of the measurement

We have seen in Section 1.1.2 that, in order for QZD to arise, we need to have a measurement that distinguishes a multidimensional subspace of the Hilbert space. Looking at Equation 1.57, we see that our measurement rate is different for every state $|n_N\rangle$. The key to realising QZD therefore lies in the relative strength of the measurement rates of the different states (corresponding to the Zeno subspaces) compared to the strength of the MW used to drive the dynamics. We see easily that an interesting regime is given by

$$r_m \simeq 2\Phi > \sqrt{N}\Omega > r_m^{(n)} \simeq 2\Phi \frac{1}{(2Cn)^2} \quad \forall n > 0\,. \tag{1.58}$$

In this case, the measurement is strong enough to change the dynamics of the MW rotation for the state $|0_N\rangle$ (given by the Rabi frequency $\sqrt{N}\Omega$, cf. the explicit form of the rotation operator given by Equation 1.18) while being too weak to influence the subspace formed by the other Dicke states. Preparing the atomic state within the subspace $\mathcal{H}_Z \in \mathcal{H}_s$ spanned by all Dicke states $|n_N\rangle$ with $n > 0$, the measurement will act as a barrier preventing the system to move into the state $|0_N\rangle$. In our case, the strong atom-cavity coupling with $C \approx 100$ gives us enough range to accommodate the MW drive with a typical frequency of $\Omega/2\pi \simeq 0.1\,\mathrm{MHz}$ for around $N \simeq 40$ with a typical photon flux in the cavity $\Phi \simeq 10\,\mathrm{MHz}$. Working in this parameter regime, we can describe our experiments with the master equation 1.52, where the jump operator is simply

$$\hat{d} = \sqrt{r_m}|0_N\rangle\langle 0_N| = \sqrt{2\Phi}|0_N\rangle\langle 0_N|. \tag{1.59}$$

Non-destructive nature of the measurement

We have seen that the cavity measurement can define Zeno subspaces. However, we also need to make sure that the measurement does not destroy the atomic state. The main concern in our case is spontaneous emission. The following rough calculations can serve to estimate the order of magnitude of the limits this poses on our scheme. We will see later that our experiments in the current setup are actually limited by the detrimental effect of the second cavity mode which leads to much higher scattering rates than the ones expected for a single mode cavity (see also Section 4.1.2).

On the one hand, an optically excited atom in $F' = 3$ can leave the qubit space by scattering into another Zeeman level. If it does fall back into the qubit subspace, the resulting collective state is non-symmetric with probability $p = 1 - 1/N$. For 40 atoms, $p > 80\%$, so to first order any resonant excitation will lead to loss from our Hilbert space. To observe QZD, the scattering rate needs to be small compared to the dynamics of the Rabi oscillation. This imposes the following condition on the resonant scattering rate for n atoms in $|1\rangle$, $\Gamma_{\text{eff},n}$ given by Equation 1.51 (for $C \gg 1$) :

$$\sqrt{N}\Omega > \Gamma_{\text{eff},n} \simeq \Phi\frac{1}{Cn}. \tag{1.60}$$

Comparing this condition with Equation 1.58, we see that the scattering limits the maximal photon flux we can use to produce the Zeno measurement.

We can also have non-resonant scattering by atoms in the qubit state $|0\rangle$. The scattering rate in this case is given by Equation 1.34, with $\Delta_{ap} = \Delta_{HFS} \gg g, \kappa, \gamma$:

$$\Gamma_{\text{eff},F=1} = 2\gamma p_{\text{exc}}n_{F=1} \approx 2\gamma\frac{\eta^2 g^2}{\kappa^2\Delta_{\text{HFS}}^2}n_{F=1} \tag{1.61}$$

$$= C\Phi\frac{(2\gamma)^2}{\Delta_{\text{HFS}}^2}n_{F=1} \approx 3\cdot 10^{-4}\Phi n_{F=1}. \tag{1.62}$$

The off-resonant scattering is maximal in the state $|0_N\rangle$. For our parameters ($N = 40, \Phi \lesssim 10\,\text{MHz}$) it attains a maximal value on the order of $\Gamma_{\text{eff},F=1}^{\max} \approx 2\pi \cdot 0.1\,\text{MHz}$. This is the same order of magnitude as our typical Rabi frequency Ω, thereby limiting the maximal ensemble size to about 100 atoms. In a new cavity setup, this limit could be improved by changing the cavity parameters, specifically the cooperativity. However, decreasing $\Gamma_{\text{eff},F=1}$ would require to decrease C which leads to higher resonant scattering as well as a lower measurement rate. Due to this trade-off, a detailed analysis would be necessary to optimise this limit (which in the end is set by the hyperfine state structure of Rb).

1.4   Conclusion

In this chapter, we have presented from a conceptual point of view how quantum Zeno dynamics can be produced in an experimental setup that allows to couple an ensemble of N atoms to an optical resonator. Our scheme relies on a continuous measurement of the collective atomic state which is strong enough to prevent MW-induced dynamics in a certain subspace of the complete atomic state space. Specifically, our system can be described by the Dicke states of an effective spin-$N/2$ qubit system in which probing the cavity can distinguish the state $|0_N\rangle$ from all other states. The measurement process needs to be non-destructive in order not to scramble the dynamics inside the Zeno subspace due to spontaneous emission. We have shown that we can meet these requirements experimentally, notably because of the strong collective coupling we can achieve between the atoms and a high finesse resonator. We also have introduced models that describe our system for both infinite and finite strength of the Zeno measurement.

Chapter 2

Experimental Setup

This chapter presents the experimental apparatus. Its core component is an atom chip with two integrated miniature Fabry-Perot resonators. An optical setup generates the necessary light fields. As the apparatus has been described extensively in [63, 59, 62], we concentrate here on a brief overview of its most important features and a documentation of the modifications made during this thesis.

In Section 2.1, we describe the apparatus used to create ultracold atomic samples on the atom chip as well as the integrated fibre Fabry-Perot cavities and the additional optical setup. In Section 2.7 we detail the work performed on the setup during the present work, which includes a significant speed up in the experimental cycle time and the realisation of short pulses of probing light necessary for the QZD experiments presented in Chapter 4.

2.1 Overview

The central idea behind the setup is to combine two different technologies that are at the same time simple and compact yet experimentally versatile and powerful. An atom chip allows us to create well confined ensembles of cold atoms in a single vacuum cell design. A high finesse Fabry-Perot resonator made from optical fibres provides light fields with a small mode volume. Integrating chip and cavity enables to position the atomic ensemble in a single antinode of the standing wave in the resonator, realising cavity QED in the strong coupling regime.

The core part of the experimental apparatus consisting of atom chip, ultra high vacuum (UHV) apparatus and fibre cavities was completed in 2007 [63] and has stayed basically unmodified since then. It is still running fine at the time of writing without major maintenance which speaks for its careful construction as well as for the robustness of the miniaturised approach.

2.2 The atom chip

2.2.1 Magnetic traps and atom chips

To study atoms at the quantum mechanical level it is necessary to confine them spatially. One option to trap neutral atoms is to make use of the potential energy shift they

experience in an external magnetic field due to their magnetic moment. If the energy shift ΔE is small compared to the hyperfine splitting, it can be written as $\Delta E(\mathbf{B}) = \mu_B g_F m_F |\mathbf{B}|$ where μ_B is the Bohr magneton, g_F the Landé factor and m_F the magnetic quantum number [64]. If $g_F m_F < 0$, atoms are attracted towards minima of the magnetic field. Since local maxima of the magnetic field in free space are forbidden by Maxwell's equations, only these low field seeking states can be trapped with static magnetic fields. For ^{87}Rb in the $^5\mathrm{S}_{1/2}$ multiplet, the states $|F = 1, m_F = 1\rangle$ and $|F = 2, m_F = 1, 2\rangle$ are low field seekers.

The spatially inhomogeneous fields required for magnetic trapping are typically generated from electric currents passing through conductors. According to the Biot-Savart law, the magnetic field B is inversely proportional to the distance r from a current-carrying wire and the field gradient $\frac{\partial B}{\partial r}$ decreases quadratically. To create steep traps, it is therefore advantageous to bring the conductors as close to the atoms as possible. This idea lead to the proposal of microscopic wire structures that can be patterned on planar substrates [65]. The structures can be realised using common photolithography techniques used in microelectronics. Reducing the typical length scales to 10...100 μm, such planar microfabricated substrates ("atom chips") are a simple way to create complex field geometries, not only providing high gradients but also transport and other manipulation techniques [66, 67, 68, 69, 70]. The tightly confining traps that can be created by microstructures are especially interesting for the production of BECs, allowing condensation by evaporative cooling to be one order of magnitude faster than in macroscopic traps and relaxing the requirements on the vacuum quality [71, 72].

A review of common wire configurations to create trapping potentials such as quadrupole, Ioffe-Pritchard, waveguide and dimple can be found in [73].

2.2.2 The FFP chip

The atom chip in our setup consists of two individual AlN substrates glued together with a thermally conductive, electrically insulating and vacuum compatible glue. The bigger "base" chip measuring 0.8 mm×35 mm×45 mm carries in its centre the smaller "science" chip measuring 0.63 mm×25 mm×28 mm (see Fig. 2.1). The wire structures on the chips are made from Au and produced in thin-film hybrid design. The structures are 7 μm thick with dimensions of 0.2 mm - 1 mm on the base chip down to 50 μm on the science chip. Structurally, the base chip seals the top end of a glass cell that acts as a vacuum chamber with excellent optical access. The base chip also serves as a feedthrough for all wire connections. It protrudes on two sides over the glass cell to give easy access to 2×24 electric contacts, of which 2×19 are connections to the science chip while the rest addresses magnetic trap structures on the base. The science chip is completely enclosed in the vacuum cell and electrically contacted to the base through bonding wires. Due to the piggyback construction, optical access to the surface of the science chip is not obstructed by the unavoidable glue meniscus between (base) chip and cell.

The science chip provides the physical support for the fibre Fabry-Perot cavities as well
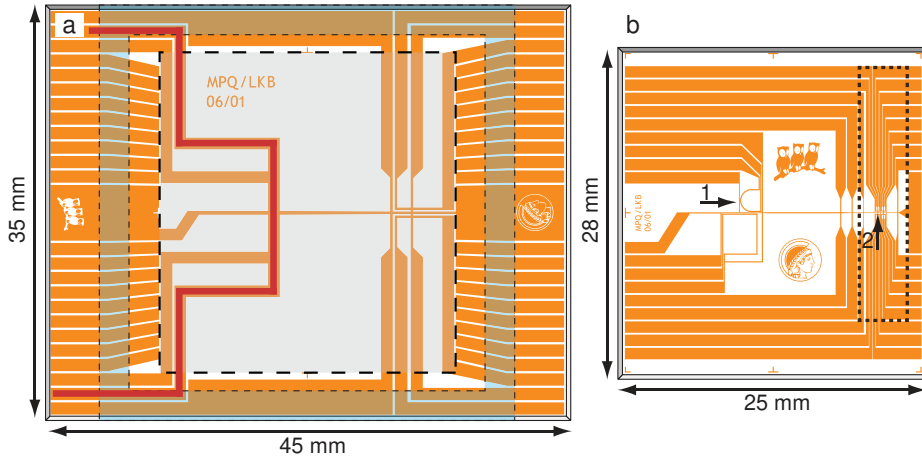
Figure 2.1: The two microsubstrates of the atom chip in the experiment. a) The base chip. Fine dashes indicate the position of the glass cell, rough dashes the position of the science chip. The red line indicates the U wire used for the quadrupole field of the chip MOT (cf. Section 2.8.1). The left and right edges serve as connectors for the chip wires. b) The science chip. The dotted line indicates the position of the resonator support bridge. The initial MOT and the first magnetic trap are at position 1, the centre of the first FFP resonator is at position 2. Adapted from [63] .

as the magnetic potentials that allow us to position ultracold atoms in the first resonator. To be able to load atoms into the magnetic traps, we first cool them in a magneto-optical trap (MOT) [74]. Efficient loading requires a high spatial overlap between the magnetic trap and the MOT which is difficult to achieve with a standard six-beam configuration due to the chip surface. We therefore make use of a mirror MOT [66]: the surface of the science chip is covered with a mirror coating, which allows a configuration of four light beams to create a MOT close to the chip. As explained in Section 2.5, the geometrical position of the mirror-MOT beams is still constrained by the finite size of the fibre cavity assembly, so that the MOT can only be created at a certain distance from the resonators. The specific series of magnetic potentials that realises the transport of the atoms from the MOT to the resonator is described in Section 3.

2.3   FFP cavity assembly

The centre-piece of the experiment are the two miniature Fabry-Perot cavities integrated on the atom chip. In the experiments, only the "science" cavity FFP1 is coupled to the atoms while the other (FFP2) serves for locking purposes. Each FFP is formed by two optical fibres facing each other with their end facets having been microfabricated (see also Section 5.2) and treated with a highly reflective coating[1] [46]. This technology has

---

[1]A dielectric multilayer coating custom made at the Laser Zentrum Hannover.
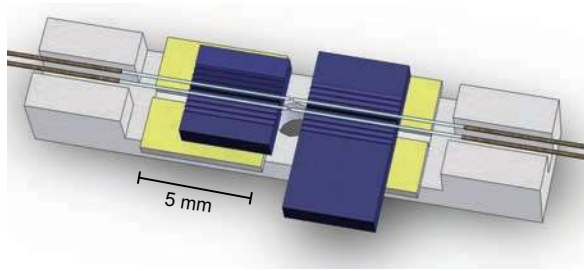
Figure 2.2: FFP cavity assembly (schematic). A support bridge made from ceramic (light grey) carries two shear piezos (yellow). Each piezo carries two silicon substrates (blue) into which the microfabricated fibres are glued.

several strong advantages:

- Small mode volume: The microfabricated mirrors can be small while having large curvatures. By making the resonator length small, this makes it possible to build stable cavities with very small mode volume which translates into strong atom-light coupling (cf. Equation 1.25).

- High finesse: The microfabrication produces surfaces of very low roughness which translates into high finesse.

- Compact size: The small size of the optical fibres allows to approach the surface of the atom chip where the confinement of the magnetic traps is strong. This allows one to load an ensemble of thousands of atoms into one specific antinode of the standing wave inside the resonator.

For an FFP resonator to perform optimally as atom-light interface in the experiment, it is critical that the two fibres are well aligned with respect to each other and that the cavity as a whole is well aligned with the atom chip. In the present setup, these two challenges are realised separately by introducing a support which carries the correctly aligned cavities, which can then be placed as a whole at the desired position on the atom chip. The approach is furthermore to fix as many degrees of freedom as possible during construction, retaining as only variable the cavity length (which is indispensable to control the cavity resonance).

The support assembly for the FFP cavities in the present experiment is shown schematically in Figure 2.2. Two piezoelectric shear actuators are glued onto a support bridge made from machinable ceramic (Macor). The shear piezos have a stroke of $\simeq 1$ nm/V which is sufficient to change the cavity length within one free spectral range ($\simeq 390$ nm) with a typical high voltage driver. Once in place, the piezos are cut along the long symmetry axis of the bridge to be able to control the length of both cavities independently. The microfabricated fibres ($\varnothing\,125\,\mu$m) are glued into silicon v-groove substrates which are then aligned precisely while, in turn, gluing the substrates to the piezos with a slow-curing epoxy glue. This step is critical, as the tolerance for the positions of the fibres
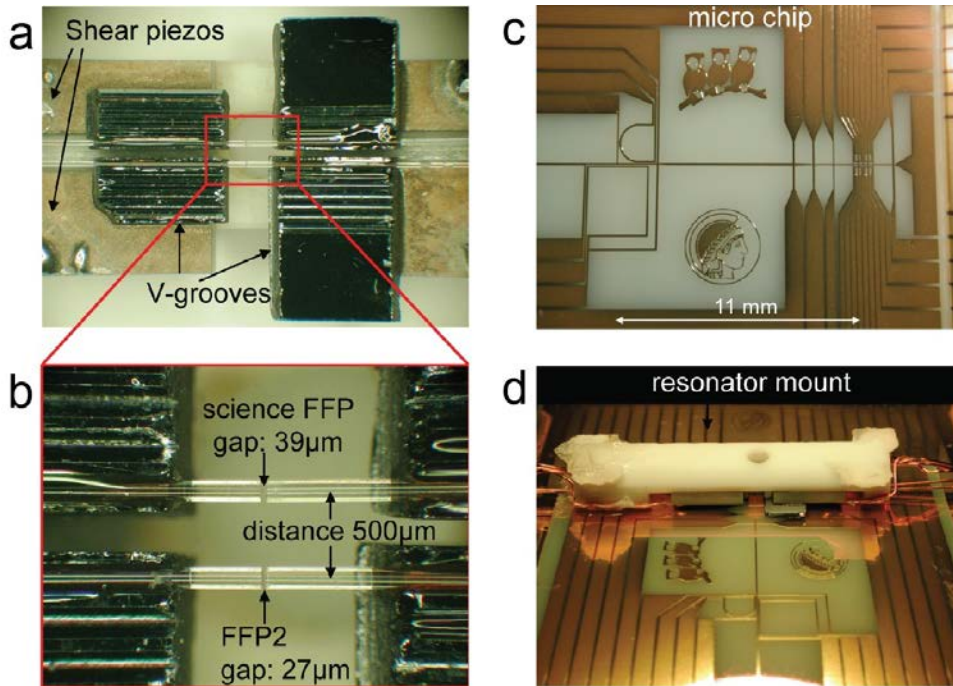
Figure 2.3: Photographies of the completed FFP setup. a) The completed FFP cavity assembly before gluing on the chip. The hole in the centre of the bridge gives optical access to the cavity region. b) Close-up of the two FFP cavities. c) The science layer of the atom chip. d) The mounted FFP cavity assembly. The assembly is flipped over compared to the position shown in Figure 2.2. The copper wires to the left and right of the bridge electrically contact the shear piezos, what appears like thinner wires are the copper-coated FFP fibres. Adapted from [63].

with respect to each other is on the order of 1 μm. During the first 12 hours of curing, it was therefore necessary to monitor the cavity transmission and adjust the alignment to correct for displacement of the shrinking glue.

The completed FFP cavity assembly was then attached with UV glue to the atom chip while ensuring the correct alignment of the fibre facets with the wire structures. The distance between the chip surface and the fibres (cavity mode) is $\simeq 90(150)\,\mu$m. Figure 2.3 shows photographies of the FFP assembly and the completed chip setup.

2.3.1 FFP cavity characteristics

Both cavities consist of a single-mode fibre[2] (SMF) on the input side and a multi-mode fibre[3] (MMF) on the output side which relaxes the requirements on the resonator

---

[2]Oxford Electronics SM800-125CB.
[3]Oxford Electronics GI50-125CB.

parameter	FFP1	FFP2	source
geometry			
r_1: ROC^a single-mode fibre	450 μm	350μm	estimated [63]
r_2: ROC multi-mode fibre	150 μm	100 μm	
d: effective resonator length	39 μm	27 μm	computed from $FSR = \frac{c}{2d}$
optical parameters at 780 nm			
FSR: free spectral range	3.9 THz	5.6 THz	measured [62]
$\Delta\nu_{FWHM}$: linewidth (FWHM)	106 MHz	156 MHz	
F: finesse	37000	36000	computed from $F = \frac{FSR}{\delta\nu}$
$\Delta\nu$: frequency splitting	540 MHz	730 MHz	measured [63]
T: mirror transmission	31 ppm		measured [63]
L: mirror losses	56 ppm		computed from $F = \frac{2\pi}{T+L}$
T_0: total cavity transmission	9.4%	n.a.	measured [63]
R_0: maximal cavity reflection	47%	n.a	
w_0: mode waist	3.9 μm	3.2 μm	computed from r_1, r_2, d
V_m: mode volume	461μm	217μm	see text!
$\kappa/2\pi$: decay constant	53 MHz	78 MHz	measured [62]
$g_m/2\pi$: coupling constant	240 MHz	313 MHz	measured [62]
C: cooperativity	181	210	computed from $C = \frac{g^2}{2\kappa\gamma}$
optical parameters at 830 nm			
$\Delta\nu_{FWHM}$: linewidth (FWHM)	260 MHz	390 MHz	measured [62]
F: finesse	14000	13100	computed from $F = \frac{FSR}{\delta\nu}$

^{a}ROC: radius of curvature

Table 2.1: Geometrical and optical parameters of the two FFP cavities.

alignment. The fibres are commercially available and feature a Cu coating on the exterior which makes them UHV compatible and increases their mechanical stability.

The relevant parameters of the two fibre cavities in the experiment are collected in Table 2.1. All relevant cQED parameters have been measured in previous experiments. Free spectral range FSR, decay rate κ, birefringent mode splitting Δ, as well as total cavity transmission T_0 and reflection R are easily accessible from direct optical measurements. The coupling constant of the σ^+ transition $|F = 2, m_F = 2\rangle \rightarrow |F = 3, m_F = 3\rangle$ has been derived from spectroscopic measurements of the vacuum Rabi splitting of the coupled atom-cavity system to be $g_m = 240(10)$ MHz for FFP1. For the experiments performed in this thesis, we work on the transition $|F = 2, m_F = 0\rangle \rightarrow |F = 3, m_F = 0\rangle$. Taking into account the different Clebsch-Gordan coefficients, we find a value of $g = \sqrt{2/3}g_m \approx 190$ MHz which we use as an input parameter for our calculations.

The radius of curvature (ROC) r of each cavity mirror has been estimated from the fibre fabrication process. We note that these values can be used to obtain a theoretical value for g_m based on cavity geometry. The waist w_0 of a Gaussian beam matched to a

resonator of length d made from mirrors with ROC r_1, r_2 is given by [75]:

$$w_0^2 = \frac{\lambda}{\pi} \sqrt{\frac{d(r_1 - d)(r_2 - d)(r_1 + r_2 - d)}{(r_1 + r_2 - 2d)^2}} \, .$$

(2.1)

The volume of the fundamental mode is (see [63], p. 15):

$$V_m = \frac{\pi w_0^2 d}{4} \, .$$

(2.2)

Inserting the computed V_m and the dipole matrix element $d_{22 \to 33}$ for the σ^+ transition $|F = 2, m_F = 2\rangle \to |F = 3, m_F = 3\rangle$ into Equation 1.25, we obtain a theoretical value of $g_0^{\text{theor}}/2\pi \simeq 210$ MHz. Taking into account that the ROC have not been determined with precision, this agrees reasonably well with the measured value.

The distance between the first/second mirror and the waist is given by [75] :

$$d_{1/2} = \frac{d(r_{2/1} - d)}{r_1 + r_2 - 2d} \, ,$$

(2.3)

which evaluates for FFP1 to $d_{1/2} \simeq 8.3 \, \mu\text{m}/30.7 \, \mu\text{m}$ as the distance from the SMF/MMF.

The FFP1 resonator used to couple to the atoms shows a frequency splitting between two polarisation eigenmodes of the TEM_{00} mode. The modes are linearly orthogonally polarised and separated by about 540 MHz. In the experiments presented here, both probe and dipole light address the higher frequency polarisation mode (see also Section 4.1). The effect of the second mode in our experiments is discussed in detail in Section 4.1.1. The origin of the polarisation mode splitting is discussed in detail in Chapter 5.

Dipole trap

Each FFP resonator is constructed to allow having an intra-cavity standing wave dipole trap [76]. In practice, we use light at $\simeq 830$ nm that serves both to lock the cavity length and to trap atoms inside FFP1. Because of the different wavelengths of probe (780 nm) and dipole light, care has to be taken that the antinodes of both overlap to couple all atoms uniformly and maximally to the probe light field. The cavity length and the wavelength of the dipole laser are therefore chosen so that probe and dipole light fields both have an antinode at the geometric centre of the cavity. For details on how the coupling changes with the position in the cavity, see Section 2.8.3.

2.4   Cell and vacuum setup

The vacuum cell is shown schematically in Figure 2.4. The chip forms the top wall of a glass cell[4] that provides - via a glass to metal transition - the connection to the

---

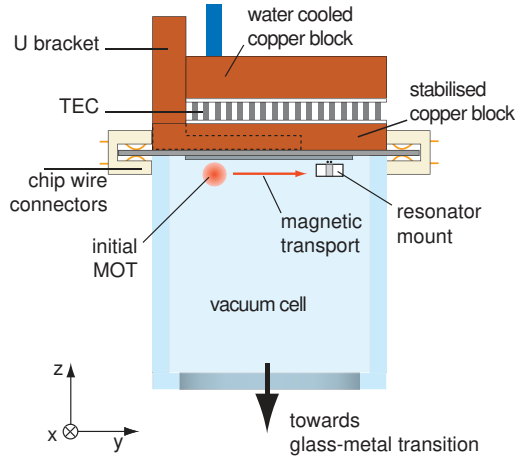[4]Hellma 704.001-OG with anti-reflective coating on the outside.

Figure 2.4: Schematic of the experiment cell. The chip forms the top wall of the vacuum cell. It is electrically contacted by two PCI connectors. On top of the chip is the U-shaped copper bracket, the copper piece and thermoelectric cooler (TEC) for temperature stabilisation and the water cooled copper block for heat dissipation. The different positions of the initial MOT and the resonator are also shown. Adapted from [63].

UHV apparatus. To the top side of the chip, a macroscopic "U"-shaped copper piece is attached. This piece is used to create the quadrupole field for the first MOT at the beginning of the experimental sequence (see Section 3). The currents in the atom chip wires and the "U" bracket generate considerable resistive heat. The "U" is therefore embedded in a copper block that is cooled by a thermoelectric cooler (TEC). The TEC is controlled by a servo loop using a thermistor in the copper block as sensor to actively stabilise its temperature. In previous work, the servo loop was active during all phases of the experiment, so that the current through the TEC, in principle, was varying at all times. The magnetic field associated with the current being a potential noise source, we modified the setup during the present work to switch off the TEC during the critical part of the experimental cycle. The heat of the TEC is dissipated by a water cooled copper block.

Figure 2.5 shows a schematic of the ultra high vacuum setup. As rubidium source we use a dispenser placed inside the glass-metal transition which is connected to the top port of a six-way cross[5]. The bottom port is a window for optical access, the cross also connects to a titanium sublimation pump, an electrical feed-through for the dispensers and another four-way cross. Here, a pressure gauge, an ion pump and the valve for attaching the turbo pump are connected.

Around the glass cell, there is a metal cage that holds four pairs of water-cooled coils. Three pairs in Helmholtz configuration generate bias fields in the three spatial directions and one pair in anti-Helmholtz configuration creates a field gradient for the magnetic

---

[5]There is another dispenser inside the cross which we have not used. Both models are SAES-Getters RB/NF/3.4/12FT10+10.
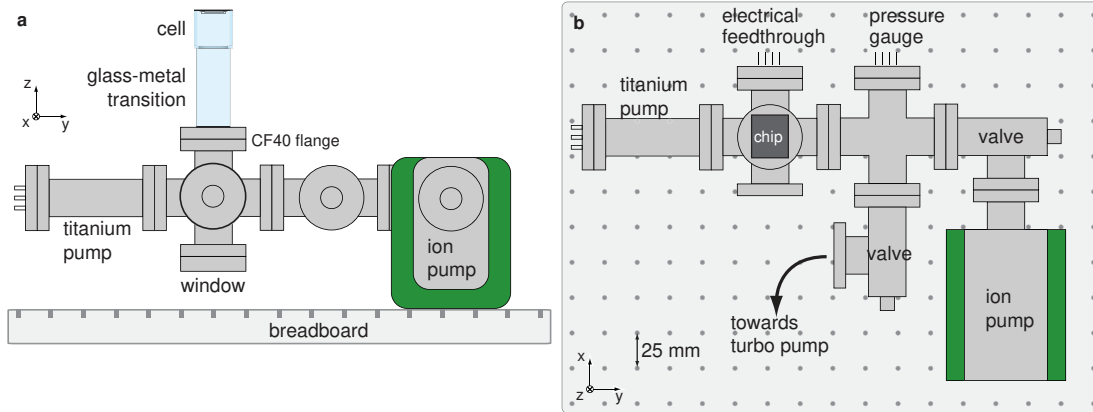
Figure 2.5: Vacuum setup. a) Side view. b) Top view. Adapted from [63].

transport.

A microwave antenna is placed at a distance of approximately 50 cm from the cell and directed towards it. It is connected to the microwave system described in Section 2.7.2 that allows us to drive Rabi oscillations between the hyperfine ground state levels $F = 1$ and $F = 2$ of ^{87}Rb that are separated by $\simeq 6.8\,\text{GHz}$.

A home-built coil (10 turns, $\varnothing \approx 30\,\text{mm}$) close to the cell is used to inject RF in the range of 30...1 MHz for evaporative cooling.

2.5 Optical setup

In the experiments, we need light fields for six different purposes:

- cooling the atoms in the MOT and optical molasses,

- pumping the atoms into a magnetically trappable Zeeman state,

- imaging the atoms via absorption imaging,

- probing the atoms in the cavity,

- creating a dipole trap in the cavity,

- locking the fibre cavity length.

The first four points require light frequencies close to resonance with the D_2 line of ^{87}Rb at around 780 nm (see Figure 2.6), for the last two tasks we use far red-detuned light at 830 nm. We generate all light fields from home-built external grating stabilised laser diodes [77]. They are frequency-locked to reference signals via feedback on the grating angle.

The optical setup is organised in four parts, the "main optical table", the "locking" table, the "detection" table, and the optics surrounding the vacuum cell.
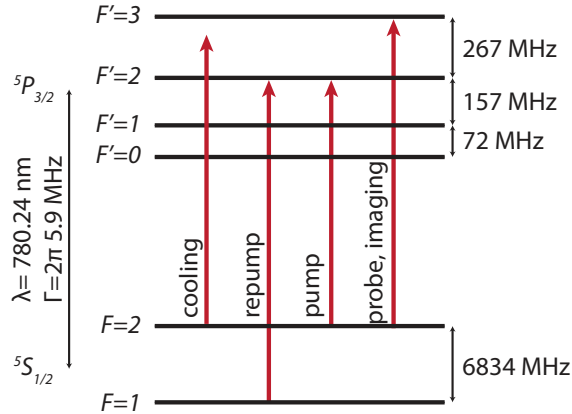
Figure 2.6: Level scheme of the D_2 line of ^{87}Rb with relevant laser light frequencies.

2.5.1 Main table

The beam paths on the main table are shown in Figure 2.7. There are three diode lasers at around 780 nm, each locked to a frequency modulated Doppler-free absorption spectroscopy [78, 79]. They generate the following light fields close to resonance with the D_2 line of ^{87}Rb:

- Cooling: The light for cooling the atoms in the MOT and optical molasses is generated from the "main" laser locked to the $F = 2 \rightarrow F' = 2, 3$ crossover transition. The main part of its output light is used to inject the tapered amplifier (TA) (see Section 2.7.1), while a small fraction is sent to the "locking" table to lock the auxiliary laser there. A small part of the TA output is used to create a beat lock signal with the FFP probe laser. The main part of the TA output is frequency-shifted by $+2 \times 96\,\mathrm{MHz}$ using an acousto-optic modulator (AOM) in double-pass configuration [80] and then shifted by a fixed amount of $-80\,\mathrm{MHz}$ using a single pass AOM. The double-pass AOM serves to vary the red detuning of the cooling light between $\sim 7\Gamma$ (MOT phases) and $\sim 11\Gamma$ (molasses phase). The cooling light is then coupled into four polarisation-maintaining (PM) single-mode (SM) optical fibres leading towards the vacuum cell where the four beams for the mirror MOT are created.

- Repump: Atoms can get lost from the cooling cycle by falling into $F = 1$. They are recovered by light on the $F = 1 \rightarrow F' = 2$ transition which is created with a "repump" laser locked to the $F = 2 \rightarrow F' = 1, 2$ crossover and an AOM at $-83\,\mathrm{MHz}$. The light is overlapped with one of the MOT cooling beams and coupled into the same fibre.

- Detection: A small part of the TA output after the double-pass is sent through another AOM at $+53\,\mathrm{MHz}$. The resulting light is resonant to the (Zeeman-shifted) $F = 2 \rightarrow F' = 3$ transition and used for absorption imaging of the atoms outside

of the cavity. The two detection beams "x" and "y" corresponding to different imaging regions on the chip are coupled into fibres leading to the cell.

- Pump: A small part of the "main laser" light is shifted by $-2 \times 66\,\text{MHz}$ to make it resonant to the $F = 2 \rightarrow F' = 2$ transition. It is overlapped with the x-detection beam and used to pump the atoms into the magnetically trappable state $|F = 2, m_F = 2\rangle$ (cf. Sections 2.2 and 2.8).

- Probe: To probe the atoms resonant to the $F = 2 \rightarrow F' = 3$ transition, we employ the "FFP probe" laser. A fraction of its light overlapped with the main laser goes to a photodiode (PD). The resulting beat signal is used to lock the probe to the main laser via an offset lock that allows us to precisely control the lock point (see also Section B). The main part of the light is shifted by a double-pass AOM at $+2 \times 207\,\text{MHz}$ and coupled into a fibre leading to the "locking" table.

2.5.2 Locking table

This part of the optical setup provides the light for locking the FFP cavities and to create a dipole trap inside. For both purposes, a "dipole" laser at around $830\,\text{nm}$ is used. We stabilise and control its frequency in a chain of several locking steps [62]: The dipole laser is locked to a macroscopic transfer cavity that is locked to an "auxiliary" laser at $780\,\text{nm}$ that is locked to the "main" laser (which is locked spectroscopically). The beam paths on the table are shown in Figure 2.8.

A fraction of the light from the **auxiliary laser (aux)** and the small part of the main laser coming from the main table are overlapped on a PD. The resulting beat signal is used for the offset-lock (based on a digital frequency-to-voltage converter) of the aux laser frequency to the "main laser" frequency. The rest of the aux laser light is mode-filtered and then used to lock the transfer cavity in a Pound-Drever-Hall (PDH) scheme [81]. The aux light is phase-modulated with a free-space electro-optical modulator (EOM)[6] to apply sidebands at around $18\,\text{MHz}$ and then sent to the transfer cavity. The light reflected from the cavity is collected on a PD to produce an error signal used to stabilise the cavity length via a piezo actuator to the aux laser frequency.

The **dipole laser** light is split into three beam paths. Part of the light is superimposed with the aux laser to implement another PDH lock with the transfer cavity. The reflected light at $830\,\text{nm}$ is separated from the aux beam with a filter and sent to a separate PD to produce an error signal that is used to lock the dipole laser frequency to the transfer cavity. Another part of the dipole light is sent through a double-pass AOM that shifts its frequency by $2 \times (175...225)\,\text{MHz}$ and then through a fibre-coupled EOM[7] towards the "detection" table (where it is coupled to the FFP1 cavity). The EOM imprints side-bands at $1.8\,\text{GHz}$ which are used for a PDH lock of the fibre cavity length to the

---

[6]Qubig High-Q 17.85 MHz.
[7]Photline NIR-MPX800-LN-10.
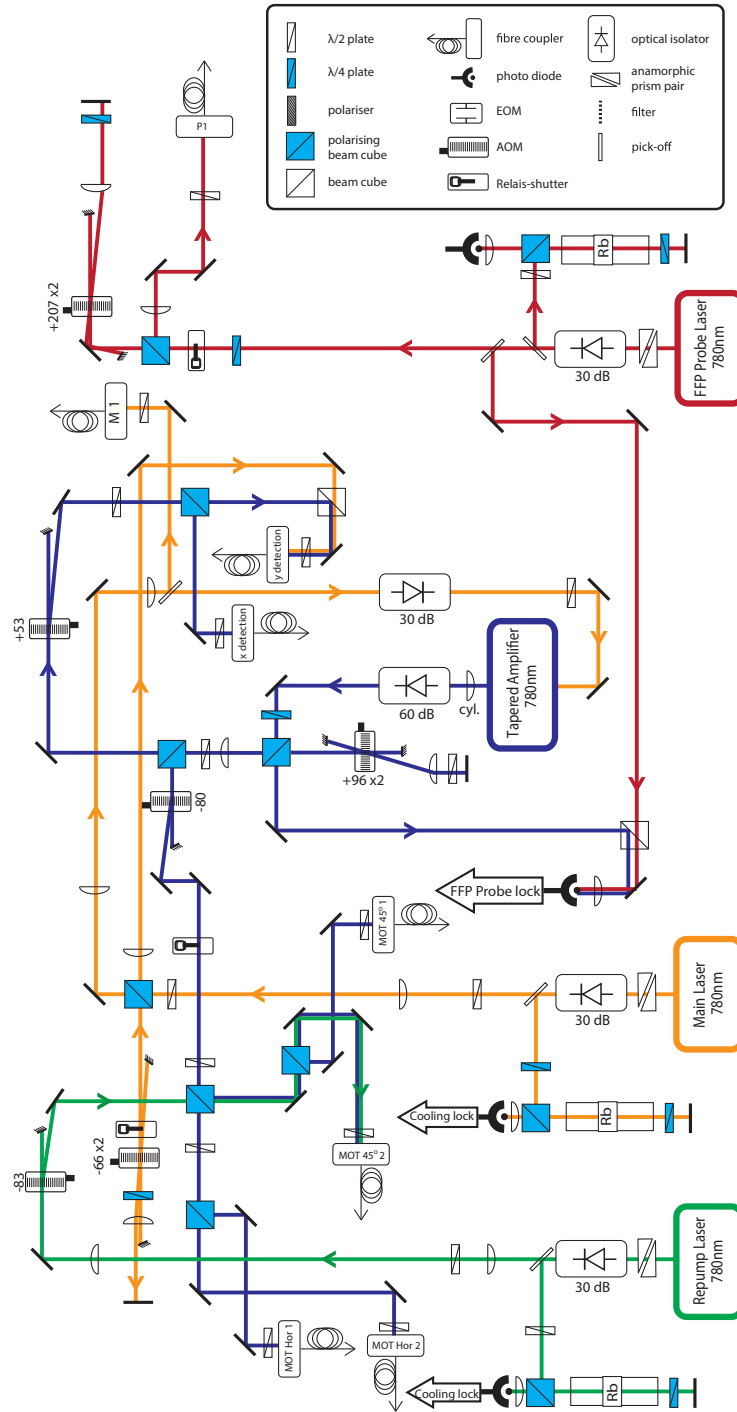
Figure 2.7: Beam paths on the main optical table. Light for MOT operation and imaging of the atoms is coupled into PMSM fibres leading to the optics surrounding the vacuum cell (see Figure 2.10). The probe light is sent to the "detection table" (see Figure 2.9). Numbers next to AOMs denote their frequency shift in MHz, numbers next to OIs their isolation in dB. Adapted from [45]

Figure 2.8: Beam paths on the "locking" table. For a legend of the symbols, see Figure 2.7. Adapted from [45].

Figure 2.9: Beam paths on the "detection" table. For a legend of the symbols, see Figure 2.7. Adapted from [45].

dipole light. The rest of the dipole laser light is sent to the detection table where it is coupled to the FFP2 cavity.

The length of the science cavity FFP1 is locked to the dipole laser frequency. We note that the lock chain provides two ways of shifting the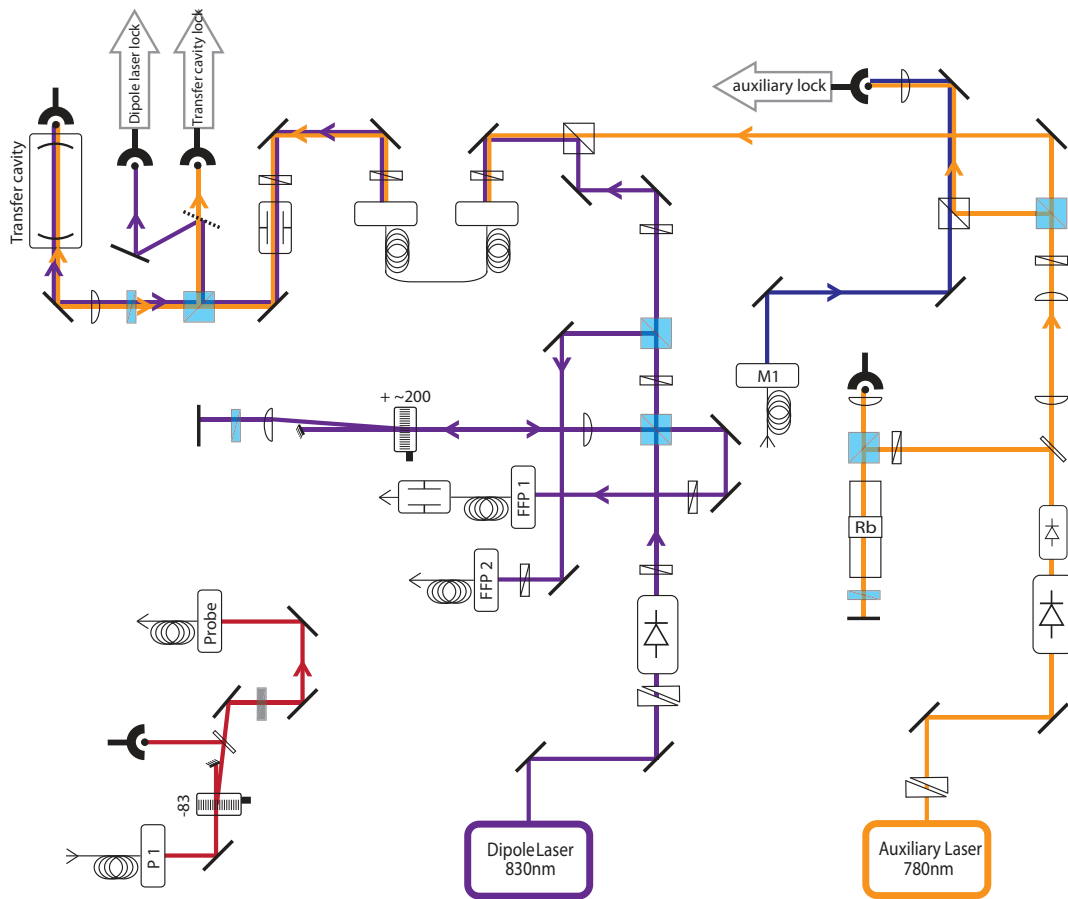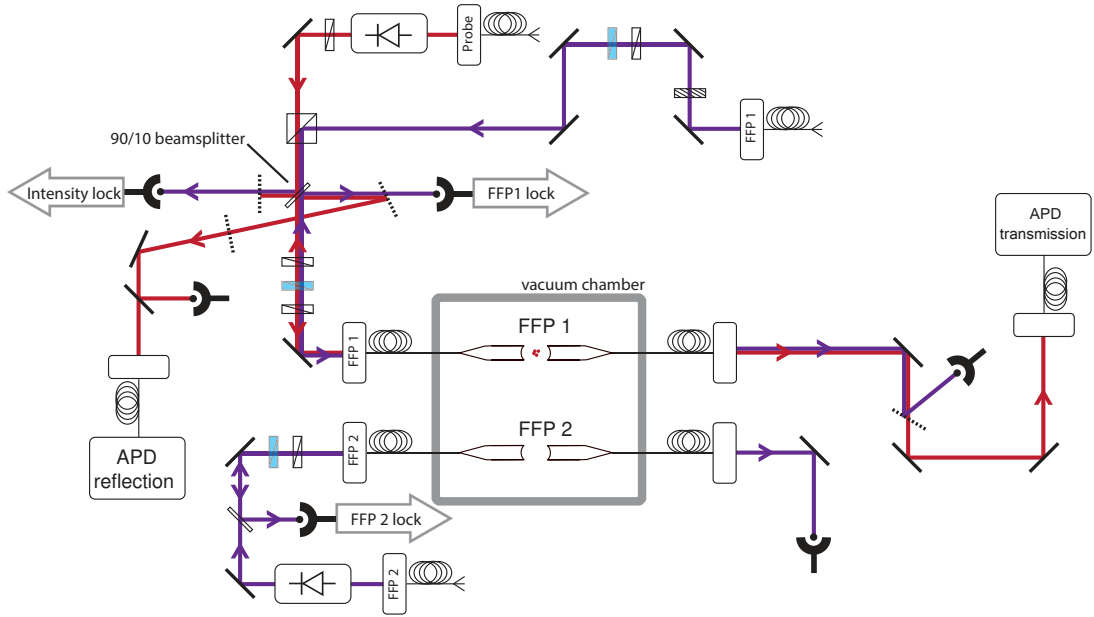 resonance frequency of FFP1 during the experiment, first by changing the lock point of the offset lock between aux and main laser (which provides a range of up to 1 GHz, with a speed of about 500 MHz/20ms, not addressed by the real-time microcontroller[8]), second by changing the double-pass AOM frequency (with a range of about 100 MHz, addressed by the microcontroller[8]).

The locking table also holds some components for the **probe** light. The probe power can be controlled by varying the RF power sent to an AOM at a fixed frequency of $+83\,\mathrm{MHz}$. In particular, the AOM serves to switch the probe on and off to create the Zeno light pulse as detailed in Section 2.7.2. After the AOM, the probe light is monitored with a PD and sent to the "detection" table.

2.5.3 Detection table

The detection table comprises all optical components necessary to control and monitor the way dipole and probe light beams are transmitted and reflected by the two fibre cavities. The beam paths are shown in Figure 2.9.

---

[8]The different experiment control schemes are explained in Section 2.6.

The dipole and probe light beams for FFP1 coming from the locking table are overlapped and coupled into the resonator. A set of wave plates allows us to control independently the polarisation of dipole and probe light so that they can be aligned with respect to the cavity's polarisation eigenaxes (cf. Section 2.3.1). A beam splitter and several filters are employed to send 90% of the incoming dipole light to a PD used to stabilise its intensity[9] and to send 90% of the light reflected from the cavity to a PD to lock the length of FFP1 to the dipole light frequency in a PDH scheme. The reflected probe light is detected with either a PD or an avalanche photodiode (APD)[10]. The dipole (probe) light transmitted from FFP1 is analysed with another PD (another SPCM).

In the present experiments, FFP2 is used to help locking FFP1. An important source of cavity length fluctuations are temperature changes (for example due to ohmic heating from the chip wires varying during the experimental sequence). As these thermic drifts act very similarly on both fibre cavities, the error signal of the length stabilisation of one can be used to stabilise the other. During the experimental sequence, this is important when loading the atoms from the magnetic trap into the dipole trap inside FFP1. For this transfer to be efficient, the dipole light needs to be switched of briefly while the atoms are brought into the correct position. During this time where there is no lock signal from FFP1, its length is stabilised with the error signal from FFP2. We note that the error signal from FFP2 is obtained directly from the reflected light intensity. In a situation similar to the tilt-locking scheme [82], the light coupled to the cavity excites both the TEM_{00} and a higher order spatial mode which results in a reflection signal with a dispersive feature suitable for locking.

2.5.4   Optical setup at the vacuum cell

The optical components surrounding the vacuum cell are shown schematically in Figure 2.10. They serve to distribute the MOT, detection and pump light brought by the fibre cables from the main table. The MOT beams are collimated to a diameter of about 2.5 cm. The two horizontal ones are overlapped with the x-detection and the pump beam. Figure 2.10 b illustrates the geometric constraints that impose a certain distance of the MOT position from the resonator bridge due to the size of the two 45° beams for the mirror MOT. Position and direction of the y-detection are also determined by the space available for the collimating optics and the cameras[11].

2.6   Experiment control

The experiment is controlled by a personal computer equipped with two interface systems. The main experimental control consists of a home-developed script language

---

[9]The dipole light intensity is stabilised in an analogue feedback circuit using this PD as sensor and the RF power to the double-pass AOM on the locking table as actuator.

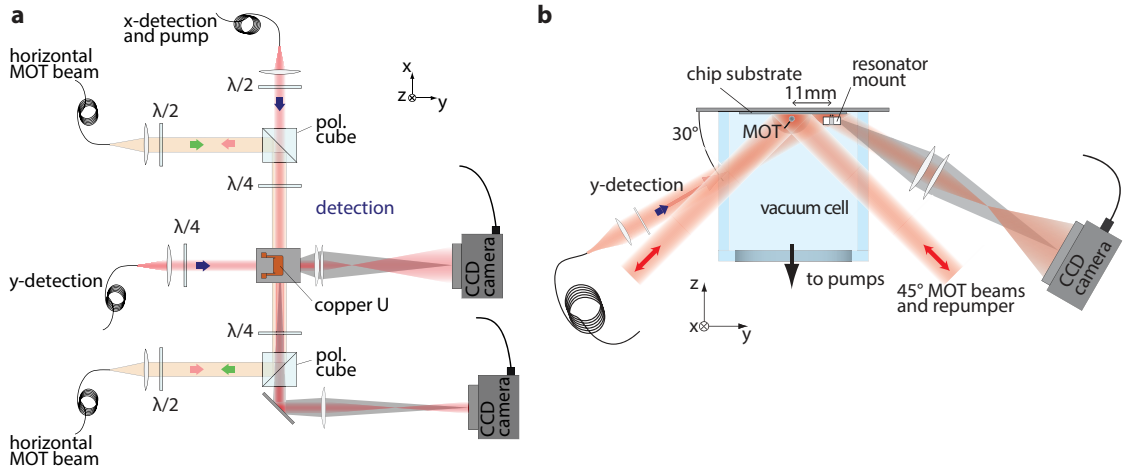[10]Perkin-Elmer SPCM AQR-14.

[11]JAI CV-M50-IR.

Figure 2.10: Schematic of the optics surrounding the vacuum cell. a) Top view showing in particular the two horizontal MOT beams. b) Side view. The position of the mirror-MOT is constrained by the condition that the resonator bridge should not clip the 45° beams. y-detection is used for absorption imaging of the MOT region, x-detection of the resonator region. Adapted from [63].

("GoodTime") that is used to program digital I/O boards[12] to address the current sources, AOM drivers, shutters etc. as well as some GPIB devices and the MW source. These control sequences are static and cannot react to experimental results, which makes them sufficient to load a cold sample into the cavity but not adequate for subsequent manipulations such as the atom number preparation described in Section 2.8.5. In [59], our setup was therefore complemented with a second control interface in the form of a real-time microcontroller[13] which provides several digital and two analogue outputs.

2.7   Modifications

This section details the two most important modifications made to the experimental setup during the present thesis in order to realise the QZD experiments. An improved cooling system based on a tapered amplifier (TA) has allowed us to reduce the experimental cycle time from 9 s to less than 4 s, as described in Section 2.7.1. The apparatus to create the synchronised light and MW pulses for the quantum Zeno dynamics is described in Section 2.7.2.

We note at this point that the experimental setup had not been in use for more than one year prior to the present work. Part of setting up the experiment therefore consisted in bringing the apparatus back to working condition. We found that a number of components had to be replaced, namely several RF components in the main-probe beat lock

---

[12]National Instruments PCI-3360 and PCI-4820.
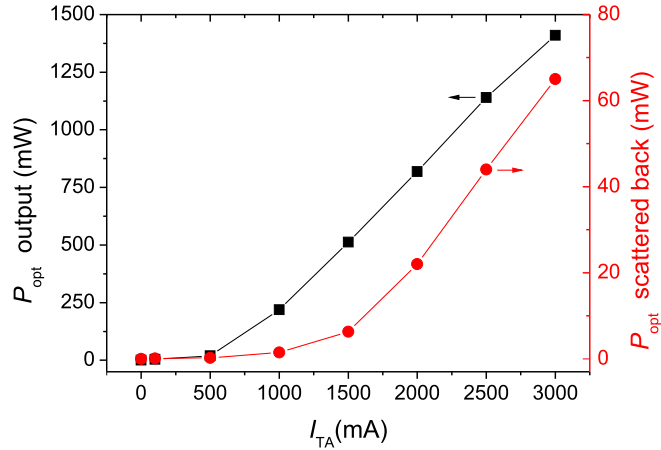[13]Jäger GmbH ADwin light with digital I/O extension card.

Figure 2.11: Optical power P_{opt} at output (black squares) and scattered back into input direction (red circles) of the TA as a function of the operating current I_{TA}. The TA was injected with 17 mW of optical power.

(see also Appendix B), AOM driving electronics and current sources used on the chip wires. After accounting for the problems caused by these external components, the core of the apparatus needed no major adjustments of the experimental parameters.

2.7.1 Improved experimental cycle time

To perform quantum state tomography on the atomic ensemble it is necessary to take a large number of individual measurements. As detailed in Section 3.1, we need on the order of 10^4 individual samples to acquire sufficient statistic for one 2d state tomography measurement. The experimental cycle time is therefore a critical parameter for the practical realisation of our measurement scheme. In the current implementation, we need to produce a new atomic sample for every measurement as there is no feasible way to reinitialise and reuse the sample. The longest part of the experimental cycle is the MOT phase which, prior to the work presented here, took 6 s.[14] In contrast, once the atoms are in the first magnetic trap, it takes only about 500 ms to have the ultracold ensemble ready inside the cavity, a few hundreds of μs to perform the QZD manipulations, about 100 ms to prepare for the next cycle and 1 s for the control software to reset.

The purpose of the MOT is to provide enough atoms for the subsequent experiment. In our case, we need to have around 10^3 atoms after evaporative cooling (see Section 2.8.1). The number of atoms captured in a MOT operated for some fixed time increases with the optical power of the cooling beams [83, 84]. Previously, the cooling beams were generated from an additional "slave" diode laser on the main table which was injection-

---

[14]Additionally, there was an unnecessary waiting time of about 1 s in the interaction of the main experiment control software with the MW control software which we have eliminated.
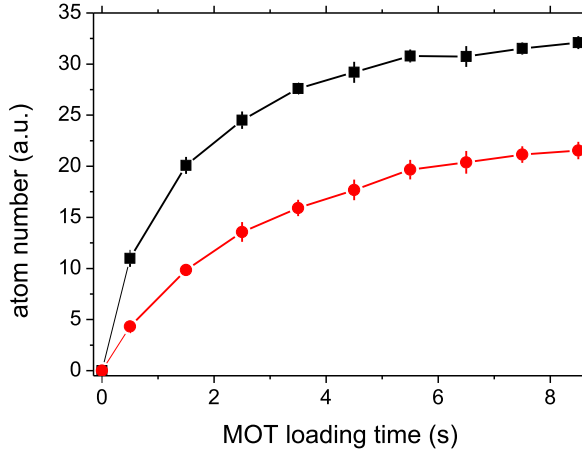
Figure 2.12: Captured atoms in the MOT as a function of the loading time. Black squares: cooling power 230 mW as in the new TA configuration. Red circles: cooling power 40 mW as in the old master-slave laser configuration. The atom number is extracted from absorption imaging which was not calibrated correctly to give absolute values. The dispenser current was $I_{disp} = 3.45\,\mathrm{A}$.

locked to the "master" main laser diode laser. The slave had an optical ouput power of 120 mW which resulted in 40 mW available for coupling into the fibre cables for the MOT, or about 8 mW each in the horizontal beams and 4 mW each in the 45° beams.

We have replaced the slave laser diode with a tapered amplifier (TA) specified to provide around 1 W of optical output power [15]. The amplifier module is mounted in a home made copper piece carrying the input and output collimating lenses[16]. The mount is placed inside a case that includes a Peltier element for temperature stabilisation and a circuit board to connect to standard laser current drivers. The output beam is asymmetric and astigmatic which we compensate with a cylinder lens. Figure 2.11 shows the output power P_{opt} measured directly after the TA as well as the light scattered back into the input direction due to spontaneous emission. The TA performs as specified, delivering about 1.4 W output at its maximum specified current $I_{TA} = 3\,\mathrm{A}$. To prolong its lifetime, we operate it below the maximum output. The light scattered back into the input direction attains several tens of mW. We therefore protect the main laser with a $35\,\mathrm{dB}$ optical isolator[17] on the input side of the amplifier (in addition to the 35 dB OI directly after the laser). To protect the TA from the light coming back from the double-pass AOM, we introduce a double-stage optical isolator[18] (specified isolation $> 60\,\mathrm{dB}$) at its output. In the experiment, we operate the TA at $I_{TA} = 2.55\,\mathrm{A}$ injecting it with $17\,\mathrm{mW}$ of light from the main laser. We then have an optical power of about 1.2 W after the

---

[15]Eagleyard Photonics EYP-TPA-0780-1000.
[16]Thorlabs molded glass aspherics, EFL 2.0 mm.
[17]IO-5-780-PBS.
[18]Linos Dl1-1.

two-stage OI, 340 mW after the double-pass and 230 mW to couple into the MOT fibre cables, about six times the amount of the old configuration. Figure 2.12 shows the atom number captured in the MOT as a function of loading time for the two different cooling powers. As can be seen, the higher power allows us to shorten the MOT loading phase from 6 s to 2 s to capture the required number of about 10^7 atoms.

2.7.2 Control of the probing light pulses

To implement the QZD, we need to produce synchronised pulses of probe light and microwave (MW) radiation, as detailed in Section 4.1. The realisation of the MW pulses for qubit manipulation is the same as in previous work and has not required any modifications. Our MW system is home-built and described in [59]. In principle, the MW is generated by adding the signal of an oscillator at 6800 MHz to that of a direct-digital-synthesizer (DDS) at 1-500 MHz. The DDS has 4 channels which can be programmed by a PC and then subsequently switched in real-time via TTL signals. The resulting MW signal is amplified by 51 dB resulting in a power of about 15 W that is sent to the antenna placed close to the vacuum cell.[19] A TTL-controlled switch allows us to switch the MW output on and off with a rise time below 10 ns.

During the experiment, we use TTL signals generated by the real-time micro-controller to realise MW pulses of well defined phase (by switching between the DDS channels) and length (via the TTL switch).

The synchronised probe light pulses need to be:

- short (duration on the order of a Rabi period, which is $< 10\,\mu$s in our experiment);

- variable in power (as we want to study the influence of measurement strength on the QZD);

- stabilised in power (as the experiment requires taking statistics for up to several days).

We can satisfy these requirements with the existing apparatus with only minimal modifications to the optical setup but some additional control components shown schematically in Figure 2.13. The principle is to modulate the probe beam power by varying the RF power sent to the single-pass AOM on the locking table. Such a scheme was already implemented previously to stabilise the optical power of the probe beam by acting on a voltage-controlled attenuator for the RF. The lock is implemented as a sequence on the the real-time controller; at the beginning of each experimental cycle, the power is adjusted until the reflection counts from the off-resonant cavity correspond to the pre-determined set-point value. We now implement a copy of this locking scheme, allowing for two different set-points for the optical probe power (corresponding to two different

---

[19]The MW pulses for the adiabatic transfer described in Section 2.8.4 are generated with an additional MW source (Agilent E8257D). The output of both MW sources is combined with a directional coupler (Pasternak Enterprise PE2204-30) and the combined signal sent to the amplifier chain.
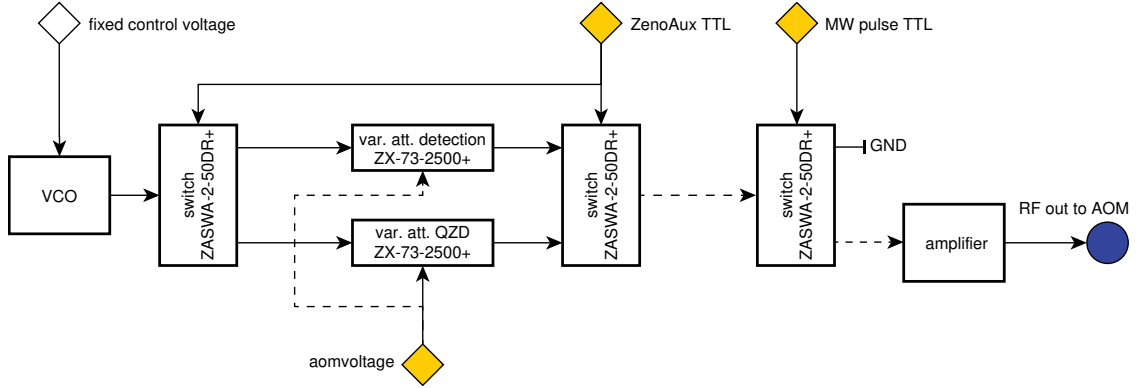
Figure 2.13: Simplified schematic of the RF electronics to regulate the probe intensity during the QZD. All components are from Minicircuits. Yellow diamonds indicate input from the real-time micro-controller. The analogue "aomvoltage" gives the feedback to stabilise the optical power of the probe either for the QZD or detection. The digital "ZenoAux" switches between the attenuators. The digital "MW pulse" synchronises the light pulse with the MW pulse during the QZD. Dashed arrows indicate omitted additional components which are necessary to work around different technical limitations. A complete schematic and full description can be found in Appendix C.

attenuator control voltages). One set-point is for the probe power corresponding to the measurement process that induces the QZD (which varies with the experiment), the other for detection of the atomic state in the cavity (which is the same in all experiments, but necessary to compensate intensity drifts of the probe power occurring on the time scale of several minutes). In the experimental sequence, we want to switch as quickly as possible from the QZD measurement power level to the detection power to shorten the time until detection which reduces the effect of decoherence. The variable attenuator is too slow for our purposes (specified fall time $25\,\mu$s), we therefore use two switches (response time around $10\,$ns) to change quickly between two different attenuators. To synchronise the QZD light pulse with the MW pulse, we use an additional switch which takes as TTL input the same signal used for switching the MW on and off.

Figure 2.14 shows typical signals illustrating the probe light pulses used during the QZD sequence. As can be seen, the probe power during the QZD is much stronger than during the detection. Nonetheless, due to the two-attenuator setup, both pulses are to good approximation rectangular. Using a single attenuator, the detection pulse would start at a higher intensity and then settle towards its target value. This increase would depend on the strength of the QZD pulse and change the count rates during the detection by up to 50% for our parameters.
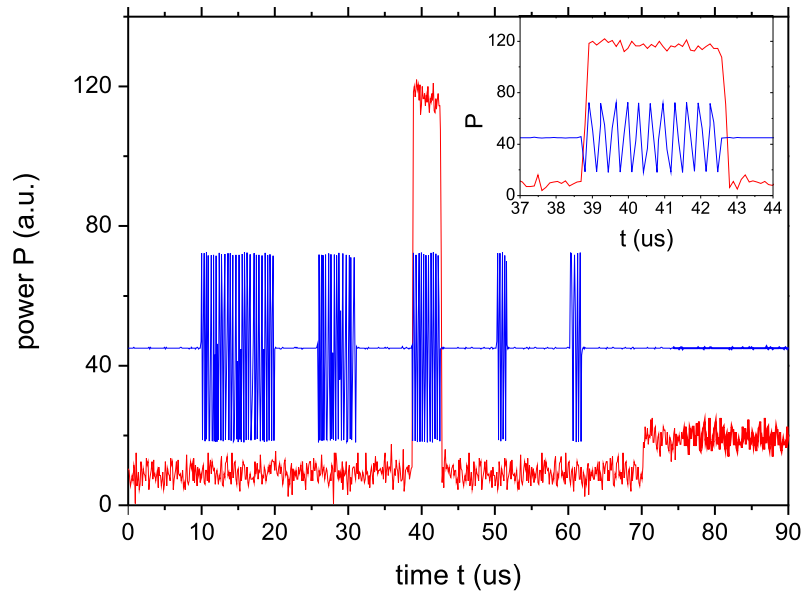
Figure 2.14: Oscilloscope traces showing the timing of the synchronised MW (blue) and probe light (red) pulses during the experimental sequence that produces the QZD. To visualise the MW at 6.8 GHz, it is mixed with a signal at a similar frequency to obtain a beat signal with an envelope following the pulse shape. The first three pulses correspond to the state preparation. During the third MW pulse, the probe light is switched on to induce the QZD. The following two MW pulses rotate the atomic state for the tomographic measurement which is performed with the subsequent (weaker) light pulse (which is in total $120\,\mu$s long). A detailed description of the complete sequence is given in Section 4.2.2.

2.8 Coupling a sample of cold atoms to the cavity

This section details how we prepare the atomic ensemble used for the experiments. First, we produce a sample of cold atoms by means of a MOT and evaporative cooling on the atom chip. The sample is then loaded into an intra-cavity dipole trap, placing it at the position of strongest coupling with the probe light field in the cavity. Finally, we prepare the ensemble to contain a well defined number of atoms.

2.8.1 Cold atom preparation

We start by capturing atoms in a first MOT produced with a bias field from the external coils and a magnetic quadrupole field from the copper U piece above the atom chip. The centre of this MOT is about 4 mm away from the surface of the atom chip (compare Figure 2.10 b). The atoms are then transferred into a MOT whose quadrupole field is generated by an U-wire on the base chip (compare Figure 2.1). The centre of this "chip MOT" is brought to a distance of about 0.8 mm from the surface of the science chip. After a phase of optical molasses, the atoms are then optically pumped into the state $|F = 2, m_F = 2\rangle$ and loaded into a first magnetic trap ("Trap1"[20]) formed by an external bias field and the P-trap wire (see Figure 2.15 showing a schematic of the science chip wires used during atom preparation).

By changing the orientation of the bias field, the main axis of the quadrupole trap generated by the P-wire can be rotated to transfer the atoms efficiently into a trap generated by the waveguide wire and an external quadrupole field [85] (Trap3). By varying the zero point of the external quadrupole field, the waveguide can then be used to move the atoms about 11 mm towards the cavity region (Trap4).

To be able to load the cloud of cold atoms into the cavity, its size and temperature needs to be reduced. The atoms are therefore first loaded into a Z-type trap formed by the Ioffe wire while a current through the stop wire creates a barrier that prevents the cloud from colliding with the cavity fibres (Trap5). This barrier in place, the Ioffe trap is compressed to move it closer to the chip and the dimple wire is used to create a dimple trap (which the atoms cannot reach yet) close to the final position the resonator (Trap6). Next, the current through the stop wire is turned off, and the atoms collect in the dimple trap where they are cooled via RF-evaporation (Trap7). Now follows the transfer into a pure dimple trap and a second phase of evaporative cooling (Trap8). For reference, Table 2.2 shows typical values for the number of atoms in the ultracold sample up to this point in the preparation sequence.

After the second RF evaporation, the dimple trap is moved closer to the cavity (Trap9). Now the sample temperature can be reduced further by bringing the atom cloud close to the fibres which will lead to evaporative cooling by removing the hottest atoms through contact with the fibre surface [66] (Trap10). Trap11 consists of moving the dimple trap to

---

[20]We use the term "trap" to signify the complete parameter set of external magnetic fields and chip wire currents characterising each step of manipulating the atom cloud on the chip.
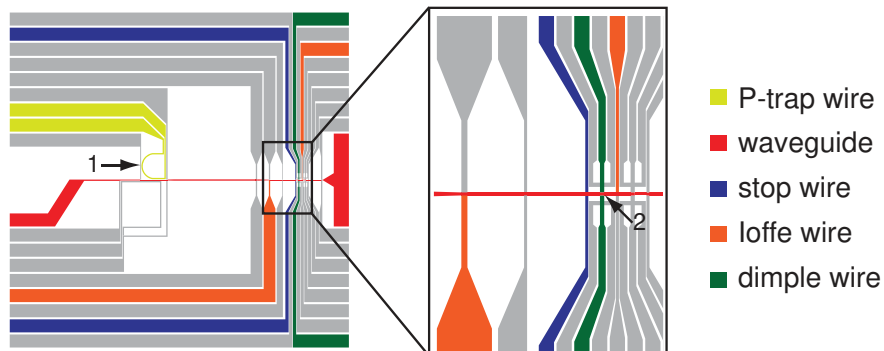
Figure 2.15: Wire configuration on the science chip highlighting wires used for the atom preparation sequence. The initial MOT and the first magnetic trap are at position 1, the centre of the science FFP resonator is at position 2. Adapted from [62].

experimental phase	N_{at}
chip MOT after molasses	$20 \cdot 10^6$
chip MOT after pumping	$20 \cdot 10^6$
in Trap1	$5.5 \cdot 10^6$
in Pturn	$5 \cdot 10^6$
in Trap3	$4.5 \cdot 10^6$
in Trap5 (after quadrupole transport)	$1.3 \cdot 10^6$
in Trap6	$1.3 \cdot 10^6$
in Trap7 (after first RF evaporation)	2000
in Trap8 (after second RF evaporation)	1200

Table 2.2: Characteristic parameters for the preparation of cold atomic samples. The table gives typical values for the number of atoms N_{at} extracted from absorption imaging.

position the atoms into the exact desired position for loading into the dipole trap (which needs to be switched off during that time). The general preparation sequence then ends with loading the atoms into the dipole trap by ramping its intensity up (Trap12) and ramping down the magnetic fields and wire currents (Trap13).

2.8.2 Dipole trap depth

The choice of the dipole trap depth is influenced by two considerations. On the one hand, the dipole laser power needs to be strong enough to give a useful error signal for the lock of FFP1 throughout the sequence. On the other hand, higher trap depth leads to the ensemble of atoms having higher temperature after the atom number preparation scheme described in Section 2.8.5. This higher temperature translates into faster decoherence. In our experiments, we load the atoms into a dipole trap with a depth of approximately $U \approx 0.3$ mK. From previously performed measurements, we infer the average temperature of the trapped ensemble to be $T \approx U/6 = 0.05$ mK. This is a factor of 10 lower than in previous experiments which increases the experimental coherence time by about an order of magnitude while still providing a stable locking signal. We estimate the trapping frequencies along and perpendicular to the trap axis to be $\omega_{axis} \approx 2\pi 300$ kHz and $\omega_\perp \approx 2\pi 15$ kHz respectively.

2.8.3 Position of the atoms in the resonator

As mentioned in Section 2.1, FFP1 is constructed so that dipole light and probe light both feature an antinode at the geometric centre of the cavity. In previous experiments, atoms were loaded into this common central antinode. However, this is not the position of strongest coupling, since the cavity geometry is slightly asymmetric so that the position of the probe beam waist does not coincide with the centre of the cavity. To quantify how the coupling varies with the position along the cavity axis, we measure the transmission of the cavity with an ensemble of atoms in $F = 2$ and cavity and probe tuned to the transition $F = 2 \rightarrow F' = 3$. In this configuration, stronger coupling leads to longer lifetime and lower cavity transmission (compare Equation 1.50). Figure 2.16 shows the lifetime of the atoms and the normalised average cavity transmission when varying the position of the ensemble in Trap11. The lifetime shows a characteristic modulation with maxima spaced by $\simeq 6.5\,\mu$m. They correspond to maximal overlap between the dipole light at $\lambda_1 = 830$ nm and the probe light at $\lambda_2 = 780$ nm which occurs after multiples of the beat length $\lambda_{beat} = \frac{\lambda_1 \lambda_2}{2(\lambda_1 - \lambda_2)} \approx 6.4\,\mu$m . At positions $x \simeq -20\,\mu$m and $x \simeq 18\,\mu$m, the end surfaces of the resonator fibres lead to atom loss (in agreement with the resonator length of $d \simeq 39\,\mu$m). It can be seen that the coupling is not strongest in the central antinode but in an antinode at a distance of $\simeq 6\,\mu$m from one of the fibres which agrees with the distance of the waist from the SM fibre $d_1 \simeq 8\,\mu$m computed in Section 2.3.1. The cavity transmission is reduced strongly in the coupled atom-cavity system (see Equation 1.36). For the central antinode, we measure a normalised transmission $T/T_{max} = 2.7(6) \cdot 10^{-4}$, for the antinode closest to the waist
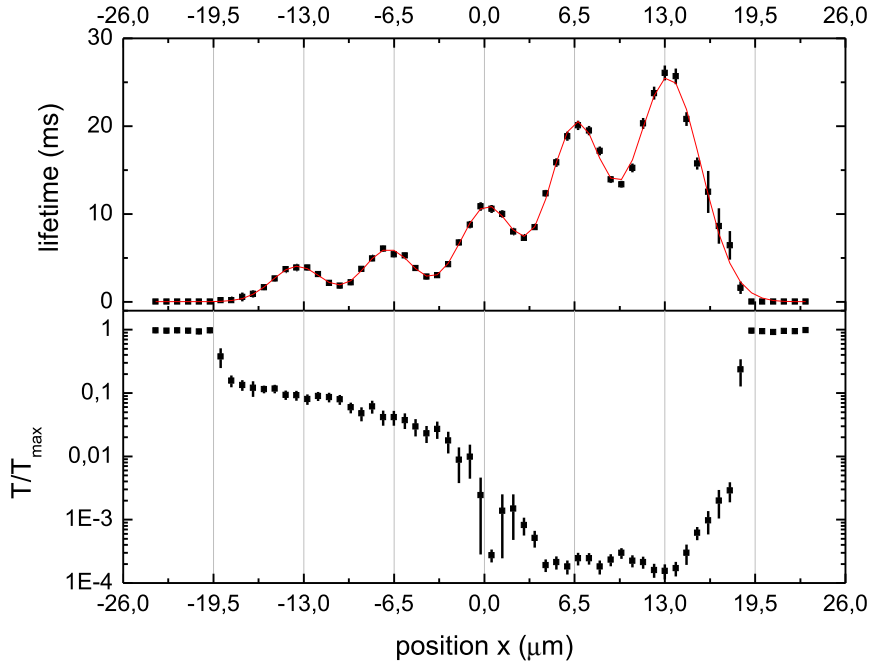
Figure 2.16: Lifetime of the atoms and cavity transmission as a function of the position x of the coupled ensemble along the cavity axis. Upper panel: With the probe light continuously on, lifetime is higher for higher coupling. The maxima correspond to positions where probe and dipole laser antinodes have maximal overlap. The coupling varies slowly with the diameter of the probe light mode which has its waist close to $x = 11\,\mu$m. The line is a guide to the eye. Lower panel: normalised cavity transmission T/T_{max} averaged over $100\,\mu$s, logarithmic scale. Atoms coupled to the cavity strongly suppress cavity transmission.

$T/T_{max} = 1.6(4) \cdot 10^{-4}$. In the present experiments, we load the atoms into this position of strongest coupling.

2.8.4   Zeeman state preparation

The experimental setup is not shielded against ambient magnetic field fluctuations; to minimise their impact on the stability of the qubit system, we have implemented it in the present work in the Zeeman states $|0\rangle \equiv |F = 1, m_F = 0\rangle$ and $|1\rangle \equiv |F = 2, m_F = 0\rangle$ which are to first order insensitive to the magnetic field. To initialise the atoms into the state $|0\rangle$, we apply three adiabatic MW sweeps to transfer them from the state $|F = 2, m_F = 2\rangle$ (in which they are loaded out of the magnetic trap into the dipole trap) first to the state $|F = 1, m_F = 1\rangle$, then $|F = 2, m_F = 1\rangle$ and then into $|0\rangle$. Since our MW source does not allow frequency sweeps, we keep the MW frequency fixed while varying the external magnetic bias fields to bring the Zeeman-shifted levels into

49

resonance with the MW.[21] Each sweep takes 3 ms to vary the bias field around $\pm 5\%$ of the resonant value. The transfer efficiency of the complete sequence is larger than 90%.

2.8.5 Atom number preparation

An ensemble of ultracold atoms loaded into the dipole trap as described so far does not contain a well defined number of atoms. To perform quantum state tomography, however, it is necessary to collect statistics over a large number of identical ensemble realisations. In our experiments, we therefore use a method to prepare ensembles of well-defined atom number that was developed in [45]. It is shown schematically in Figure 2.17. With the cavity and probe tuned to the $F = 2 \rightarrow F' = 3$ transition, we load about 150-200 atoms in $F = 1$ into the dipole trap. These atoms are far detuned from the cavity resonance $\Delta_{ca} = \Delta_{HFS} = 2\pi \cdot 6.8$ GHz. The field in the cavity is then given by Equation 1.35 with $\Delta_{ca} \gg g^2/\kappa$:

$$\langle \mathbf{a}^\dagger \mathbf{a} \rangle \approx \frac{\eta^2/\kappa^2}{\left(\frac{\Delta_{cp}}{\kappa} - \frac{g^2_{n_{F=1}}}{\kappa \Delta_{ap}} \right)} = \frac{\eta^2/\kappa}{\left(\Delta_{cp} - n_{F=1} \frac{g_1^2}{\Delta_{ap}} \right)} \,, \tag{2.4}$$

where $n_{F=1}$ is the number of atoms in $F = 1$. We see that the atoms act like a medium of different refractive index, shifting the cavity resonance by the amount $n_{F=1} \frac{g_1^2}{\Delta_{ap}}$ towards lower frequencies. The coupling constant g_1 takes into account the coupling to all transitions $F = 1 \rightarrow F' = 0, 1, 2$ and can be computed to be $g_1 = \sqrt{\frac{2}{3}} g^{\sigma^+}_{22 \rightarrow 33}$[59]. For our parameters, the light shift per atom evaluates to 5.6 MHz.

We now turn on the probe light and measure the cavity transmission which is initially low, as the atoms detune the cavity (left-hand side of Figure 2.17). However, the probe light induces light-assisted atom losses from the dipole trap through the mechanism of radiative escape [86]. As atoms get continually lost from the trap, cavity transmission increases. We monitor the rising transmission until it reaches the threshold corresponding to a certain atom number at which point we stop the loss process by switching the probe light off. By shifting the empty cavity resonance with respect to the probe before the preparation sequence, different atom numbers can be prepared. In the present experiments, we select a target number of 40 atoms by setting the cavity to be resonant with 20 atoms in $F = 1$ (we do this by locking the cavity to be resonant with the probe and then shifting the set-point of the beat lock between main and auxiliary laser by about 120 MHz before the preparation). We set the transmission threshold for the preparation to $\frac{1}{5}$ of the resonant value, which corresponds to the detuning caused by another 20 atoms.

---

[21]The MW source is operated at a fixed frequency of 6858 MHz. This frequency is about 24 MHz higher than the unperturbed transition $|F = 1, m_F = 1\rangle \rightarrow |F = 2, m_F = 2\rangle$, corresponding to the Zeeman shift caused by the magnetic field of about 12 G used to lift the degeneracy of the ground state levels.
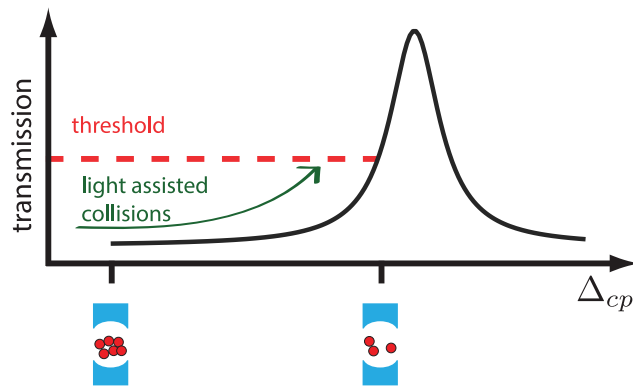
Figure 2.17: Principle of the atom number preparation scheme. The detuning between cavity and probe laser Δ_{cp} changes proportionally to the number of off-resonant atoms in the cavity. Removing atoms until the transmission crosses a certain threshold allows us to prepare a well-defined atom number. Source: [45].

Chapter 3

Quantum state tomography and entanglement detection

To understand the multiparticle atomic states created in our experiments and to make statements about their quantum features (such as entanglement), we need to know as much as possible about their quantum state. We therefore perform quantum state tomography to reconstruct the ensemble's density matrix from the measurements experimentally accessible to us. Section 3.1 describes our tomography method which is based on measuring the Husimi Q-distribution with the cavity. From 2d tomographic measurements of the $Q-$distribution, we reconstruct the symmetric part of the density matrix of the atomic ensemble as detailed in Section 3.2. To determine whether the states feature entanglement, we use two criteria described in Section 3.3, one based on the populations in the first two Dicke states and the other based on computing the quantum Fisher information.

3.1 Quantum state tomography

Our method is based on measuring the Husimi Q-distribution of the multiparticle state which describes its overlap with a coherent spin state. By coherently rotating the state, we can perform 2d tomography.

3.1.1 Coherent spin states

If the Dicke states introduced in Section 1.2.1 are the atomic counterpart to the electromagnetic field Fock states, the coherent field states have as analogon the coherent spin states (CSS) [87, 88]. The CSS $|\theta, \phi\rangle$ is the coherent superposition of all individual particle spins pointing in the same direction

$$|\theta, \phi\rangle = \bigotimes_{i=1}^{N} \left[\cos(\theta/2)|0\rangle_i + \sin(\theta/2)e^{i\phi}|1\rangle_i \right] . \tag{3.1}$$

The state $|\theta, \phi\rangle$ can also be understood as the result of operating a collective rotation operator $\hat{\boldsymbol{R}}(\theta, \phi)$ on the collective ground state:

$$|\theta, \phi\rangle = \hat{\boldsymbol{R}}(\theta, \phi)|0_N\rangle . \tag{3.2}$$

The CSS are completely symmetric and the most "classical" spin states, featuring no correlations between individual particles. Due to the uncertainty relation, the direction of the total spin of a CSS is not precisely determined. Instead, the spin direction is associated with fluctuations which for the CSS are isotropic in all directions perpendicular to the mean spin direction. In this sense, and similar to the optical coherent states, the CSS therefore have a finite extension and they are not orthogonal:

$$|\langle\theta'=0,\phi'=0|\theta,\phi\rangle|^2 = \cos(\theta/2)^{2N}\,. \tag{3.3}$$

It follows that the CSS form an overcomplete basis of the symmetric subspace $\mathcal{H}_s$:

$$\frac{N+1}{4\pi}\int \mathrm{d}\Omega|\theta,\phi\rangle\langle\theta,\phi| = \mathbb{1} \quad \text{with } \mathrm{d}\Omega = \sin\theta\mathrm{d}\theta\mathrm{d}\phi\,. \tag{3.4}$$

In the basis of Dicke states, the CSS set reads [89]:

$$|\theta,\phi\rangle = \sum_{n=0}^{N}\left(\frac{N!}{(N-n)!\,n!}\right)^{\frac{1}{2}}\cos(\theta/2)^{N-n}\sin(\theta/2)^n e^{-in\phi}|n_N\rangle\,. \tag{3.5}$$

3.1.2 Husimi Q-distribution and generalised Bloch sphere representation

To visualise multiparticle quantum states, it is useful to introduce the Husimi Q-distribution [90, 91]. It is a quasiprobability distribution defined in phase space that represents the overlap of the quantum state with a CSS. If the N-qubit quantum state is described by the density matrix ρ, the Husimi Q-distribution is defined as:

$$Q(\theta,\phi) \equiv \frac{N+1}{4\pi}\langle\theta,\phi|\rho|\theta,\phi\rangle = \frac{N+1}{4\pi}\langle 0_N|\hat{\boldsymbol{R}}^\dagger(\theta,\phi)\rho\hat{\boldsymbol{R}}(\theta,\phi)|0_N\rangle\,. \tag{3.6}$$

It follows directly that Q is non-negative, bounded and normalised:

$$0 \leq Q(\theta,\phi) \leq \frac{N+1}{4\pi}\,, \tag{3.7}$$

$$\int \mathrm{d}\Omega Q(\theta,\phi) = \mathbb{1} \quad \mathrm{d}\Omega = \sin\theta\mathrm{d}\theta\mathrm{d}\phi\,. \tag{3.8}$$

Given that the CSS form an overcomplete basis of the symmetric subspace $\mathcal{H}_s$, Q is equivalent to ρ in containing the full information of a state in the symmetric subspace.

The Q-distribution can be visualised on a generalised Bloch sphere of radius $J = N/2$. States in $\mathcal{H}_s$ then lie on the surface of the sphere, its south pole ($\theta = 0$) corresponds to the state $|0_N\rangle$ and its north pole to $|N_N\rangle$. Figure 3.1 shows the Q representation of several symmetric multiparticle states on the Bloch sphere. Figure 3.1a illustrates the finite extension of the probability distribution for the total spin direction of a given CSS
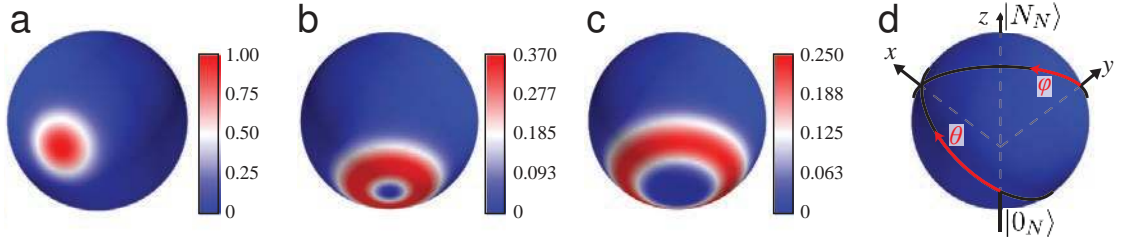
Figure 3.1: Depiction of multiparticle states on the generalised Bloch sphere. The pictures show $\frac{4\pi}{N+1}Q(\theta,\phi)$ for different states. a) CSS $|\theta = \frac{\pi}{4}, \phi = 0\rangle$ of 36 atoms. b) Dicke state $|n = 1_{N=36}\rangle$. c) Dicke state $|n = 3_{N=36}\rangle$. d) Coordinate system for a), b) and c).

$|\theta = \frac{\pi}{4}, \phi = 0\rangle$. The Q-distribution which is nothing else but a projection on CSS, is therefore limited in its resolution of the spin direction. This becomes clear in Figure 3.1b showing the Q-representation of the Dicke state $|1_N\rangle$. In the Dicke state, J_z is known precisely while J_x and J_y are undetermined. While the Q-distribution renders the latter fact well by showing a symmetric ring-like shape in x and y, its variance in z-direction (which is zero for a Dicke state) is smeared out (to $\sim 1/\sqrt{N}$). This also means that the Q-functions for different Dicke states (which are orthogonal) overlap, as can be seen comparing Figure 3.1b with Figure 3.1c showing the Q-representation of the Dicke state $|3_N\rangle$.

3.1.3 Measuring the Q-distribution with our cavity

As explained in the previous section, the Q-function of the state ρ at the angle (θ, ϕ) is a measurement of the overlap of ρ with the coherent spin state $|\theta, \phi\rangle$. Our cavity provides an immediate way to perform this measurement.

As described in Section 1.3.1, given an ensemble of N atoms in the cavity, we can distinguish between two situations: If all atoms are in the qubit ground state, which corresponds to the ensemble being in $\bigotimes_{i=1}^{N} |0\rangle = |0_N\rangle$, the cavity shows high transmission and low reflection. If at least one atom is in $|1\rangle$, the cavity shows low transmission and high reflection. The probability $p(|0_N\rangle)$ for the measurement outcome $|0_N\rangle$ directly gives the value of the Q-distribution at $(\theta = 0, \phi = 0)$:

$$Q(0,0) = \frac{N+1}{4\pi}\langle\theta = 0, \phi = 0|\rho|\theta = 0, \phi = 0\rangle = \frac{N+1}{4\pi}\langle 0_N|\rho|0_N\rangle = \frac{N+1}{4\pi}p(|0_N\rangle).$$
(3.9)

If we rotate the state ρ before the cavity measurement, we can determine the value of the Q-distribution at arbitrary angles:

$$Q(\theta,\phi) \equiv \frac{N+1}{4\pi}\langle\theta,\phi|\rho|\theta,\phi\rangle = \frac{N+1}{4\pi}\langle 0_N|\hat{\boldsymbol{R}}^{\dagger}(\theta,\phi)\rho\hat{\boldsymbol{R}}(\theta,\phi)|0_N\rangle.$$
(3.10)

Experimentally, the qubit states $|0\rangle$ and $|1\rangle$ correspond to the hyperfine states $|F = 1, m_F = 0\rangle$ and $|F = 2, m_F = 0\rangle$ of ^{87}Rb so that we can realise the rotation $\hat{\boldsymbol{R}}(\theta, \phi)$ using resonant MW pulses. Each individual measurement can only give the outcome 0 or 1. To obtain the expectation value $\langle \theta, \phi | \rho | \theta, \phi \rangle$, we repeat the measurement many times at the same angle (θ, ϕ). The experimental tomography procedure is detailed in Section 4.2.3 together with the complete experimental cycle.

What happens if the state ρ of the atomic ensemble in the cavity is not completely symmetric? To answer this question, we decompose ρ in the part ρ_s that lies in the symmetric subspace and the remaining part ρ_{ns} by introducing the projection operator P that projects on $\mathcal{H}_s$ and $\bar{P} = \mathbb{1} - P$:

$$\rho = (P + \bar{P})\rho(P + \bar{P}) = \underbrace{P\rho P}_{\rho_s} + \underbrace{P\rho\bar{P} + \bar{P}\rho P + \bar{P}\rho\bar{P}}_{\rho_{ns}} \,. \tag{3.11}$$

The crucial point is that the CSS $|\theta, \phi\rangle$ is symmetric so that

$$\bar{P}|\theta, \phi\rangle = 0 \,. \tag{3.12}$$

Inserting 3.11 and 3.12 into 3.10, we find

$$Q(\theta, \phi) = \frac{N+1}{4\pi} \langle \theta, \phi | (\rho_s + \rho_{ns}) | \theta, \phi \rangle = \frac{N+1}{4\pi} \left[\langle \theta, \phi | \rho_s | \theta, \phi \rangle + \underbrace{\langle \theta, \phi | \rho_{ns} | \theta, \phi \rangle}_{0} \right] \,. \tag{3.13}$$

Measuring the Q-distribution collects only information about the symmetric part of the density matrix of the atomic ensemble. We complement this result with the example of the state $|\psi_{sc}\rangle$ which describes one well-defined atom in $|1\rangle$ and all others atoms in the ensemble in $|0\rangle$. This state corresponds to the situation of one specific atom scattering a photon which makes it distinguishable from the others. In the qubit product basis, this state is $|\psi_{sc}\rangle = |10\ldots0\rangle$; in the basis of angular momentum eigenstates it reads [45]:

$$|\psi_{sc}\rangle = \frac{1}{\sqrt{N}}|1_N\rangle + \frac{1}{\sqrt{N}} \sum_{i=1}^{N} |J = N/2 - 1, m = -(N/2 - 1)\rangle_i \,. \tag{3.14}$$

Only the first term in 3.14 contributes to the Q-distribution so that the state appears as the first Dicke state with a reduced amplitude.

3.2 Maximum likelihood quantum state reconstruction

As detailed in the previous section, knowledge of the full Q-distribution of a multiparticle quantum state amounts to having complete information about the symmetric part of its density matrix. However, deducing the density matrix from experimental observations can be a delicate process [92]. Let us assume that the quantum state ρ can be fully

measured by performing projective measurements $\{|y_i\rangle\langle y_i|\}$ with M different possible outcomes:

$$\sum_{i=1}^{M} |y_i\rangle\langle y_i| = \mathbb{1}\,. \tag{3.15}$$

In principle, ρ will then give the measurement results

$$p_i = \langle y_i|\rho|y_i\rangle\,, \tag{3.16}$$

which could be inverted to determine ρ. The probabilities 3.16, however, correspond to an infinite amount of repetitions for each measurement i. In our case, the inversion would also require to measure $Q(\theta,\phi)$ for all angles (θ,ϕ) on the Bloch sphere [93]. These conditions are obviously impossible to realise experimentally. In practice, the experimenter can only measure frequencies:

$$f_i \xrightarrow{\infty\,\text{measurements}} p_i\,, \tag{3.17}$$

which are subject to statistical and systematic errors. Inverting 3.17 instead of 3.16 can be sensitive to noise and errors [94] and produce artefacts such as unphysical density matrices [95].

The problems associated with the inversion technique can be avoided by using a maximum likelihood (ML) approach to reconstruct the density matrix [95]. Where the inversion aims at finding the quantum state determined by the probabilistic frequencies observed, the ML method amounts to finding the quantum state that is most likely to have produced the observed data. Such a method was implemented previously in our group. There, however, it was limited to the reconstruction of the diagonal elements of the density matrix [45]. For the present experiments, we perform full 2d tomographic measurements which allow us to extend the reconstruction to all elements of the density matrix.

Implementation

To reconstruct the most likely density matrix, we employ the iterative algorithm described in [96]. Given the measurement operators 3.15 and the observed frequencies 3.17, we look for the density matrix ρ that maximises the likelihood functional

$$\mathcal{L}(\rho) = \prod_{i=1}^{M} \langle y_i|\rho|y_i\rangle^{f_i}\,. \tag{3.18}$$

In our case, we measure the Q-function at certain angles $\{|(\theta,\phi)_i\rangle\langle(\theta,\phi)_i|\}$ and the result can be either 0 or 1 so that 3.18 becomes

$$\mathcal{L}(\rho) = \prod_{i=1}^{M} (p_i^1)^{f_i^1} \cdot (p_i^0)^{f_i^0} \qquad p_i^1 = \langle(\theta,\phi)_i|\rho|(\theta,\phi)_i\rangle,\, p_i^0 = 1 - p_i^1\,, \tag{3.19}$$

where f_i^1 (f_i^0) is the frequency of measuring 1 (0) at angle $(\theta, \phi)_i$ normalised to the number of measurements at that angle. The density matrix ρ_m that maximises 3.19 can be found by introducing the operator $\boldsymbol{K}(\rho)$:

$$\boldsymbol{K}(\rho) = \sum_i \frac{f_i^1}{p_i^1} \boldsymbol{\pi}_i + \frac{f_i^0}{p_i^0} \left(\mathbb{1} - \boldsymbol{\pi}_i\right) \qquad \boldsymbol{\pi}_i = |(\theta, \phi)_i\rangle\langle(\theta, \phi)_i| \,. \tag{3.20}$$

We know that for ρ_m, $f_i^k \propto p_i^k$ so that $\boldsymbol{K}(\rho_m) \propto \mathbb{1}$. We can therefore start with an arbitrary density matrix (we use the identity) and iterating the series

$$\rho^{(k+1)} = \mathcal{N}\left[\boldsymbol{K}(\rho^{(k)})\rho^{(k)}\boldsymbol{K}(\rho^{(k)})\right] \,, \tag{3.21}$$

where $\mathcal{N}$ denotes normalisation to a unitary traces. In each step, the likelihood monotonically increases and the series asymptotically approaches ρ_m.

In our implementation of the ML algorithm, we account for the angle-dependent detection errors ϵ_i^{10} and ϵ_i^{01} introduced in the previous section by modifying 3.20 to read:

$$\boldsymbol{K}(\rho) = \sum_i \frac{f_i^1}{p_i^1}\left[(1 - \epsilon_i^{01})\boldsymbol{\pi}_i + \epsilon_i^{10}(\mathbb{1} - \boldsymbol{\pi}_i)\right] + \frac{f_i^0}{p_i^0}\left[(1 - \epsilon_i^{10})(\mathbb{1} - \boldsymbol{\pi}_i) + \epsilon_i^{01}\boldsymbol{\pi}_i\right] \,. \tag{3.22}$$

As reconstruction basis we choose the Dicke states and an additional state in the non-symmetric subspace which allows us to reconstruct ρ_s, the symmetric part of the multi-particle density matrix, with possibly non-unitary trace.

The reconstruction is associated with a certain statistical error due to the finite number of observations and the detection errors. We estimate this error with the bootstrapping method [97]. For each 2d tomography measurement, we create 1000 artificial datasets having the same number of samples with the same mean observed frequencies. Reconstructing these gives a set of resampled density matrices and therefore a distribution of values for each matrix entry. We report the standard deviation of the spread of this distribution as the statistical error of the reconstruction.

3.3 Assessing multiparticle entanglement

Entanglement between multiple quantum systems is a fundamental phenomenon of quantum mechanics and at the heart of many proposed applications of quantum technology. While the concept itself can be described in fairly simple terms, detecting and quantifying multiparticle entanglement is, in general, not straightforward. This section summarizes how, given a density matrix for an atomic ensemble, we detect entanglement by computing the quantum Fisher information and, for certain states, quantify it by means of a previously developed criterion.

3.3.1   Quantum entanglement

When initially separate quantum systems interact with each other, their resulting state can, in general, not any more be described in terms of the individual system states. This phenomenon, which is a consequence of the basic principles of quantum mechanics (namely coherent superposition), was pointed out by Schrödinger who described the systems as having become "entangled" by their interaction [15, 16]. Limiting ourselves to pure states for simplification, we can define [17]:

> An N-particle pure state $|\psi\rangle \in \mathcal{H} = \bigotimes_{i=1}^{N} \mathcal{H}_i$ is called entangled if it cannot be written in the form
>
> $$|\psi\rangle = \bigotimes_{i=1}^{N} |\varphi_i\rangle \qquad |\varphi_i\rangle \in \mathcal{H}_i \,. \tag{3.23}$$
>
> Otherwise, it is called fully separable.

From this definition, we can understand the origin of entanglement by considering the difference between classic phase space and the Hilbert space of quantum mechanics. In the classical case, the total state space for N identical particles is the Cartesian product of the individual spaces; its dimension scales linearly with N. In contrast, the total Hilbert space for N identical quantum systems is the tensor product of the individual Hilbert spaces which scales exponentially with N. It is exactly this scaling property that makes entanglement an interesting resource for quantum information applications [98].

On closer examination, entanglement between multiple particles is a complex concept. For example, according to 3.23, both the following three-particle qubit states are entangled:

$$|\text{GHZ}\rangle \;\; = \;\; \frac{1}{\sqrt{2}} \left[|000\rangle + |111\rangle \right] , \tag{3.24}$$

$$|\Psi\rangle \;\; = \;\; \frac{1}{\sqrt{2}} \left[|000\rangle + |110\rangle \right] = \frac{1}{\sqrt{2}} \left[|00\rangle + |11\rangle \right] \otimes |0\rangle \,. \tag{3.25}$$

In a way, $|\Psi\rangle$ is "less entangled" than the state $|\text{GHZ}\rangle$[1], as one particle can be factored out into a separated state. We therefore introduce the following definition of "partial entanglement" [100] [2]:

> For $k \leq N$, an N-particle pure state $|\psi\rangle$ is called k-particle entangled if it cannot be written in the form
>
> $$|\psi\rangle = \bigotimes_{l=1}^{m} |\varphi_l\rangle \qquad m \geq \frac{N}{k} \,, \tag{3.26}$$
>
> where the $|\varphi_l\rangle$ are states of maximally $k-1$ particles. Otherwise, it is called $(k\text{-}1)$-producible.

---

[1]States of this class were introduced by Greenberger, Horne and Zeilinger in [99].

[2]For a formally precise definition of k-particle entanglement, see [101]. A k-particle entangled state can also be described as having "depth of entanglement" k [102].

For a mixed state described by a density matrix ρ, these definitions can be extended through convex combination [100]. If we can write

$$\rho = \sum_i p_i |\psi_i\rangle\langle\psi_i| \, , \; p_i \geq 0 \, \forall i, \; \sum_i p_i = 1 \, , \tag{3.27}$$

with $|\psi_i\rangle$ at most $(k-1)$-producible, the state given by ρ is called $(k-1)$-producible. Physically, this means that ρ can be described by only $(k-1)$-producible pure states and statistical mixing. Consequently, a mixed state ρ contains k-particle entanglement, if and only if the correlations cannot be explained by assuming the presence of $(k-1)$-particle entanglement only.

A fully N-particle entangled state can therefore not even be decomposed into the product of two states $|\varphi_A\rangle \otimes |\varphi_B\rangle$ where A and B are disjoint subsets of $\{1, \ldots, N\}$. Applying the definition 3.26 to the state $|\Psi\rangle$ in Equation 3.25, we find that it is not 3-particle entangled but 2-particle producible.

Examples for fully entangled states are, for $N = 3$, the state $|\mathrm{GHZ}\rangle$ in Equation 3.24 as well as the W state (see Equation 4.3):

$$|1_{N=3}\rangle = \frac{1}{\sqrt{3}} \left[|100\rangle + |010\rangle + |001\rangle \right] . \tag{3.28}$$

Still, these two maximally entangled states belong into inequivalent classes [103]. Tracing out one particle in $|\mathrm{GHZ}\rangle$ produces a statistical mixture of separable two-qubit states, for $|1_{N=3}\rangle$, however, it results in an entangled 2-qubit state.

3.3.2 Quantum Fisher information

Entangled states are not only interesting for quantum information applications but also specifically for metrology purposes. Formulating the metrology process in terms of estimating an interferometric phase ϑ with a probe made of N quantum systems, the measurement error scales as $\Delta\vartheta \propto \frac{1}{\sqrt{N}}$ when the probe systems are uncorrelated. Using entangled states instead, this so-called standard quantum limit (SQL) can be undercut to improve the scaling towards $\Delta\vartheta \propto \frac{1}{N}$, the so-called Heisenberg limit imposed by the uncertainty relation [22]. Approaching the concept of entanglement from this perspective, the phase sensitivity of an arbitrary interferometric measurement strategy can shown to be given by the Quantum Cramer-Rao bound

$$\Delta\vartheta_{\mathrm{QCR}} = \frac{1}{\sqrt{F_Q(\rho)}} = \frac{\chi}{\sqrt{N}} \, , \tag{3.29}$$

where $F_Q(\rho)$ is the quantum Fisher information (QFI) of the state ρ used as input for the measurement [104] and $\chi = \sqrt{\frac{N}{F_Q(\rho)}}$. Let us consider an ensemble of qubits that can be assigned the operator $\boldsymbol{J}_{\vec{n}}$ describing a rotation of the total spin around the axis $\vec{n}$.

The QFI for this rotation is then:

$$F_Q(\rho, \boldsymbol{J}_{\vec{n}}) = 2 \sum_{i,j} \frac{(p_i - p_j)^2}{p_i + p_j} |\langle i | \boldsymbol{J}_{\vec{n}} | j \rangle|^2 \,, \tag{3.30}$$

where p_i and $\{|i\rangle\}$ are the eigenvalues and eigenvectors of the ensemble state ρ. Intuitively, $F_Q(\rho, \boldsymbol{J}_{\vec{n}})$ can be understood as a measure of the "speed with which the state ρ moves in Hilbert space" when performing the rotation $\boldsymbol{J}_{\vec{n}}$. For a state with high QFI, already a small change in the rotation angle ϑ corresponds to a difference in its position in Hilbert space that is large enough to be distinguished in a measurement subject to quantum uncertainty [105].

According to Equation 3.29, states with $\chi < 1$ achieve phase estimation better than the SQL. Indeed, the relationship between beating the SQL and entanglement of the probe state can be used to derive an entanglement criterion based on the state's QFI [106]:

The quantum state ρ of an ensemble of N qubits is particle entangled if

$$\chi^2 \equiv \frac{N}{F_Q(\rho)} < 1 \,, \tag{3.31}$$

where $F_Q(\rho, \boldsymbol{J}_{\vec{n}})$ is the QFI for a rotation around an arbitrary axis $\vec{n}$.

If the criterion 3.31 is fulfilled, the state ρ is (at least 2-)particle entangled and features a metrological useful gain over fully separable states.[3]

As detailed in the previous section, we can reconstruct the symmetric part ρ_s of the atomic state ρ. In the following, we show that $F_Q(\rho) \geq F_Q(\rho_s)$ and computing the quantum Fisher information in the symmetric subspace gives us a lower bound for $F_Q(\rho)$. We consider the completely positive trace preserving map M which transforms ρ into $M[\rho] = \Pi \rho \Pi + \bar{\Pi} \rho \bar{\Pi}$, where Π is the projector onto the symmetric subspace $J = N/2$ and $\bar{\Pi} = \mathbb{1} - \Pi$. Under a rotation of the atomic spin around the direction $\vec{n}$ by an angle θ, ρ transforms into $\rho(\theta)$. The quantum Fisher information associated with the measurement of the angle θ, which we denote by $F_Q(\{\rho(\theta)\})$, cannot increase under the action of M [108] and $F_Q(\{\rho(\theta)\}) \geq F_Q(\{M[\rho(\theta)]\})$. Because the norm of the atomic spin is conserved by rotations, we have $M[\rho(\theta)] = \rho_s(\theta) + \rho_{ns}(\theta)$, where $\rho_s(\theta)$ and $\rho_{ns}(\theta)$ are respectively the rotated symmetric part of the density matrix ρ_s and the rotated non-symmetric part of the density matrix $\rho_{ns} = \bar{\Pi} \rho \bar{\Pi}$. We thus conclude that

$$F_Q(\{\rho(\theta)\}) \geq F_Q(\{\rho_s(\theta) + \rho_{ns}(\theta)\}) = F_Q(\{\rho_s(\theta)\}) + F_Q(\{\rho_{ns}(\theta)\}) \,, \tag{3.32}$$

where the last equality comes from the additivity of the quantum Fisher information under direct sum [109].

We note that the QFI of the Dicke state $|n_N\rangle$ is [110]:

$$F_Q[n, N] = N \left(1 + \frac{N}{2} - \frac{2}{N}\left(n - \frac{N}{2}\right)^2\right), \tag{3.33}$$

which for $n = 0, 1, 2$ evaluates to $N, \approx 2.9N, \approx 4.8N$.

---

[3]Criteria that quantify multiparticle entanglement based on the QFI can be found in [107].

3.3.3 Spin squeezing

The concept of spin squeezing is similar to the QFI in the sense that it provides a way of characterising the sensitivity of quantum states for metrology applications and can serve to detect entanglement [111, 112]. For multiparticle spin systems, a squeezed state can be defined as achieving higher resolution in a Ramsey spectroscopy experiment compared to a coherent spin state [113]. According to this definition, the fluctuation of the spin component orthogonal to the mean spin direction $\Delta J_\perp^2$ needs to be below the value for the CSS $\Delta J_\perp^2 = J/2 = N/4$, which leads to introducing the spin squeezing parameter ξ and the following criterion:

A system of N spin-$\frac{1}{2}$ particles with total mean spin $\langle J \rangle$ is called spin-squeezed if

$$\xi^2 \equiv N \frac{(\Delta J_\perp)^2}{\langle J \rangle^2} < 1 \,. \tag{3.34}$$

We note that for the Dicke state $|n_N\rangle$, the spin squeezing parameter takes the value [112] $\xi^2 = (\frac{N}{n})^2 (1 + \frac{N}{2} - \frac{(N/2-n)^2}{N/2}) \geq 1$, which for $N = 36$ and $n = 0, 1, 2$ evaluates to $1, \approx 3.3, \approx 6.0$.

3.3.4 Entanglement criterion in the vicinity of the W state

The quantification of entanglement is, in general, not straight-forward [17, 114]. A convenient criterion for multiparticle states that are close to the W state was developed previously in our group. We employ this method in this work to analyse some of the states created by QZD and limit ourselves here to sketching its concept. It was first applied in [44] and is described in detail in [45].

Given a symmetric N-qubit state ρ in the basis of Dicke states, a lower bound for the depth of entanglement in the ensemble can be obtained from the populations ρ_{00} and ρ_{11} in the states $|0_N\rangle$ and $|1_N\rangle$. More precisely, for an ensemble of N qubits that is k-producible, ρ_{11} can only attain a certain maximum $C(N, k, \rho_{00})$ which depends on ρ_{00}. If ρ_{11} is higher than this threshold, ρ features at least $(k+1)$-particle entanglement. The function $C(N, k, \rho_{00})$ is plotted in Figure 3.2 for $N = 36$ and different k.
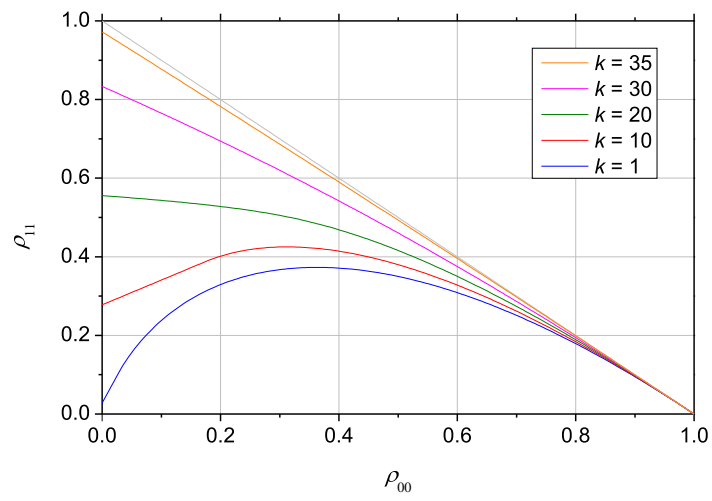
Figure 3.2: Entanglement criterion in the vicinity of the W state. States with ρ_{11} above a certain bound $C(N, k, \rho_{00})$ must be at least $(k + 1)$-particle entangled. The plotted curves are for $N = 36$ which is the ensemble size in the QZD experiments presented in Chapter 4.

Chapter 4

Creation of multiparticle entanglement through QZD

This chapter presents how we experimentally realise QZD to create multiparticle entanglement in an ensemble of several tens of atoms. Combining our cavity-based Zeno measurement with two different trajectories of the MW drive, we can realise different dynamics, one leading to entangled states close to the W state, the other offering the possibility for spin-squeezing. These schemes are presented in Section 4.1, where we also discuss the influence of experimental imperfections, notably due to finite measurement strength and spontaneous emission arising from the second cavity mode.

In practice, our experiments consist of a cycle that begins with the preparation of an atomic ensemble of well-defined atom-number and its initialisation in a well-defined quantum state. We then perform the actual QZD sequence and end with a detection phase in which we analyse the resulting state of the ensemble by performing quantum state tomography. The individual steps of this experimental cycle are described in Section 4.2.

The experimental results are presented in Section 4.3. We show that we realise dynamics that follows the basic model of unitary QZD introduced in the first chapter of this thesis. We analyse the multiparticle entanglement of the created atomic states and discuss the influence of finite measurement rate and the second polarisation mode in the cavity, showing that they can be reproduced by a model without any free parameters. We conclude by discussing the potential improvement expected from improved cavity parameters.

4.1 Deterministic entanglement generation by means of QZD

The general concept behind our experiments has already been presented in Chapter 1, the key point being that our cavity setup can produce a good approximation of an ideal projective measurement acting collectively on the ensemble of ^{87}Rb atoms coupled to the FFP cavity. Applying MW radiation to drive unitary qubit dynamics, while simultaneously probing the ensemble with the cavity, results in QZD. In the following, we present the specific experimental sequences we use to generate entanglement.
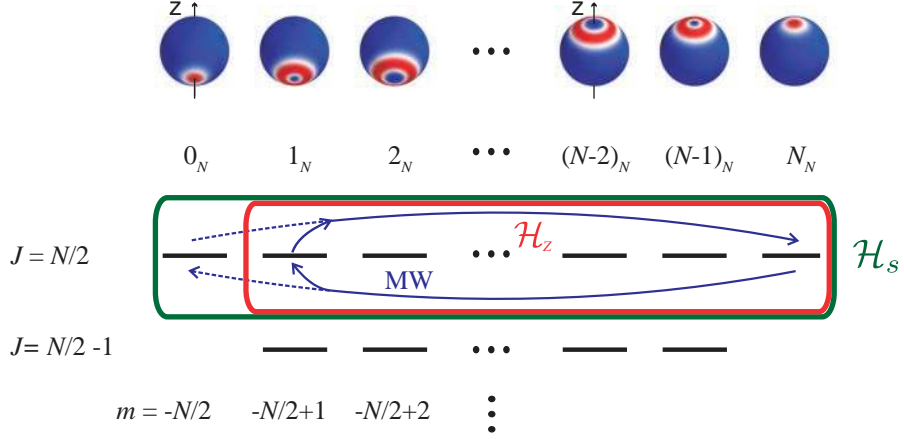
Figure 4.1: The Hilbert space of the symmetric atomic spin states $\mathcal{H}_s$ is spanned by the Dicke states $|n_N\rangle$ (compare with Figure 1.2). The top row shows the generalised Bloch sphere representations of the Husimi Q-distribution for some states $|n_N\rangle$. The MW induces dynamics within $\mathcal{H}_s$ (solid blue arrows); they are modified (dashed arrows) by probing the cavity transmission which corresponds to a projection on the state $|0_N\rangle$ or the complementary subspace $\mathcal{H}_Z$. See also Figure 1.7.

As detailed in Sections 1.2 and 1.3, the relevant Hilbert space consists of the symmetric states of the collective atomic spin $\mathcal{H}_s$, which is spanned by the Dicke states $|n_N\rangle$. Furthermore, we implement a cavity-based measurement that, under the conditions discussed in Section 1.3.2, distinguishes the state $|0_N\rangle$ (all atoms in $|0\rangle$, high transmission), from the subspace $\mathcal{H}_Z$ of all other states (low transmission), see Figure 4.1. Adopting a simplified description, the cavity measurement corresponds to a projection P, either on $|0_N\rangle$:

$$\hat{P}_0 = |0_N\rangle\langle 0_N|, \tag{4.1}$$

or on the complementary Zeno subspace $\mathcal{H}_Z$:

$$\hat{P}_{\mathcal{H}_Z} = \mathbb{1} - \hat{P}_0. \tag{4.2}$$

This projection gives rise to the QZD in our experimental system. In the following, we detail the general idea of our experiments: to observe the QZD that occur when taking the atomic system from a state close to $|N_N\rangle$, that is within $\mathcal{H}_Z$ and far away from the subspace boundary, towards the state $|0_N\rangle$.

Figure 4.2 displays the time-evolution according to Equations 4.1, 1.22 and 1.23 for two different initial states. In both cases, we start within $\mathcal{H}_Z$, close to the state $|N_N\rangle$ which has the lowest overlap with the state $|0_N\rangle$ outside $\mathcal{H}_Z$ and drive a rotation of the collective spin around the x-axis with Rabi frequency $\Omega = \pi/T$.

The first trajectory (I) starts in $|N_N\rangle$, a coherent spin state at the north pole of the Bloch sphere. This trajectory passes exactly through the south pole of the Bloch sphere.
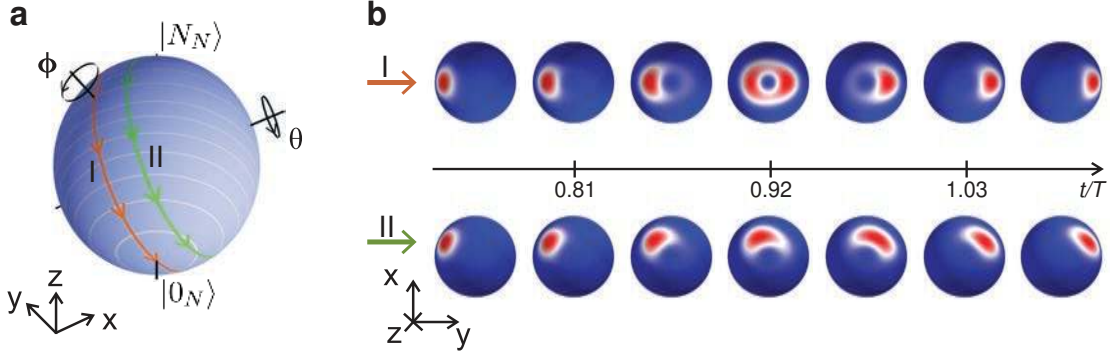
Figure 4.2: Unitary QZD induced by the cavity measurement for two different traject-ories on the generalised Bloch sphere. a) Trajectory I follows a meridian from $|N_N\rangle$ at the north pole of the sphere through $|0_N\rangle$ at the south pole. Trajectory II starts with a state that is slightly displaced from the north pole and follows a smaller circle around the sphere, passing not exactly through the south pole. b) Calculated Husimi Q-distribution of the atomic state ($N = 36$) at certain times t close to the π-pulse time T in the presence of measurement. For Trajectory I (upper row), there is no initial rotation $\phi_d = 0$, for Trajectory II (lower row) $\phi_d = \pi/10$.

As evident in the top panel of Figure 4.2b, in the presence of the cavity measurement, the Husimi Q-distribution of the atomic state is strongly modified when the state comes close to the boundary of $\mathcal{H}_Z$. Specifically, as the QZD does not allow the atomic state to populate $|0_N\rangle$, it builds a high overlap with the state $|1_N\rangle$, visible in the characteristic ring shape of the Q-distribution in the top central frame in Figure 4.2b. At this position of highest overlap with $|1_N\rangle$, the mean spin points in the direction $-z$. We note that during QZD, this does not occur at $t = T$, as is the case during regular Rabi dynamics, but at an earlier time. We have already seen in Section 1.2 that this faster dynamics is a typical feature of QZD.

The Dicke state $|1_N\rangle$ is also known as "W state" [103]. It describes one atomic excitation shared symmetrically between N particles and can be written in the qubit product basis as:

$$|1_N\rangle = \frac{1}{\sqrt{N}} \left(|10\dots0\rangle + |010\dots0\rangle + \dots + |0\dots01\rangle \right) . \qquad (4.3)$$

The W state features N-particle entanglement that is robust against particle loss which makes it interesting for applications in quantum information [115], quantum commu-nication [116] and quantum metrology [106]. W states have been realised in different physical systems such as ions [117], neutral atoms [118], photons [119], and supercon-ducting qubits [26]. They were studied previously with our experimental setup in [44].

The second trajectory (II) starts from a position slightly displaced from the north pole, obtained by rotating the coherent state $|N_N\rangle$ by a small angle ϕ_d around the y-axis. The lower panel of Figure 4.2b shows the Q-distribution along this trajectory for an initial
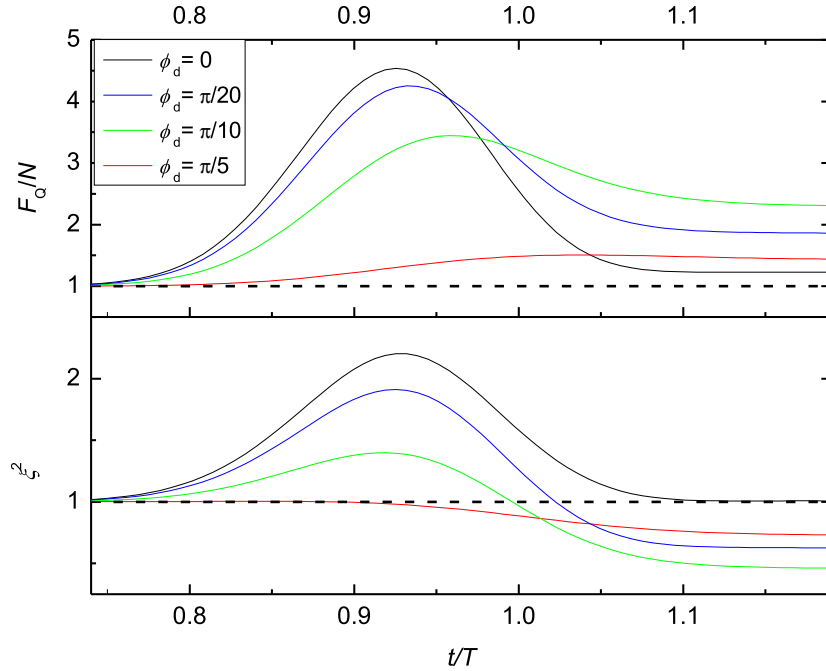
Figure 4.3: Predicted values for Fisher information F_Q and spin squeezing parameter ξ^2 along unitary QZD trajectories with different ϕ_d. Upper panel: $F_Q/N > 1$ (dashed line) indicates particle entanglement. Lower panel: $\xi^2 < 1$ indicates spin squeezing.

rotation of $\phi_d = \pi/10$. As the atomic state passes close to the boundary of the Zeno subspace, its Q-distribution gets distorted into an elongated shape. As the state moves away from the boundary, the distribution keeps the squeezed shape it has acquired.

Can we use this method to shape states that are interesting for quantum technology applications? As detailed in Section 3.3.3, we can answer this question and related ones concerning the entanglement properties of the distorted states by examining their Quantum Fisher information (QFI) F_Q and the spin squeezing parameter ξ^2. Specifically, the criterion $F_Q > N$ indicates particle entanglement (see Equation 3.31) and the criterion $\xi^2 < 1$ indicates spin squeezing (see Equation 3.34). Both cases imply a sensitivity gain for metrological applications. Figure 4.3 shows the calculated values for F_Q and ξ for unitary QZD trajectories passing the boundary of the Zeno subspace in varying distance, given by varying ϕ_d between 0 and $\pi/5$. Looking at the QFI, we find that it reaches its maximum of about $4.5\,N$ for $\phi_d = 0$, at the position of maximum overlap with the W state. Once the atomic states pass and leave the boundary region, the QFI decreases towards a final value (however, F_Q/N stays above unity).

Regarding the spin squeezing parameter ξ, the situation is slightly different. For the Dicke-like states that result for $\phi_d \leq \pi/10$, ξ attains values above unity (as expected, see Section 3.3.3). However, for atomic states that have passed and left the boundary region, ξ^2 gets minimal and attains values below unity, indicating that the squeezed

66

states displayed in the lower right-hand part of Figure 4.2 do feature spin-squeezing. We also see that there is an optimal ϕ_d (in our case around $\pi/10$) that minimises ξ^2 (in our case down to about 0.46).

We conclude that the measurement-induced QZD along trajectory I, in the unitary limit, creates states close to the W state which are highly particle-entangled and offer an advantage in interferometric phase estimation. The deformed states created along trajectory II lead, in principle, to spin squeezing which makes them interesting for quantum metrology applications.

4.1.1   Influence of finite measurement strength

We have already seen in Section 1.3.2 that we cannot perform the experiments with infinitely high measurement rate because increasing the photon flux also increases spontaneous emission which leads to atoms leaving the symmetric subspace. Let us study the difference between Rabi dynamics, unitary QZD and the influence of finite probing strength for the experiment along trajectory I described in Figure 4.2. We compute numerically the populations ρ_{00} and ρ_{11} and the transverse spin length $\frac{2}{N}\sqrt{J_x^2 + J_y^2}$ in the absence of measurement (Equation 1.52 without the Lindblad terms), for unitary QZD according to Equations 4.1, 1.22 and 1.23, and for finite measurement rate (Equations 1.52 and 1.59) $r_m = 23\,\Omega$; the results are shown in Figure 4.4. During ordinary Rabi oscillations, the population ρ_{00} reaches a value of unity at $t = T$, which is also the turning point of the mean spin direction. The maximum population in the state $|1_N\rangle$ is $\rho_{11} \simeq 0.37$ (with ρ_{00} having the same value at this position). In contrast, during unitary QZD, ρ_{00} is completely suppressed, while ρ_{11} reaches a maximum of about 0.93 at $t \simeq 0.93\,T$ which is also the turning point of the mean spin direction. Not surprisingly, the evolution induced by a finite-strength measurement proceeds in between the two limiting cases of Rabi and unitary dynamics. We will see in Section 4.3 that this simple model reproduces well the evolution of the atomic state inside the symmetric subspace $\mathcal{H}_s$ but cannot account for the loss of atoms from $\mathcal{H}_s$.

4.1.2   Effect of spontaneous emission

In order to take into account the effect of spontaneous emission and calculate the expected decay of the population in the symmetric subspace, we consider an anti-Hermitian operator $\bar{H}_{\mathrm{loss}}$ and the modified master equation

$$\frac{d\rho}{dt} = \frac{1}{i\hbar}[\hat{H}_{\mathrm{MW}}, \rho] + \frac{1}{i\hbar}\{\bar{H}_{\mathrm{loss}}, \rho\} + \hat{d}\rho\hat{d}^\dagger - \frac{1}{2}\rho\hat{d}^\dagger\hat{d} - \frac{1}{2}\hat{d}^\dagger\hat{d}\rho\,. \tag{4.4}$$

We suppose that $\bar{H}_{\mathrm{loss}}$ is diagonal in the Dicke state basis with matrix elements given by $\langle n_N|\bar{H}_{\mathrm{loss}}|n_N\rangle = -i\gamma_n$ where $\gamma_n = \gamma\,p_{\mathrm{exc},n}$ and $p_{\mathrm{exc},n}$ is the probability for one atom among the n atoms in $|1\rangle$ to be optically exited. Here, we neglect the probability $(\sim 1/N)$ to fall back into the symmetric subspace after a spontaneous emission.
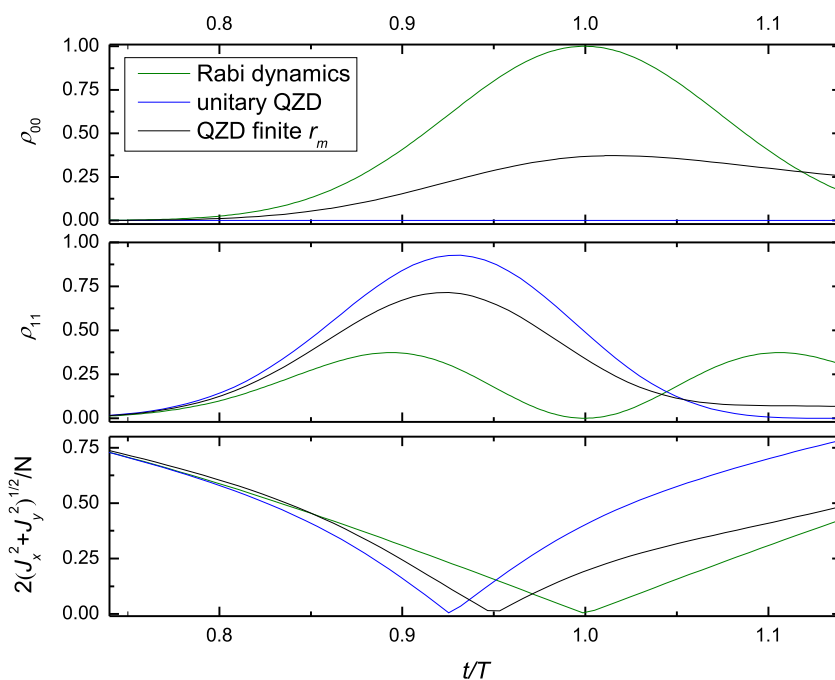
Figure 4.4: Comparison between atomic dynamics in the absence of measurement (standard Rabi oscillations, green), measurement-induced unitary QZD (blue) and QZD with finite measurement rate (black) $r_m = 23\,\Omega$ along trajectory I of Figure 4.2. Upper panel: population ρ_{00}. Centre panel: population ρ_{11}. Lower panel: transverse spin length $\frac{2}{N}\sqrt{J_x^2 + J_y^2}$.
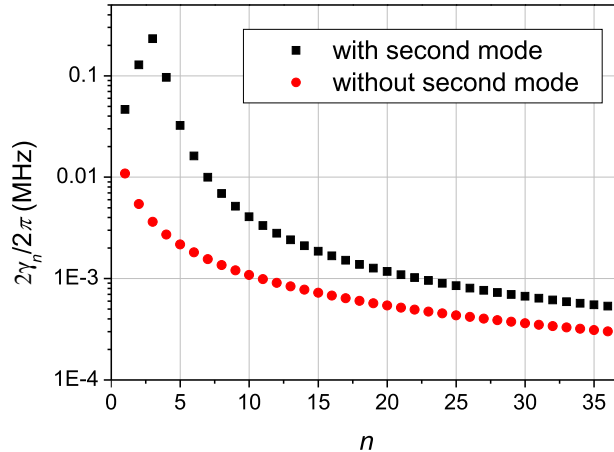
Figure 4.5: Calculated effective loss rates for the Master equation taking into account spontaneous emission. γ_n is the loss rate when the atoms are in state $|n_N\rangle$ at a measurement rate of $r_m = 23\Omega$. Black squares: Simulation including the second cavity mode. Red circles: Values for a single mode cavity calculated from Equation 4.5.

In a single-mode cavity, γ_n is given by Equation 1.51, which reads for $C \gg 1$:

$$\gamma_n = \frac{1}{2Cn}\Phi \approx \frac{r_m}{4nC} \, . \tag{4.5}$$

To include the influence of the second cavity mode, we calculate the probability of excitation $p_{\mathrm{exc},n}$ from the steady-state solution of an independent atom-cavity master equation describing the coupling of n atoms to the TEM_{00} mode taking into account all known experimental parameters for our setup (magnetic field strength and orientation, lattice depth, ...), in particular the presence of the orthogonally polarized TEM_{00} cavity mode. This model is the same used in [120] and is described in detail in [62].

Figure 4.5 shows the calculated rates γ_n as a function of n for a typical measurement rate r_m used in the experiment. We observe that the second polarisation mode leads to a considerably increased loss rate. At $n = 3$, γ_n has a peak with a value increased by more than one order of magnitude which we attribute to a resonance feature of the second cavity mode. Specifically, the second mode can become resonant to the D_2 transition due to the dispersive shift of the light frequency arising from atoms in $F = 1$ in the cavity (see Section 2.8.5).

We use the model described by Equations 4.4 and 4.5 (which has no adjustable parameters) in Section 4.3 to describe our experimental data taking into account the losses from the symmetric subspace.

4.2   Experimental realisation

This section presents the procedure we use to realise the experiments described in the previous section. The experimental sequence can be divided into three parts: initialisation of the atomic state (Section 4.2.1), inducing the desired QZD with a sequence of MW and probing light pulses (Section 4.2.2) and analysing the resulting atomic state by performing quantum state tomography (Section 4.2.3).

4.2.1   State initialisation

We begin the experimental cycle by preparing a sample of several hundreds of ultra-cold atoms according to the procedure detailed in Section 2.8. The atoms magnetically trapped on the atom chip are initially in the $|F = 2, m_F = 2\rangle$ state. We then load them into an intra-cavity dipole trap (trap depth approximately 50 μK) and transfer them into the qubit state $|0\rangle = |F = 1, m_F = 0\rangle$ by means of three consecutive microwave sweeps. Next, we prepare an ensemble of well-defined atom number as described in Section 2.8.5. In brief, atoms in $F = 1$ are not resonant with the light field in the cavity, thereby shifting the cavity resonance. We send probe light into the cavity causing atom losses via light-assisted collisions and simultaneously monitor the rising cavity transmission which allows us to infer the number of atoms left in the cavity. When our target value of 40 atoms is reached, we switch off the probe beam. We terminate the preparation sequence with a weak measurement pulse to check for faulty sample preparation (atoms at $t = 0$ in state $|1\rangle$, occurring in about 25% of all runs).

We have verified the prepared atom number by tomographic measurements and find that we have about 36 atoms in the state $|0\rangle$ (see Section 4.8). The difference to the target value $N_{tot} = 40$ can be explained by the fact that the preparation leads to some atoms changing the Zeeman state. These "spectator" atoms in $|F = 1, m_F \neq 0\rangle$ still shift the cavity resonance but are not addressed by subsequent qubit manipulations. We can estimate the uncertainty this induces on the number of atoms manipulated in the experiment by making the worst-case assumption that the atoms are spread over all three Zeeman states in the $F = 1$ manifold. The probability that in N_{tot} tries, k atoms are in the correct Zeeman state can then be described by a binomial distribution $\mathcal{B}(N_{tot}, k, p) = \binom{N_{tot}}{k} p^k (1-p)^{N_{tot}-k}$ with (from our observation) a success probability $p = \frac{36}{40}$. $\mathcal{B}(N_{tot}, k, p)$ has the standard deviation $\sigma = \sqrt{N_{tot}\, p\,(1-p)}$ which in our case evaluates to $\sigma = 1.9$.

4.2.2   QZD sequence

Once the atoms are prepared in the desired state, we start one of the trajectories I or II described in Figure 4.2 by applying a combination of suitable MW and probe light fields.[1] Initially, all atoms are in $|0\rangle$ so that the total spin points to the south pole of

---

[1]The MW frequency is 6834.75 MHz. This is 60 kHz higher than the unperturbed transition frequency corresponding to the differential light shift between $|0\rangle$ and $|1\rangle$ induced by the dipole trap. The technical
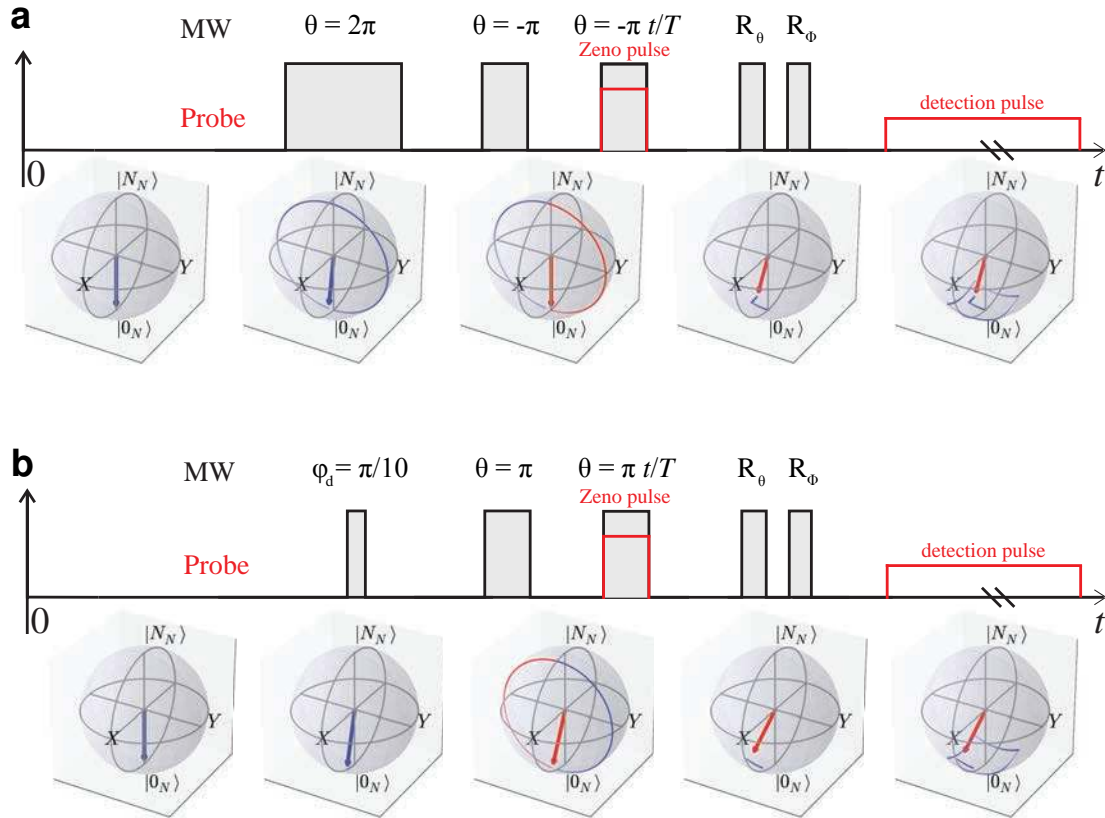
Figure 4.6: Sequence of MW and probe light pulses to realise QZD along trajectory I (a) and trajectory II (b). The upper part of each panel shows the timing sequence of the pulses, the lower part visualises the evolution of the state on the Bloch sphere. Oscilloscope traces showing the precise timing of (a) are depicted in Figure 2.14.

the Bloch sphere. The QZD sequence itself should start with a state fully inside $\mathcal{H}_Z$. The most basic protocol would therefore consist in first applying a π pulse to get from $|0_N\rangle$ to $|1_N\rangle$, and then a pulse corresponding to $\theta = -\pi t/T$ accompanied by cavity measurement to perform the Zeno dynamics. However, it is crucial for the production of the W state to use a trajectory that passes exactly through the south pole. Therefore, to realize trajectory I starting from $|0_N\rangle$, we first perform a $(\theta = -2\pi)$-pulse, then a π pulse immediately followed by the $(\theta = -\pi t/T)$-pulse accompanied by measurement. It has been shown that this pulse sequence compensates for both pulse length and detuning fluctuations [121], ensuring that the trajectory in the absence of measurement passes through the south pole of the Bloch sphere. To perform trajectory II, starting with all atoms in $|0\rangle$, we first apply a small rotation around the y-axis (we choose $\phi_d = \pi/10$ as motivated in Section 4.1) and then a $\theta = \pi$ rotation followed by the $\theta = -\pi t/T$ rotation accompanied by the probing of the cavity. Figure 4.6 shows schematically the timing sequence of MW and probe light fields as well as the evolution of the atomic state on the Bloch sphere for both trajectories.

4.2.3   Tomographic measurement of the Q-distribution

As detailed in Section 3.1.3, we can use our cavity to measure the Husimi Q-distribution. For one complete 2d tomography measurement, we scan the tomography angles θ (around X) and ϕ (around Y) each between $-0.26\pi, ..., 0.26\pi$, resulting in a 7x7 grid of individual measurements at different (θ, ϕ). To perform the required rotation $R(\theta, \phi)$, we apply two consecutive microwave pulses, with adjustable durations ($0.4...1.2\mu$s here) and phases; for technical reasons, there is a delay of 6 μs between successive pulses leading to a total time delay of 14 μs between preparation and tomography.

We then probe the cavity for 120 μs with an intra-cavity flux of $0.9 \cdot 10^6$ photons/s on resonance and measure the photon counts in transmission and reflection with APDs. We assign the result to one of the two outcomes "the atomic ensemble was in the state $|0_N\rangle$" or "at least one atom in the ensemble was in $|1\rangle$". Repeating this measurement several times, we obtain an expectation value for Q which is subject to statistical and systematic errors. The statistical error can be estimated from the standard deviation of a binomial distribution. Repeating each measurement at least 50 times keeps the absolute (relative) statistical error below 0.07 (14%). Each individual measurement is subject to the systematic error ϵ_{01} of assigning the state "at least one atom in $|1\rangle$" when in reality all atoms were in $|0\rangle$ and ϵ_{10} (assigning the state $|0_N\rangle$ when in reality there was an atom in $|1\rangle$). To reduce these errors, we do not just compare the counts to fixed thresholds but, building on methods developed in previous works [62, 45], use the additional information contained in the time evolution of the APD signals[2]. We employ a maximum-likelihood (ML) method to determine for each trace if it is more likely to have been produced by the state $|0_N\rangle$ or the complementary one. In this calculation, we also allow for jumps

---

implementation of the synchronised light and MW pulses is detailed in Section 2.7.2.

[2]For a single atom in the cavity, [62] showed that analysing the whole trace achieves detection errors below 0.01, 20-30% lower than the ones obtained from 2d-thresholding.
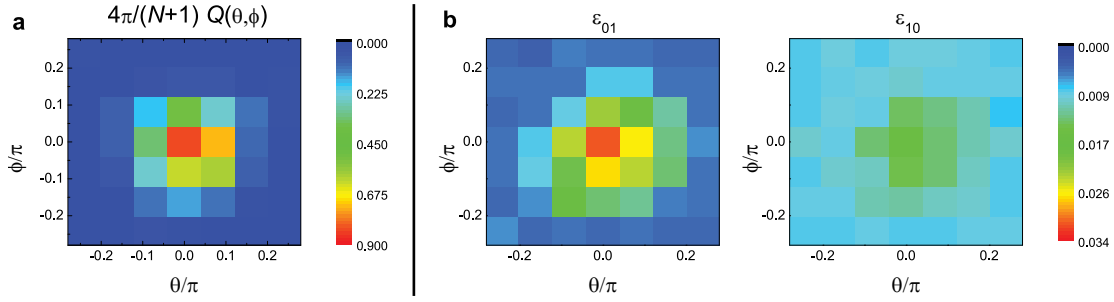
Figure 4.7: 2d tomography of the Husimi distribution $Q(\theta, \phi)$ for a coherent state with $N \simeq 36$ atoms. a) $\frac{4\pi}{N+1} Q(\theta, \phi)$ corresponding to the probability to detect all atoms in $|0\rangle$. b) The error ϵ_{01} of assigning the state "at least one atom in $|1\rangle$" when in reality all atoms were in $|0\rangle$ and the error ϵ_{10} of assigning the state $|0_N\rangle$ when in reality there was an atom in $|1\rangle$. Both errors are higher when there are more atoms in $|0\rangle$ which makes them dependent on the tomography angle (θ, ϕ).

between the two states during the detection time which are characterised by their average "lifetime" τ_0 and τ_1. These depend on the relative populations of atoms in the states $|0\rangle$ and $|1\rangle$ which, in turn, depend on the tomography angles (θ, ϕ). The full parameter set needed for the detection consists of six parameters: τ_0, τ_1, the average count rates in transmission and reflection for $|0_N\rangle$, and the count rates in the complementary state. For each tomographic measurement, we first extract these six parameters from the data. The life-times are obtained from a ML method and the average count rates from histograms of the detection and transmission counts.

We can determine the error of our detection method by creating a large set of artificial APD traces with the given detection parameters and subsequently analysing them with the ML algorithm also used for the experimental data. In all measurements we have performed, the absolute (relative) detection errors are below 0.06 (10%). Figure 4.7 shows the result of a typical tomographic measurement of the Husimi distribution $Q(\theta, \phi)$ of a coherent state together with the detection errors ϵ_{01} and ϵ_{10}.

4.3 Experimental Results

This section presents the results of the different QZD experiments carried out during this thesis. In all experiments, we prepare an ensemble of $N \simeq 36$ atoms, induce QZD for a variable time t and then perform tomographic measurements in two dimensions to record "snapshots" of the $Q-$distribution of the atomic state as it evolves. Specifically, we follow the QZD along the trajectories I and II described above and use the measurements to reconstruct the symmetric part ρ_s of the atomic density matrix. We demonstrate that the time evolution of ρ_s is well described by the models discussed in Section 4.1. Using the criteria presented in Section 3.3, we discuss the entanglement properties of the experimentally created states. Due to experimental imperfections, there is an optimum
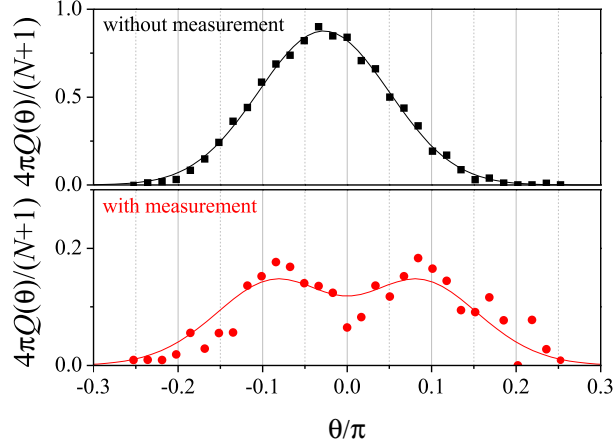
Figure 4.8: Tomography of quantum Zeno dynamics along trajectory I. High-resolution 1d cuts of the Husimi-Q distributions $Q(\theta, \phi = 0)$ for $t = 0.96\,T$ without measurement (upper panel) and with a measurement with rate $r_m \simeq 22\Omega$ (lower panel).

strength for the QZD measurement. We demonstrate the effect of varying measurement strength and discuss the performance expected for a cavity with improved characteristics.

4.3.1 1d tomography close to the W state

To first investigate the QZD in our system, we have performed tomographic measurements along one axis at one specific point along trajectory I that shows high overlap with the state $|1_N\rangle$. Here, the duration of a π-pulse is $T = \pi/\Omega = 4.5\,\mu$s. Figure 4.8 shows $Q(\theta)$ for a fixed evolution time $t = 0.96\,T$, once in the absence of the Zeno measurement, once for a measurement with intra-cavity photon flux $\Phi \simeq 7.6 \cdot 10^6$ photons/s (corresponding to a measurement rate $r_m \simeq 22\Omega$).

As explained in Section 2.7.2, we lock the power for the Zeno light pulse to a reference value corresponding to a certain photon flux Φ_R^{off} measured with the APD in reflection from the off-resonant cavity. We compute the flux entering the cavity according to

$$\Phi = \frac{\Phi_T^{res}}{\eta_F \eta_{APD} \sqrt{T_0}}, \tag{4.6}$$

where we have measured the on-resonant transmitted flux Φ_T^{res} to be $\Phi_T^{res}/\Phi_R^{off} \approx 0.25$ (including the correction factor due to the dead time of the APD). The efficiency of the fibre coupling to the transmission APD has been measured to be $\eta_F = 0.8$, the quantum efficiency of the APD is specified as $\eta_{APD} = 0.55$, and the total cavity transmission has been measured to be $\sqrt{T_0} \simeq 0.34$.

The results demonstrate the difference between the dynamics in absence and presence of the Zeno measurement. Without the measurement, the Q-function displays the characteristic (see Equations 3.5 and 3.6) $\cos(\theta/2)^{2N}$ dependence of a coherent state not quite

centred on the south pole (as expected, since $t < T$). Fitting a function of this form (solid line in the figure) gives the atom number as $N = 36 \pm 2$.

In the presence of measurement, the Q function shows the characteristic distribution which is slightly wider and has a dip around $\theta = 0$. As these data represent only cuts along a line, we cannot sensibly reconstruct the full density matrix of the atomic state including coherences [44]. We can, however, attempt the reconstruction of a diagonal density matrix, effectively assuming that the distribution $Q(\theta, \phi)$ is rotationally symmetric. With this assumption, the reconstruction of the data in the lower panel gives the populations $\rho_{00} = 0.12$, $\rho_{11} = 0.25$, $\rho_{22} = 0.00$, $\rho_{33} = 0.03$ with $\mathrm{Tr}\rho_s = 0.40$. The Q-function corresponding to this diagonal density matrix is shown as solid line. We see that the reconstructed Q-distribution reproduces the dip, but does not fit the experimental data very well (it is lower than the maxima of the data and higher than the minimum). This can be explained by the fact that the reconstructed $Q(\theta)$ is by assumption completely symmetric about $\theta = 0$. However, we do not expect the experimentally created state to be symmetric (see Figure 4.2b) and indeed the data shown in Figure 4.8 are not. To adequately reconstruct states with asymmetric Q-function, we have therefore performed 2d tomographic measurements.

4.3.2 Time evolution in 2d tomography

We have experimentally recorded the time evolution of the atomic state under QZD close to the boundary of the Zeno subspace, similar to the simulation in Figure 4.2. As $Q(\theta, \phi)$ is strongly radially asymmetric during this evolution, single 1d cuts are in this case not adequate to fully reconstruct the atomic state. We therefore perform 2d tomography, measuring $Q(\theta, \phi)$ on a 7x7 grid spanning an angular sector of $0.52\pi \times, 0.52\pi$ around the south pole of the Bloch sphere. For this measurement, $N = 36 \pm 2$, $\Omega = 4.65(6)\,\mu$s and $r_m \simeq 23\Omega$.

The results are shown in Figure 4.9, presenting the raw data and the Q-distribution of the reconstructed density matrices along trajectories I and II. As the state approaches the boundary of $\mathcal{H}_Z$, its Q-function is deformed such that $Q(0,0)$, which is proportional to the population in $|0_N\rangle$, remains small at all times. On trajectory I, at $t/T = 0.96$, a ring-shaped distribution appears, indicating high overlap with the W state. Driving the dynamics further, the state recovers its Gaussian character as it leaves the measurement boundary. On trajectory II, we observe clearly the expected deformation of $Q(\theta, \phi)$ as the atomic state passes along and leaves the boundary of $\mathcal{H}_Z$.

When reconstructing the symmetric part of the density matrix ρ_s, we limit the basis to a certain number of Dicke states. Including too few basis states prevents the reconstruction from correctly reproducing the experimental data, while including too many states increases the noise without giving additional information.[3] As can be seen in Table 4.1, when including the Dicke states from $|0_N\rangle$ up to $|n_N\rangle$, the reconstructed populations

---

[3] As the reconstructed density matrix is Hermitian, reconstruction with n basis states corresponds to a parameter space of n^2.
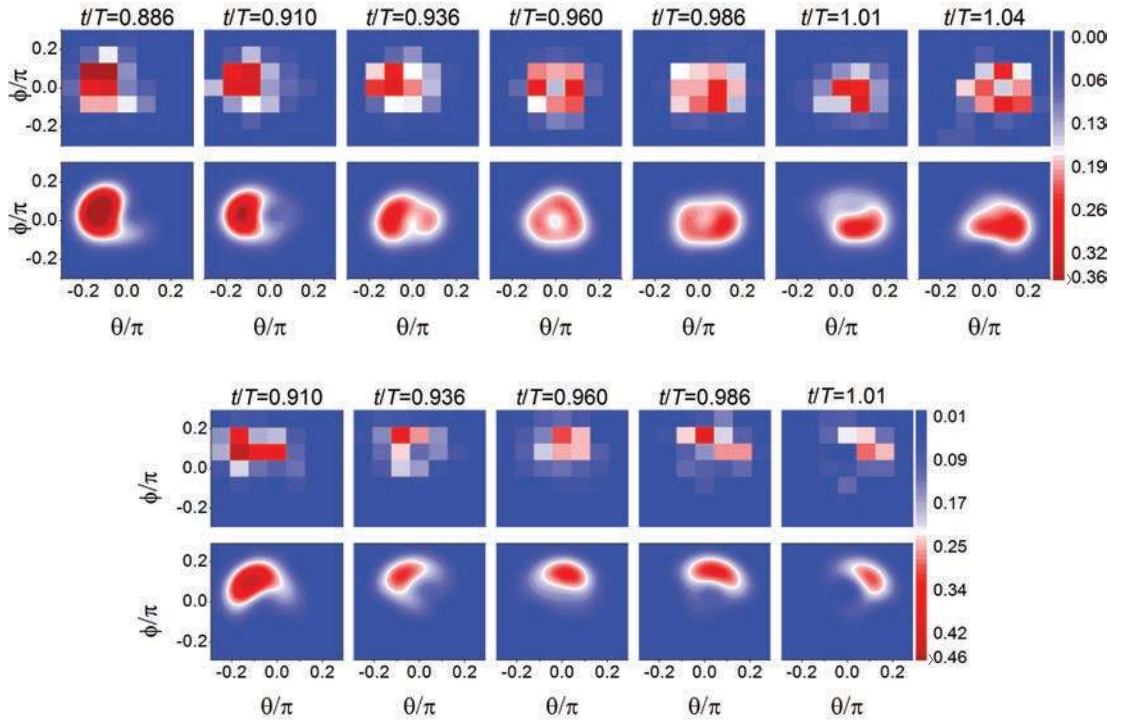
Figure 4.9: Measured 2d distributions $\frac{4\pi}{N+1}Q(\theta, \phi)$ at different times t along trajectory I (upper panel) and trajectory II (lower panel) in the presence of measurement. The 7×7 measurement grid is centred around the south pole. In each panel, the upper row shows raw data, the lower row the Q-distribution corresponding to the reconstructed density matrices.

a)	ρ_{00}	ρ_{11}	ρ_{22}	ρ_{33}	ρ_{44}	ρ_{55}	ρ_{66}	$\mathrm{Tr}(\rho_s)$
$n=2$	0.16	0.38	0.01					0.55
$n=3$	0.17	0.36	0.01	0.01				0.55
$n=4$	0.17	0.36	0.01	0.00	0.01			0.55
$n=5$	0.17	0.36	0.01	0.00	0.00	0.00		0.55
$n=6$	0.17	0.36	0.01	0.00	0.00	0.00	0.00	0.55
b)	ρ_{00}	ρ_{11}	ρ_{22}	ρ_{33}	ρ_{44}	ρ_{55}	ρ_{66}	$\mathrm{Tr}(\rho_s)$
$n=2$	0.03	0.13	0.22					0.38
$n=3$	0.03	0.08	0.15	0.15				0.40
$n=4$	0.02	0.07	0.11	0.12	0.08			0.41
$n=5$	0.03	0.05	0.12	0.13	0.07	0.01		0.40
$n=6$	0.02	0.07	0.12	0.11	0.07	0.01	0.01	0.41

Table 4.1: Reconstructed populations ρ_{ii} of the atomic system for different basis truncations. The basis includes the Dicke states from $|0_N\rangle$ up to $|n_N\rangle$. (a) Reconstructed populations for the state in Figure 4.9 obtained after a QZD of $t/T = 0.96$. (b) The same reconstruction but for the state displayed in the rightmost frame of Figure 4.9.

do not change for $n \geq 4$ and we therefore truncate the basis at $n = 4$ for all presented measurements. To estimate the statistical error on the reconstructed density matrix, we use a bootstrapping method. We generate sets of artificial measurements each having the same number of samples and the same average $P_0(\theta, \phi)$ as the experimental data. For each 2d tomography measurement, we then operate the reconstruction algorithm on 1000 artificial datasets to obtain the standard deviations for the populations of the reconstructed density matrix.

4.3.3 Time evolution of the density matrix

The cavity measurement is characterized by an effective rate which is not infinitely high, and is accompanied by spontaneous emission, which tends to populate undesired states outside the symmetric subspace. Figure 4.10a shows the decay of the symmetric subspace population $\mathrm{Tr}(\rho_s)$ for trajectory I obtained from the reconstructed density matrices. In order to capture the essential features of the QZD - which takes place in the symmetric subspace - we plot the measured relative populations $\rho'_{ii} = \rho_{ii}/\mathrm{Tr}(\rho_s)$. We observe that ρ'_{00}, which would reach unity in the absence of measurement (dotted lines), is strongly reduced by the measurement (Figure 4.10b), while ρ'_{11} is increased (Figure 4.10c). We also observe that the turning point of the Rabi oscillation of the collective spin shifts to shorter times (Figure 4.10d), which is expected because the measurement reduces the dimension of the Hilbert space. The deviation from the ideal QZD (dot-dashed lines) is well described by the simple model given by Equations 1.52 and 1.59 with $r_m = 23\Omega$.

The model given by Equation 4.4 including spontaneous emission (solid lines in Figure 4.10) gives very similar predictions for ρ'_{ii} and additionally explains the measured

decay of $\text{Tr}(\rho_s)$, with no adjustable parameters. We note that $\text{Tr}(\rho_s)$ decays below 60% as the state approaches the south pole of the Bloch sphere. This loss, due to spontaneous emission predominantly from the second polarisation mode in the cavity, considerably limits the maximum population ρ_{11} we attain.

The full result of the reconstruction is shown in Figure 4.11 including the unnormalised populations ρ_{ii} for $i < 5$ together with the full master equation model. We observe that the model describes the data well.

4.3.4 Entanglement and quantum Fisher information

To quantify the entanglement of the state at $t/T = 0.96$, we employ the entanglement criterion described in Section 3.3.4. Based on the populations ρ_{00} and ρ_{11} extracted from the reconstruction presented in the previous section, we can derive a lower bound on the depth of entanglement of the multiparticle state. As shown in Figure 4.12, the experimentally created state lies above the bound for a k-producible state with $k = 7$. Including the uncertainty in the total atom number and the reconstructed populations, we find an entanglement depth of 8^{+3}_{-5}atoms.

To assess whether the states created by the QZD are interesting for quantum metrology applications, we compute a lower bound on their quantum Fisher information (QFI) F_Q, as detailed in Section 3.3.2. The result is shown in Figure 4.13. Taking into account the uncertainty on F_Q and on the total atom number N, the first three data points on trajectory II have $F_Q/N > 1$, which shows that they are (at least 2-) particle entangled and feature (marginal) metrological gain with respect to classical states.

We have also computed the spin squeezing parameter ξ^2, it is larger than unity for all presented measurements. This is, in accordance with the predictions of the full Master equation model, due to the high losses from the symmetric subspace and the resulting shortening of the mean spin length.

4.3.5 Postselecting on cavity transmission

By detecting transmitted photons on the APD behind the cavity, we can access the result of the Zeno measurement, i.e., obtain information about whether the dynamics was indeed restricted to $\mathcal{H}_Z$. Figure 4.14 shows the fraction of runs where we observe a transmitted photon during the Zeno measurement pulse together with an estimate obtained from the full Master equation model. As an effect of the finite measurement strength, these runs have the atomic state leaking through the boundary of $\mathcal{H}_Z$ and populating the state $|0_N\rangle$ in which the cavity transmits. We see that the probability to observe a transmitted photon increases with the duration of the Zeno pulse which is in line with the observed increase of ρ_{00} (cf. Figure 4.11). We see that the experimental observation agrees roughly with a prediction that consists in integrating the theoretically expected population ρ_{00} that builds up during the Zeno pulse and multiplying it by the expected transmission for the state $|0_N\rangle$. This calculation neglects the contribution of
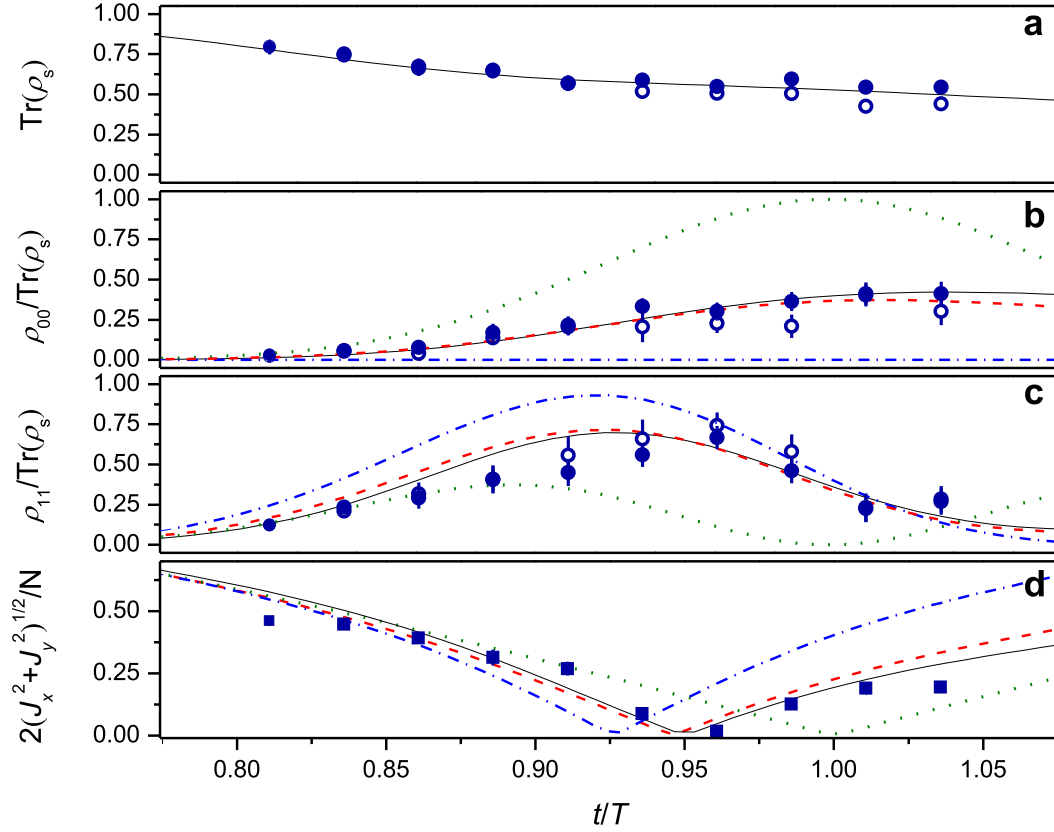
Figure 4.10: Evolution of the atomic population during QZD along trajectory I. (a) Population in the symmetric subspace. (b),(c): relative populations $\rho'_{ii} = \rho_{ii}/\text{Tr}(\rho_s)$. (d): Transverse spin length $\frac{2}{N}\sqrt{J_x^2 + J_y^2}$. Green dotted lines in (b)-(d) show the expected evolution without measurement (Rabi oscillation). The measured data is well described by the full model with no adjustable parameters (black solid lines). The dynamics within the symmetric subspace can also be understood when neglecting spontaneous emission (red dashed lines). Blue dot-dashed lines are predictions for ideal QZD ($r_m \to \infty$). Open symbols: measured evolution excluding runs with nonzero cavity transmission during the QZD. Error bars are 1σ statistical errors of the reconstruction.
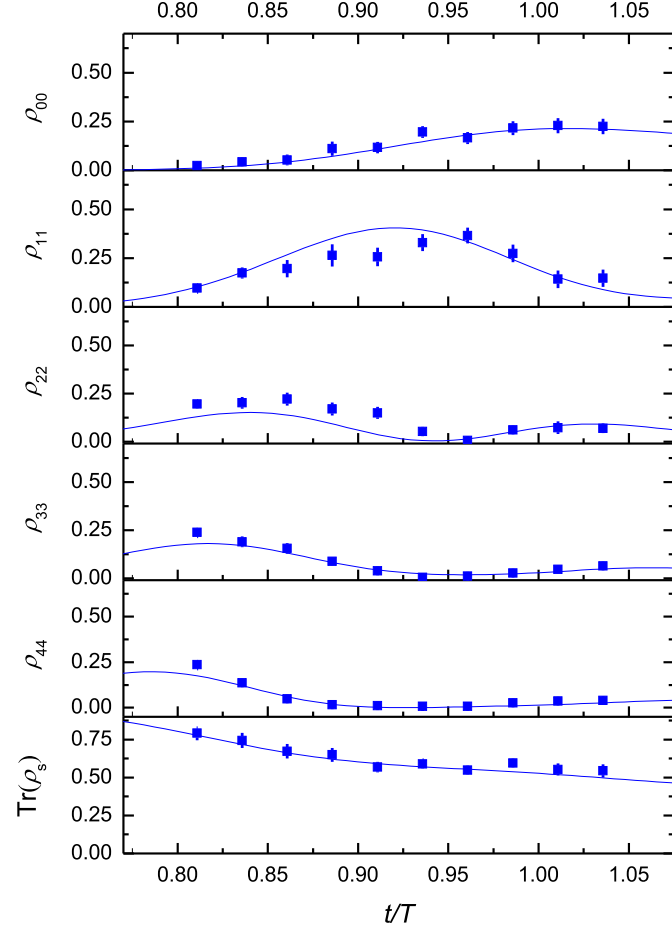
Figure 4.11: Evolution of the populations during QZD along trajectory I. The data points are the populations ρ_{ii}, with $i < 5$, reconstructed from the tomography measurement shown in the upper panel of Fig.4.9. The lowest curve shows the total population in the symmetric subspace. The solid lines are the prediction of Eq. 4.4.
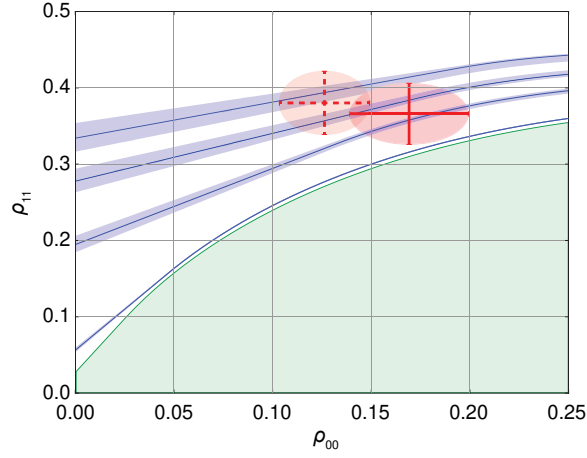
Figure 4.12: Multiparticle entanglement criterion for the reconstructed atomic state at $t/T = 0.96$ along trajectory I. From bottom to top, the blue curves show the bound $C(N, k, \rho_{00})$ for a k-producible state of $N = 36$ atoms for $k = 2, 7, 10, 12$. The blue shaded areas limit the bounds for varying the atom number from 34 to 38 which corresponds to 1σ of the atom number distribution. The red ellipses indicates the uncertainty on the reconstructed populations ρ_{ii}, dashed red lines: postselecting on zero cavity transmission. The green curve is the bound for $k = 1$, states outside the green area are entangled.
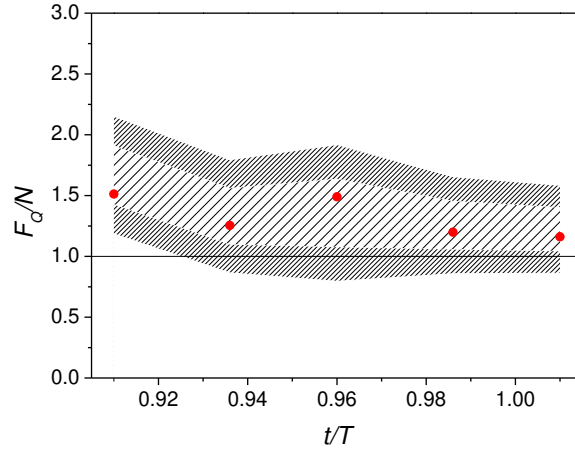

Figure 4.13: Lower bound for the quantum Fisher information F_Q for the data shown in the lower panel of Figure 4.9. The hatched areas are confidence intervals corresponding to 68% and 95% probabilities, respectively.
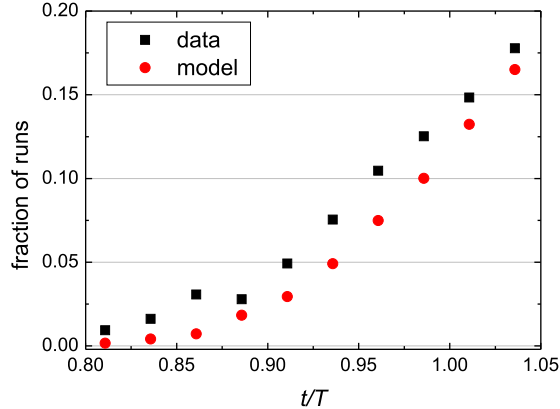
Figure 4.14: Fraction of runs where an transmitted photon is observed during the QZD along trajectory I. Black squares: experimental data. Red circles: prediction from the full Master equation model.

other Dicke states which explains why the calculated values are systematically lower than the experimental data.

At the price of excluding the data where a transmitted photon was observed, we can improve the fidelity of the produced state. Excluding these runs from the analysis indeed improves the quality of resulting state, as shown by the open symbols in Figure 4.10. As an example, for $t = 0.96\,T$ along trajectory I, we obtain an entanglement depth of 11^{+2}_{-3} atoms.

4.3.6 Large scale time evolution in 1d tomography

We have also studied the QZD on a larger time scale, by performing 1d tomographic cuts for varying evolution time $t/T = 0, 0.5, 0.96, 1.5, 2$. Figure 4.15 shows the resulting $Q(\theta)$ for a tomography range $\theta = -0.26\pi, ..., 0.26\pi$. As an upper bound for Q, the figure includes the symmetric subspace population $\mathrm{Tr}(\rho_s)$ obtained from the full Master equation simulation.

As expected, we observe that for $t < T$, far away from the boundary of $\mathcal{H}_Z$, the Q-function follows the symmetric shape for a coherent spin state. Additionally, we see that for $t > T$, we recover a Gaussian-like shape. However, the height of Q gets strongly reduced by the decay into the non-symmetric subspace caused by the second cavity mode. We observe that this decay increases sharply at $t/T \simeq 0.8$. This can be explained by the strong increase in spontaneous emission caused by a resonance with the second cavity mode (cf. Section 4.1.1) occurring when there are about 3 atoms in $|1\rangle$.
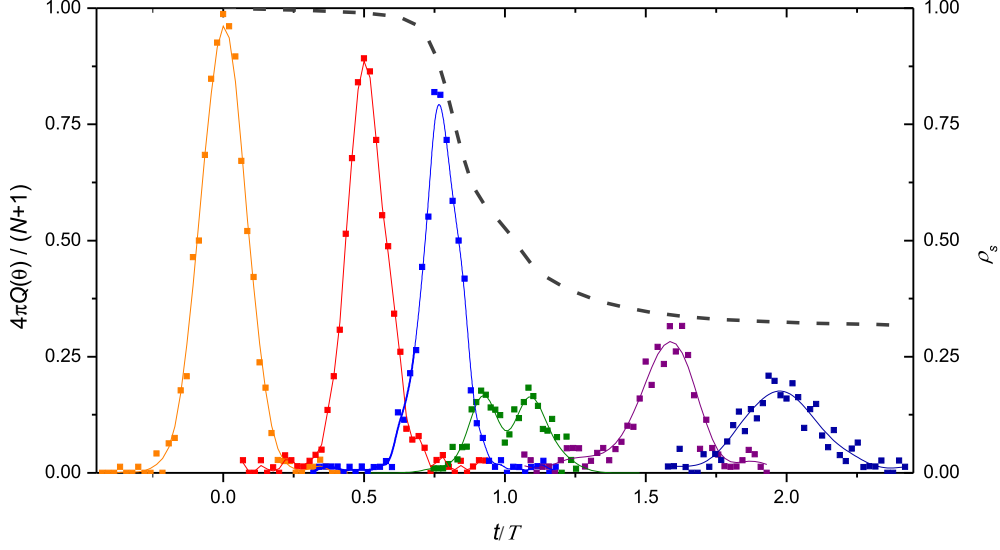
Figure 4.15: QZD along trajectory I. The plot shows the distribution $Q(\theta)$ for different times t/T corresponding roughly to rotations of $0, \frac{1}{2}\pi, \frac{3}{4}\pi, \pi, \frac{3}{2}\pi, 2\pi$ during the QZD. The solid lines are guides to the eye. The dashed line represents the symmetric subspace population ρ_s obtained from the full Master equation model.

4.3.7 Influence of measurement rate

For a given cavity, a higher photon flux Φ increases the measurement rate and thus reduces the contamination of the state by $|0_N\rangle$. However, it also increases the spontaneous emission rate and thus the probability to leave the symmetric subspace. Considering both effects, there exists an optimum measurement strength maximising the entangled states' purity.

We have investigated this behaviour experimentally by varying the measurement strength for a fixed time t along trajectory I, the results are shown in Figure 4.16. The off-resonant count rates in reflection are locked to $(0, 1.5, 2.5, 3.5, 4.5, 5.5, 6.5)$ M cts/s, respectively, which, corrected for the APD dead time, corresponds to transmitted photon fluxes $\Phi_T^{res} \approx (0, 0.4, 0.6, 0.9, 1.1, 1.4, 1.6)\ 10^6\ \text{s}^{-1}$ and intra-cavity photon fluxes $\Phi \approx (0, 2.4, 4.0, 5.7, 7.6, 9.3, 10.8)\ 10^6\ \text{s}^{-1}$. Increasing the measurement rate from zero, ρ_{00} decreases while ρ_{11} increases as normal dynamics turns into QZD. At the same time, spontaneous emission increases, reducing the population in the symmetric subspace. The optimum measurement rate is a compromise between these conflicting effects.

By solving the full Master equation model, we obtain the solid curves in Figure 4.16, which are in good agreement with the experimental data, and which show a broad maximum of ρ_{11} as a function of r_m. The data presented in section 4.3.2 is taken at $r_m \approx 23\Omega$, which maximizes the number of entangled particles as deduced in Section 4.3.4.
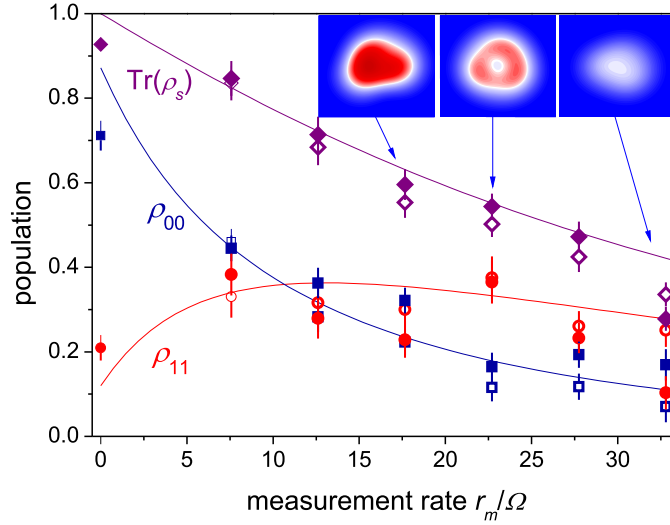
Figure 4.16: QZD along trajectory I for different measurement strengths. Tomography measurements are taken after a fixed evolution time $t = 0.96\,T$ for different measurement rates r_m. Filled symbols: reconstructed populations ρ_{00} (blue) and ρ_{11} (red), and population in the symmetric subspace (purple). Solid lines: results of the full model. The insets show some of the reconstructed Q distributions. Open symbols: runs with non-zero cavity transmission excluded.

4.3.8   Dependence on cavity parameters

As we have seen in the previous sections, the present experiments are strongly limited by the spontaneous emission caused by the second cavity mode arising from imperfections of the cavity mirrors. As shown in Chapter 5, it is possible to fabricate fibre cavities with mode splitting reduced to zero. Additionally, current state-of-the-art dielectric mirror coatings allow to produce fibre cavities with a finesse approaching 200000 [122, 123, 124], compared to 37000 in our cavity). We have simulated the QZD experiment along trajectory I for cavities with such improved characteristics by numerically solving the Master equation 4.4 with accordingly adjusted scattering rate γ_n and cooperativity C. Figure 4.17 shows the results for the following three models: a) the current experimental situation, i.e. a cavity with $C = 110$ and a second mode detuned by 540 MHz, b) single polarisation mode cavity with the same C and the loss rate γ_n given by Equation 4.5) and c) single-mode cavity with $C = 570$ and the corresponding γ_n as could be achieved with a state-of-the-art mirror coating. We perform the simulations for varying probing strength r_m to find the highest value ρ_{11}^m attained during QZD along trajectory I along with the corresponding values ρ_{00}^m and $\text{tr}(\rho_s^m)$.

For the current cavity, we observe the fast decay of ρ_s due to the second polarisation mode. The decay limits the maximum fidelity of $\rho_{11}^m \lesssim 0.5$ at a measurement strength which is comparatively low so that there is a large population of $\rho_{00}^m \approx 0.25$. In the
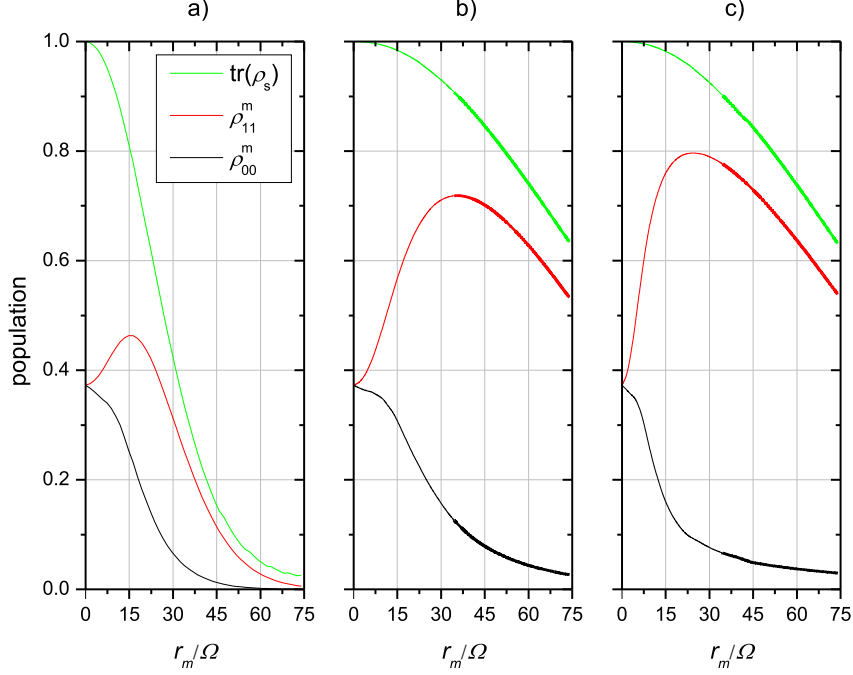
Figure 4.17: Theoretical expectations for performing the QZD experiment along traject-ory I with different cavity parameters for $N = 36$ atoms. In dependence on the cavity probing rate r_m, the plots show the maximum population ρ_{11}^m attained during the QZD together with the corresponding population ρ_{00}^m and the symmetric subspace popula-tion $\mathrm{tr}(\rho_s^m)$ for the following models: a) Current experimental situation, cooperativity $C = 110$ with second polarisation mode. b) $C = 110$, no second mode. c) $C = 570$, no second mode.

present case, we can improve the ratio ρ_{11}/ρ_{00} by slightly increasing r_m (as we have also seen experimentally, see the previous section).

A cavity of same cooperativity but without second mode would be, according to the simulations, a definite improvement due to the eliminated scattering. This would make it possible to increase r_m to obtain a maximum $\rho_{11}^m \approx 0.7$ while at the same time reducing the contamination $\rho_{00}^m \approx 0.1$ before being limited by scattering.

A single-mode cavity with improved finesse is expected to give a further improvement. The simulations show that the scattering would be essentially be the same, but the reduced cavity losses would allow to decrease r_m and produce a W state with maximal fidelity $\rho_{11}^m \approx 0.8$ with a contamination of $\rho_{00} \leq 0.1$. Applying the entanglement criterion for states close to the W state, this would correspond to an entanglement depth of at least 27 out of 36 atoms.

85

4.4 Conclusion

In this chapter, we have presented our experimental realisation of QZD in an ensemble of about 36 ^{87}Rb atoms. Through tomographic measurements of the ensemble's Q function we have given a time-resolved account of how this deterministic scheme creates multiparticle entanglement. Specifically, we have created states with depth of entanglement of at least 3-11 atoms and fidelity of up to 0.37 with respect to a W state of 36 atoms. We have also shown that the QZD can be used as a tool to create non-classical states that provide an advantage in quantum metrology applications. We have discussed the limitations arising from the experimental imperfections of finite probing strength and scattering due to spontaneous emission and have identified the presence of a second polarisation mode caused by imperfections of the cavity mirrors as the limiting factor in the current experimental setup.

Chapter 5

Splitting of polarisation modes in fibre Fabry-Perot cavities

In the previous chapter, we have seen that our QZD experiments have been mainly limited by the influence of a second polarisation eigenmode of the fibre cavity. This polarisation-dependent frequency splitting of the fundamental transverse mode is a typical phenomenon of high finesse resonators and a general inconvenience for cQED experiments. At the beginning of this thesis, the origin of this phenomenon was still unclear. This chapter presents our work investigating the causes of the frequency splitting, specifically in FFP cavities, and ways to control it.

Section 5.1 briefly motivates in how far controlling the polarisation mode splitting is an advantage for cQED experiments. The origin of the splitting in FFP cavities lies in imperfections in the CO_2 laser fabrication of the fibres which we describe in Section 5.2. Section 5.3 presents the theoretical description of how the splitting is produced by slight asymmetry in the microfabricated fibres and how it can be controlled. We have experimentally confirmed the theoretical predictions and show that the splitting can be controlled in practice as demonstrated in Section 5.4. These insights have led to preliminary work sketched in Section 5.5, both towards new experimental setups and to advancing the fibre fabrication process.

We note that similar work has been done independently in the group of G. Rempe [124].

5.1 Introduction

In our experimental setup, both FFP resonators exhibit a frequency splitting between two polarisation modes of the TEM_{00} transversal mode. The modes are linearly orthogonally polarised and separated by about 540 MHz (FFP1) and 730 MHz (FFP2) which in both cases corresponds to about 5 resonator linewidths (FWHM) (compare Section 2.3.1). This feature was noted at the time of construction and explained as arising from birefringence in the dielectric mirror coatings applied to the fibres [63, 46] which can also be observed in macroscopic FP cavities [125, 126].

In the QZD experiments presented in the previous chapter of this thesis, we have coupled one polarisation eigenmode of the cavity to an atomic resonance so that the second mode is detuned. During the experimental sequence, however, this second mode can become

resonant, leading to strongly increased incoherent scattering (see Section 4.1.1). We have seen in Section 4.3.8, that this scattering induced by the second polarisation mode is the main limit to the high-fidelity preparation of entangled states via QZD. Previous experiments with our setup have been similarly limited by the effect of the second mode [120]. For cQED experiments with atoms, the splitting is also a disadvantage as it prevents to couple circularly polarised light into the cavity to drive exclusively σ^+ or σ^- transitions between Zeeman states.[1] If the splitting can be controlled, it is therefore desirable to make it as large as possible (so that one mode is always far detuned) or to minimise it (to realise a cavity with degenerate polarisation modes).

We started our investigation of the frequency splitting with the hypothesis that it was due to birefringence in the highly reflective mirror coatings. This phenomenon is well known in high finesse resonators made from macroscopic dielectric mirrors, for example for gravitational wave detection (see [126]). The most frequent cause for the birefringence in macroscopic mirrors are mechanical stresses arising from mounting the mirrors [127]. Examining experimentally fibre cavities put under mechanical stress, we did not observe a notable effect and concluded that the birefringence was related to asymmetries of the microfabricated mirror structures. It is therefore relevant to examine the fibre fabrication process.

5.2 Fibre production and characterisation

The production of optical fibres suitable for building FFP cavities consists of three main steps. First, the glass fibre is prepared and cleaved to produce a smooth, regular end facet. The facet is then microfabricated with a CO_2 laser to create the concave geometry desired to make a stable resonator. Finally, a highly reflective dielectric coating is applied to the fibre tip. We do the preparation and fabrication ourselves and send the fibres to an external company that for dielectric coating with an ion beam sputtering process.

The CO_2 laser setup used to micro-fabricate the fibres in the current FFP experiment was build up in [128] and is shown schematically in Figure 5.1. The prepared fibre is placed on a three axis stage and brought into the focus of a CO_2 laser beam with a wavelength of 10.6 μm. An adjustable telescope before the focussing lens is used to change the laser beam's waist size. A dichroic mirror after the focussing lens is used to image the fibre tip with the help of an optical microscope which is indispensable to correctly position the fibre in the laser beam.

The fibres are fabricated with pulses of laser light, relying on the fact that silica shows high absorption at the utilised far-infrared wavelength. The process parameters are spot size (typically several tens of μm), power (several hundred mW) and duration (several tens of ms) of the CO_2 laser light. The fabrication takes place in a specific parameter regime in which the energy deposited by the laser beam not only melts the

---

[1]With the splitting, light polarised linearly along one polarisation eigenmode can be used to drive both σ transitions equally. Purely σ^+ or σ^- polarised light can only be produced from a beam off the cavity axis.
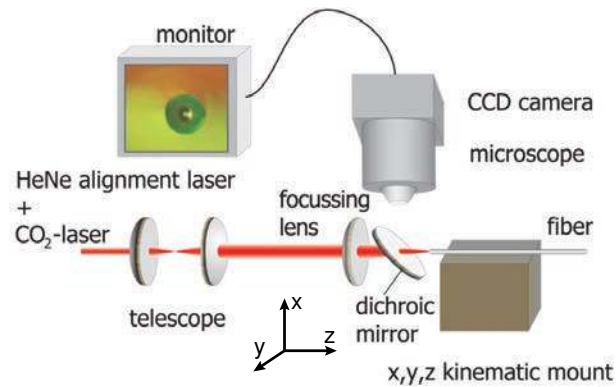
Figure 5.1: Schematic of the CO_2 laser setup used to micro-fabricate the fibres for the FFP experiment. Adapted from [63].

silica (which, alone, would lead to a convex shape determined by surface tension) but also removes material through evaporation to create the desired concave structure. An important advantage of this process is the low roughness of the created surface (atomic force microscope measurements give a RMS surface roughness of $\sigma = 0.2(1)\,\mathrm{nm}$) which limits the scattering losses when using the surface as mirror of an optical resonator [129]. Additionally, this technique makes it possible to create concave structures with radii of curvature down to 30 μm and less [122, 129] which is interesting for cQED applications in which it is advantageous to have short resonators with small mode volume (cf. Section 2.3.1).

Figure 5.2 shows the analysis of a typical microfabricated fibre with a commercial optical profilometer. Figure 5.2a shows a full surface profile with the concave depression in the centre of the fibre facet clearly visible. In a FFP resonator with small mode volume, the size of the cavity mode on the mirrors is small (in our experiment the diameter is less than 9 μm) so that the central part of the profile is of special relevance. Figure 5.2b displays a 1d cut through the fibre centre. We observe that the central part of the profile is in good approximation spherical. We also see that the local radius of curvature R (defined in Figure 5.2c) of the profile is minimal at the centre and then increases towards the edges.

Imperfections

As detailed in the next section, the symmetry of the microfabricated surface is of special importance for the performance in a high-finesse fibre cavity. Achieving precise control of the structure requires first that the fibres are well prepared. A badly cleaved fibre might have a facet of uneven surface or one that is not perpendicular to the fibre axis, both of which will cause asymmetries during the laser machining. During the production of the fibres used in the present experiments, the surfaces of the facets were inspected with an optical microscope to verify that they were even and free of dust. A clean facet
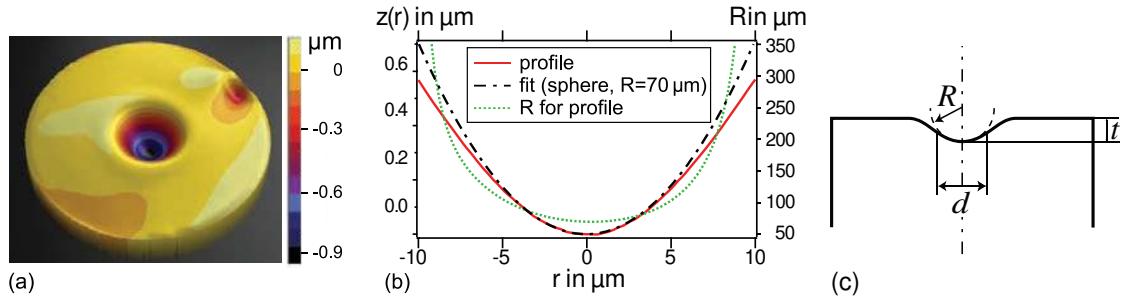
Figure 5.2: Analysis of microfabricated concave structures on an optical fibre. (a): 3d plot of the surface profile measured with an optical profilometer. (c): Cut through the centre of the profile shown in (a). (c): Parameters used to characterise the profile. Our discussion concentrates on the radius of curvature (ROC) R. Adapted from [129].
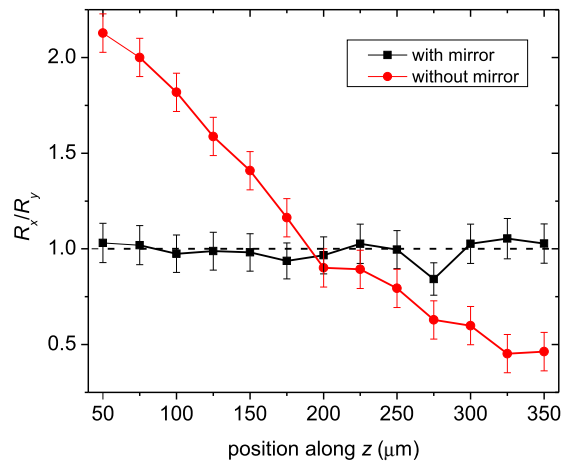

Figure 5.3: Ratio of horizontal to vertical radius of curvature R_x/R_y of CO_2 laser-machined structures (waist size about 32 μm). The dichroic mirror used for alignment produces astigmatism so that the symmetry of the structures varies with the position on the beam axis z.

90

surface typically indicates a successful cleave which also means that the angle between cleave surface and fibre axis is 90° to within less than 1°. The asymmetry introduced by this possible deviation is of minor importance in the old fabrication setup.

One important source of asymmetries in the described setup is the dichroic mirror inserted at an angle of 45° to the axis of the fabrication laser beam. After passing the mirror, the beam is astigmatic so that (cf. Figure 5.1) the waist in x-direction is at a different position along the z-axis than the waist in y-direction. We have verified this issue experimentally by machining a silica test slide placed at varying position along z while keeping all other parameters constant. We have estimated the radii of curvature (ROC) R_x, R_y in x- and y-direction from optical microscope images of the resulting concave structures. Figure 5.3 shows the ratio R_x/R_y of the structures produced with and without the dichroic mirror in the beam path. Without the dichroic mirror, the structures are symmetric ($R_x/R_y = 1$ within the measurement precision) everywhere along z. With the dichroic mirror, the symmetry of the machined structures depends strongly on the position along z, limiting the creation of symmetric structures to a specific position on the z-axis. The positioning precision is limited by the depth of field of the microscope, from the data in Figure 5.3 we expect this to translate into variations of up to 5% on R_x/R_y.

Other important sources of asymmetries are fluctuations in the CO_2 laser intensity and bad alignment of the fibre axis with the laser beam axis. Characterising the asymmetric structures by their radii of curvature along two orthogonal axes, we have observed the ratio of the larger to the smaller ROC R_1/R_2 to vary overall between 1.01 and up to 1.20 for fibres that were produced with the old setup and deemed good enough to be sent for coating.

5.3 Theoretical description

This section presents the theoretical description of how asymmetry in the mirror geometry results in a frequency splitting of polarisation modes in a cavity. We start with a general description of the behaviour of a cavity made from birefringent mirrors. We then present how an effective birefringence arises as a purely geometric effect when treating the reflection of a Gaussian mode from an asymmetric mirror beyond the paraxial approximation.

5.3.1 Jones calculus for a cavity made of birefringent mirrors

Let us consider a resonator made from two birefringent mirrors as shown schematically in Figure 5.4. We can describe each mirror M_1, M_2 as a waveplate with two orthogonal axes so that light polarised along the slow axis is retarded by the phase ϕ_1, ϕ_2 with respect to the fast axis. Both mirrors are facing each other so that their surfaces are parallel and their fast axes form the angle ϑ. We now want to determine the polarisation eigenmodes supported by this cavity and their dependence on $\phi_1, \phi_2, \vartheta$. This problem is
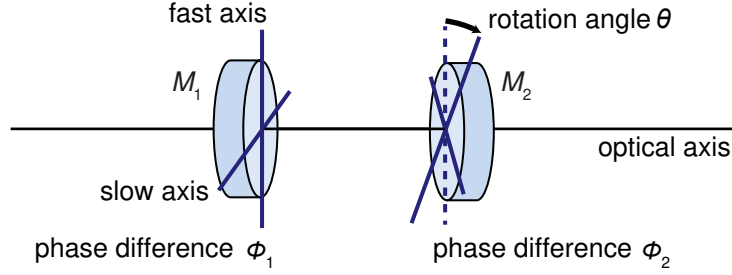
Figure 5.4: Schematic of a resonator made from two birefringent mirrors.

easily treated using Jones calculus for polarised light and is discussed in [130, 131]. The mirrors $M_j, j = 1, 2$ can be described as phase retarders with Jones matrices:

$$\underline{M}_j(\phi_j) = \begin{pmatrix} 1 & 0 \\ 0 & e^{i\phi_j} \end{pmatrix}, \tag{5.1}$$

so that the total system is described by the matrix:

$$\underline{M}_{tot} = \underline{R}^{-1}(-2\vartheta_2)\underline{M}_2(\phi_2)\underline{R}(2\vartheta_2)\underline{M}_1(\phi_1), \tag{5.2}$$

where $\underline{R}(\vartheta)$ is a rotation matrix. In our case, the phase shifts are on the order of hundreds of μrad. By calculating the eigenvectors and eigenvalues of $\underline{M}_{tot}$ (see Appendix D) with the approximation $\phi_1, \phi_2 \ll 1$, we find that the cavity supports two orthogonal modes of approximately linear polarisation. After one round-trip in the birefringent resonator, the two modes differ by the round-trip phase shift δ

$$\delta(\phi_1, \phi_2; \vartheta) = \sqrt{\phi_1^2 + \phi_2^2 + 2\phi_1\phi_2 \cos(2\vartheta)}. \tag{5.3}$$

The function $\delta(\vartheta)$ is plotted in Figure 5.5 for different values of ϕ_1, ϕ_2. We observe that δ varies between the maximum $\phi_1 + \phi_2$ at $\vartheta = 0$ and the minimum $|\phi_1 - \phi_2|$ at $\vartheta = 90°$. This can be intuitively understood in terms of rotating two waveplates either in a way that the fast axes align (retardation adds up) or in a way that the fast axis of one plate is aligned with the slow axis of the other one (retardation subtracts).

We note that for $\phi_1 = \phi_2$, the total phase shift δ chancels out at a sharp minimum. In this case, δ is linearised around its minimum at $\vartheta = \pi/2$ as

$$\delta_{lin}(\phi_1 = \phi_2) \approx 2\phi_1|\vartheta - \frac{\pi}{2}|. \tag{5.4}$$

Relationship between phase shift and frequency splitting

Assuming two longitudinal modes with frequency ν_1 and ν_2 that are resonant to a cavity of length L and differing by a phase shift δ, it must hold (roundtrip phase matching
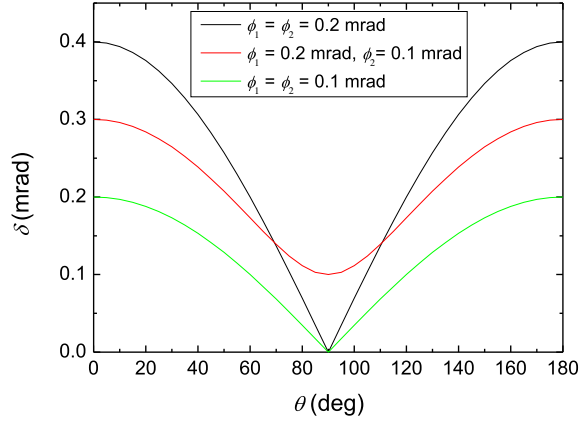
Figure 5.5: Round trip phase shift δ for the birefringent cavity depicted in Figure 5.4.

condition):

$$2\pi \frac{\nu_1}{c} 2L \quad \equiv \quad 2\pi n \,, \tag{5.5}$$

$$2\pi \frac{\nu_2}{c} 2L - \delta \quad \equiv \quad 2\pi n \,, \tag{5.6}$$

with $n = 1, 2, 3, \dots$ The frequency shift $\Delta\nu$ is

$$\Delta\nu = \nu_1 - \nu_2 = \frac{\delta}{2\pi} \cdot \frac{c}{2L} = \frac{\delta}{2\pi} \cdot FSR \,. \tag{5.7}$$

We note that $\Delta\nu$ for a given δ does not depend on the cavity finesse, but the ratio of frequency splitting to cavity linewidth $\Delta\nu_{FWHM}$ does:

$$\Delta\nu_{FWHM} \quad = \quad \frac{1}{F} \cdot FSR \,, \tag{5.8}$$

$$\frac{\Delta\nu}{\Delta\nu_{FWHM}} \quad = \quad \frac{\delta}{2\pi} \cdot F \,. \tag{5.9}$$

5.3.2 Correction to the paraxial theory

In the previous section, we have seen that a cavity features polarisation-dependent frequency splitting if it is made from mirrors that reflect orthogonally polarised light fields with a differential phase shift. In this section, we briefly summarise the analysis of [124] which shows that this is exactly what happens when we look beyond the paraxial approximation at a mirror with asymmetric geometry reflecting a Gaussian beam.

In paraxial theory, the light field of a cavity mode is purely transversally polarised. The boundary condition for the light field on the cavity mirrors is then simply that the electric field orthogonal to the propagation direction vanishes.

93

The paraxial theory can be extended to describe the light field as a vector field; a mainly transversally polarised resonator mode will then also have a small polarisation component in the direction of propagation. In this case, the boundary condition on the cavity mirror should be taken as that of an ideal electric conductor, i.e. the electric field transverse to the mirror surface vanishes.

In both cases, the boundary condition on the mirror for a transversally polarised TEM_{00} mode will correspond to an approximately spherical profile. It is shown in [124], however, that the radius of curvature (ROC) of this profile in the vector field treatment is slightly smaller than in the paraxial approximation. The mode function describing the transverse part of the electric field thus has a slightly larger ROC than the mirror that supports it. The larger ROC corresponds to a lower resonance frequency.

As this frequency difference depends on the geometric orientation of the polarisation, it introduces a polarisation dependence not present in the paraxial approximation. In [124], the authors assume a mirror with elliptical shape, i.e. a profile that can be described as an elliptic paraboloid with two principal axes having different ROC R_1, R_2, and calculate that the frequency shift $\Delta\nu$ between light (mainly) polarised along the major and minor axis corresponds to a differential phase shift ϕ (compare Equation 5.7) given by:

$$\phi = \frac{\lambda}{2\pi} \frac{R_1 - R_2}{R_1 R_2} \, . \tag{5.10}$$

5.4 Experimental measurements

This section describes the experimental measurements we have performed to investigate how to control the polarisation mode splitting by rotating one fibre about the cavity axis and the link between mirror geometry and frequency splitting.

5.4.1 Methods

Determining fibre mirror radii of curvature

A well-suited technique for characterising the concave structures on micro-fabricated fibres is optical profilometry which combines fast analysis with good spatial resolution and a non-contact measurement process. For the present work, we did not have easy access to a commercial profilometer. We have therefore used a simple white light interferometry scheme to roughly characterise the symmetry of a microfabricated structure with a compact setup that can be built up close to the CO_2 fabrication apparatus.[2]

The basic idea is to make an interferometric measurement by imaging the machined fibre facet with an interferometric microscope objective[3]. This component looks like a standard microscope objective but includes a reference mirror in the centre of the objective lens and an additional semi-transparent mirror to realise a Mirau interferometer.

---

[2]The setup and the analysis scheme were originally devised by D. Hunger.
[3]20X Nikon CF IC Epi Plan DI.

A tube lens[4] serves to create an image on a CCD camera[5]. Figure 5.6a shows a typical image recorded with our setup in which we illuminate the sample with a high power LED with wavelength $\lambda = 505\,\text{nm}$[6]. The image exhibits interference fringes which are related to the distance between the sample surface and the semi-transparent mirror inside the objective. Specifically, a difference in distance Δz leads to a phase shift of $\Delta \varphi \approx 4\pi/\lambda \Delta z$ which means that the resulting image shifts, say, from constructive to destructive interference for $\Delta z = \lambda/4 \approx 126\,\text{nm}$. Under the assumption that there are no 2π phase jumps between adjacent fringes (which is valid for the smooth surfaces created by laser fabrication), this allows a rough reconstruction of the sample surface profile along a 1d cut. We first extract the position of minima and maxima in the pixel brightness along one axis in the image, as shown in Figure 5.6b. Setting the central position to correspond to sample heigth $z = 0$, we assume that z increases by $\Delta z = \lambda/4$ with each successive extremum (which corresponds to assuming a concave sample). The resulting profile is shown in Figure 5.6c. For the present work, we are interested in the ROC close to the centre of the fibre. We therefore determine the ROC R by fitting the parabola $f(x) = \frac{1}{2R}x^2$ to the central part of the reconstructed profile. To characterise the elliptic asymmetry of the concave structure, we determine the ROC R_1, R_2 along two orthogonal axes, inspecting the interferometric image by eye to determine the orientation of the axis with the larger ROC R_1.

We have compared the results from this simple measurement method with the ones obtained from a commercial optical profilometer[7] and found that they, in general, agree to within 15%. The described method reports systematically about 10% higher values than the profilometer, which can be explained by the fact that we sample the profile not in its centre but further out where the local ROC is higher than in the centre (compare Figure 5.2b).

Measuring the frequency splitting

To measure the polarisation mode splitting in Fabry-Perot cavities made of two micromachined fibres, we use the setup shown in Figure 5.7. The general idea is to measure the resonator transmission while scanning the cavity length L over the two resonances corresponding to the two polarisation modes. We use frequency-locked laser light at about 780 nm that is phase-modulated by an EOM to create sidebands at known frequency to serve as a frequency markers. The light polarisation ε_2 incident onto the cavity can be controlled with one half- and one quarter waveplate before the input fibre (which is single-mode in our experiments). The input fibre is fixed on a 3-axes micro-positioning stage[8] that allows us to scan the cavity length by means of a piezo actuator. The out-

---

[4]Nikon f=200 mm tube lens, Edmund Optics Stock No. #58-520.

[5]IDS Ueye UI-2230SE.

[6]Thorlabs M505L3.

[7]Fogale Micromap 3D in the group of D. Chateney at the Laboratoire de Physique Statistique (LPS ENS). The specified resolution is 0.1 nm, the effective resolution is limited by vibrations to several tens of nm.
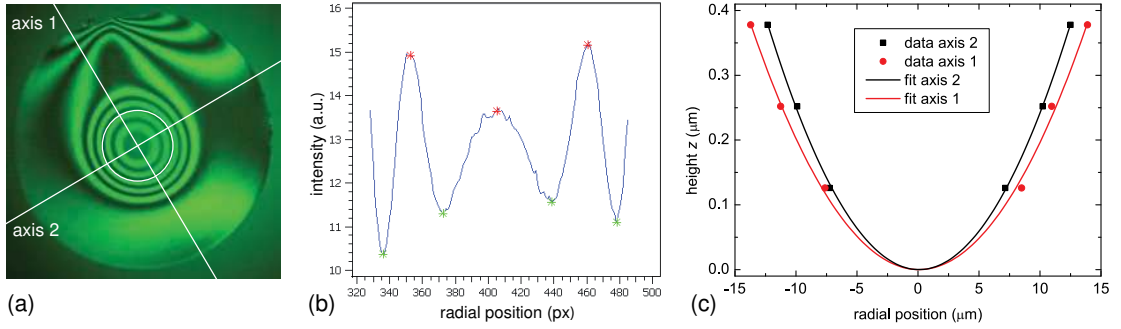
[8]Thorlabs NanoMax.

Figure 5.6: Determination of ROC using an interferometric measurement. (a): Interferometric microscope image of a microfabricated fibre facet ($\varnothing 125\mu$m). The white circle limits the region for the subsequent reconstruction. (b): Intensity cut of the image along axis 1. (c): Reconstructed profile cuts along the two axes. Parabola fits give $R_1 = 250\,\mu$m and $R_2 = 210\,\mu$m.

coupling fibre is placed into a precision rotation mount[9] that can be adjusted manually to change the roll angle ϑ between the fibres. Fibre alignment can be observed along two axes with two video microscopes[10] (resolution about 5 μm). We usually use multimode fibres on the outcoupling side which means that the polarisation of the transmitted light is scrambled. We therefore detect it non-polarisation resolved with a single photodiode (PD1).

Figure 5.8 shows a typical transmission measurement made with this setup. The EOM was operated at 2 GHz and the waveplates were aligned to excite both polarisation modes equally. By fitting a compound of six Lorentzians to the measured transmission trace, we can extract the linewidths [11] $\Delta\nu_{FWHM}^{(1)}$ and $\Delta\nu_{FWHM}^{(2)}$ and the frequency splitting $\Delta\nu$. This measurement is affected by noise from mechanic vibrations that change the cavity length, we therefore average the results over 20 scans. The analysis method described so far fails if the frequency splitting $\Delta\nu$ is on the order of or smaller than the linewidth $\Delta\nu_{FWHM}$ because then two transmission peaks merge into a single broad peak which the fitting routine cannot resolve. Keeping the same method of measuring the cavity transmission, we use a modified analysis to determine small frequency splittings by assessing the width of the broadened peak. This scheme is described in detail in Appendix E.

We have determined the free spectral range FSR by simultaneously sending in light at a second wavelength (about 830 nm) and comparing the frequency difference between the resonances of successive longitudinal modes. We then calculate the round-trip phase shift δ according to Equation 5.7 as

---

[9]Thorlabs HFR-007.
[10]Veeho VMS-004D.
[11]For averaged results, we find that $\Delta\nu_{FWHM}^{(1)} \approx \Delta\nu_{FWHM}^{(2)}$, from shot to shot, however, the linewidths can vary due to noise.
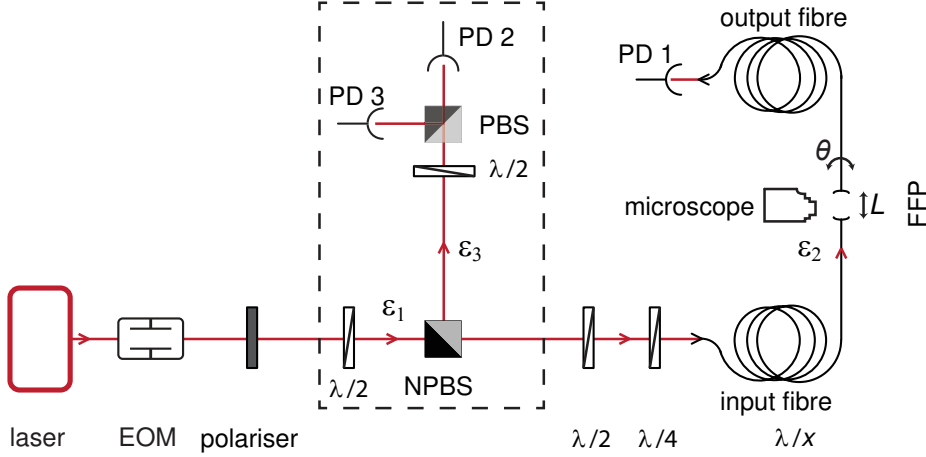
Figure 5.7: Schematic of the experimental setup to characterise mode splitting. The part within the dashed line is used to verify the polarisation angle ε_2 of the light incident on the cavity as described in Appendix E.

$$\delta = 2\pi \frac{\Delta\nu}{FSR}\,. \tag{5.11}$$

5.4.2 Results

Controlling the polarisation mode splitting by fibre rotation

We have used the methods described in the previous section to measure the frequency splitting of polarisation modes in fibre-fibre cavities when varying the roll angle ϑ between the fibres. Figure 5.9 shows two typical results together with fitted curves derived from the model presented in Section 5.3.1, specifically Equation 5.3 describing the round trip phase shift $\delta(\vartheta)$. The two data sets correspond to two different fibre-fibre cavities. In both cases, we observe that the measured δ shows, as expected, a maximum and a minimum when ϑ is varied by about 90°.

For the cavity made from fibres A and B (upper panel in Figure 5.9), the round trip phase shift can be controlled within $140\,\mu\text{rad} \lesssim \delta \lesssim 180\,\mu\text{rad}$. The measured dependence $\delta(\vartheta)$ is well reproduced by Equation 5.3 with the fitting parameters $\phi_1 = 158(15)\,\mu\text{rad}$ and $\phi_2 = 22(6)\,\mu\text{rad}$.

For the cavity made from fibres G and J (lower panel in Figure 5.9), the measured dependence $\delta(\vartheta)$ is well fit with the differential phase shifts $\phi_1 = 126(13)\,\mu\text{rad}$ and $\phi_2 = 122(13)\,\mu\text{rad}$. As ϕ_1 and ϕ_2 are closely matched, we observe in particular a cancellation of the resulting polarisation mode splitting at $\vartheta \approx 90°$ (we measure $\Delta\nu/\Delta\nu_{FWHM} \approx 0.3^{+0.05}_{-0.15}$).
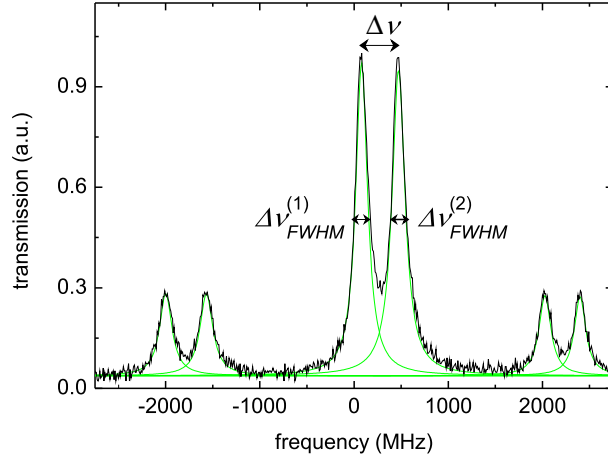
97

Figure 5.8: Measuring the frequency splitting of the polarisation modes in an FFP cavity. Transmission (black line) is measured while the cavity length is scanned over both resonances. Modulating the probing light with an EOM produces sidebands that serve as frequency calibration. A fit (green lines) is used to extract the linewidths $\Delta\nu^{(1)}_{FWHM}, \Delta\nu^{(2)}_{FWHM}$ of the two resonances and the splitting $\Delta\nu$.

Dependence of phase shift on mirror geometry

We have investigated how the differential phase shift ϕ of a microfabricated fibre depends on the geometry of the concave structure. To characterise the geometry, we describe it as an elliptic paraboloid with radius of curvature R_1 along a major axis and ROC $R_2 < R_1$ along a minor axis, measuring R_1, R_2 as described in Section 5.4.1.

As demonstrated by the experiment described above, measuring $\delta(\vartheta)$ for a fibre-fibre cavity can be used to determine the differential phase shifts ϕ_1, ϕ_2 of the fibres. However, from one such measurement we do not know which fibre causes which phase shift. To unambiguously assign each fibre its intrinsic phase shift ϕ, we have formed cavities from permutations of a set of fibres with different ϕ, each time measuring $\delta(\vartheta)$ in the resulting cavity.

The result is presented in Figure 5.10, which shows the differential phase shift ϕ as a function of $\epsilon = (R_1 - R_2)/(R_1 R_2)$. Fibres A-D were fabricated in our lab for the group of A. Kuhn, they have a dielectric mirror coating with a centre wavelength of $\lambda = 780\,\text{nm}$, transmission $T \approx 8\,\text{ppm}$, losses $L \approx 24\,\text{ppm}$ (corresponding to a finesse of $F \approx 100000$). All other fibres were fabricated by the group of D. Hunger, the mirror coatings have a centre wavelength of $\lambda = 780\,\text{nm}$, transmission $T \approx 10\,\text{ppm}$, losses $L \approx 12\,\text{ppm}$ ($F \approx 130000$).

We see clearly that the phase shift increases monotonically with increasing ϵ corresponding to stronger asymmetry. Comparing the experimental data with the prediction of Equation 5.10, we find reasonable agreement within the experimental uncertainties. The data lie systematically slightly above the predicted function $\phi(\epsilon)$. This can be ex-
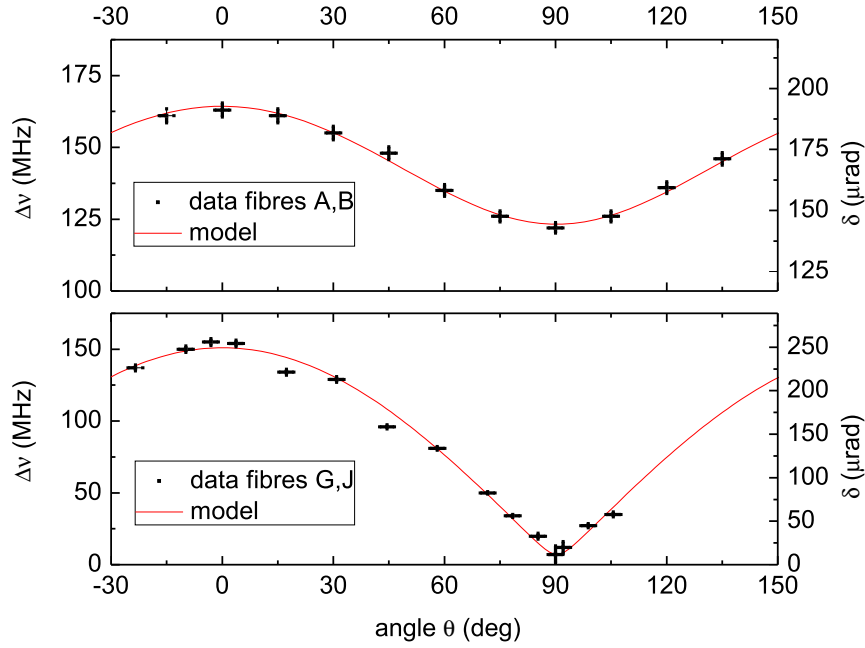
Figure 5.9: Frequency splitting $\Delta\nu$ and round trip phase shift δ as functions of roll angle ϑ. Upper panel: Cavity formed by two fibres with differing phase shifts $\phi_1 \approx 145\,\mu\text{rad}$, $\phi_2 \approx 25\,\mu\text{rad}$. The cavity parameters are $L \approx 32\,\mu\text{m}$, $\Delta\nu_{FWHM} \approx 48\,\text{MHz}$, $F \approx 100000$. Lower panel: Cavity formed by two fibres with closely matched differential phase shifts $\phi_1 \approx 125\,\mu\text{rad}$, $\phi_2 \approx 120\,\mu\text{rad}$. The cavity parameters are $L \approx 39\,\mu\text{m}$, $\Delta\nu_{FWHM} \approx 30\,\text{MHz}$, $F \approx 130000$.
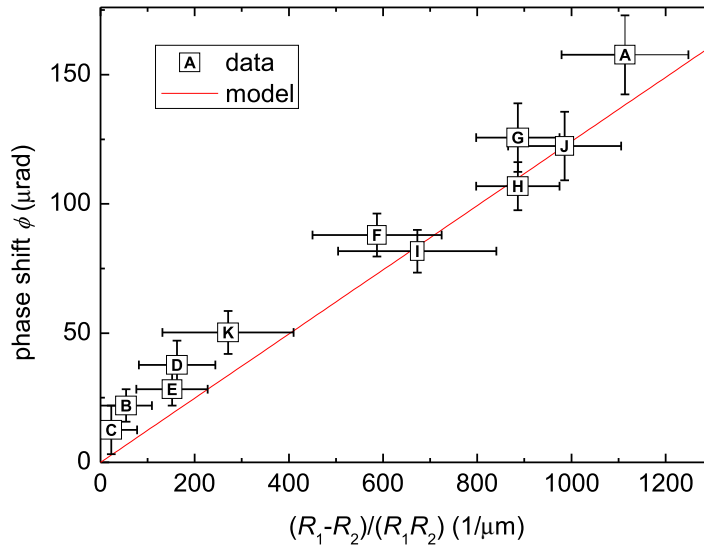

Figure 5.10: Differential phase shift ϕ as a function of mirror geometry. The red line is the prediction of Equation 5.10.

99

plained by the fact that our way of determining R_1 and R_2 systematically overestimates the radii of curvature encountered by the cavity light mode, as explained in Section 5.4.1.

We conclude that the observed differential phase shifts arise mostly from the geometry of the microfabricated fibre. The influence of eventual asymmetries or stresses in the dielectric mirror coating seem to be of minor importance.

Discussion

The experimental results confirm that the frequency splitting of the polarisation modes in an FFP cavity depends on two factors whose influence can be accurately modelled. The first factor are the differential phase shifts of the fibres which depend on their geometry according to Equation 5.10. For practical purposes, this aspect is determined by the fibre fabrication process. Given two fibres with certain differential phase shifts, the resulting splitting in the cavity can be varied as function of the orientation of the fibres as described by Equation 5.7. In practice, this can be controlled when mechanically mounting the FFP resonator.

Certain experimental target specifications for $\Delta\nu$ therefore translate into requirements on the processes of fibre fabrication and resonator construction. Given our experimental results, we want to discuss briefly in how far typical experimental requirements are feasible to realise in terms of fibre fabrication and cavity construction. Let us therefore consider a cavity with parameters similar to the current FFP1 ($L = 40\,\mu$m, $F = 40000$, $r_1 = 150\,\mu$m, $r_2 = 450\,\mu$m(SM), $\kappa/(2\pi) = 50\,$MHz) with the target of degenerate polarisation modes.

A basic requirement for most cQED experiments is then that the splitting should be smaller than the cavity linewidth $\Delta\nu < \Delta\nu_{FWHM}/2$. According to Equation 5.9, this requires $\delta < \frac{\pi}{F} \approx 80\,\mu$rad. We have seen that an ellipticity of 10% is not difficult to achieve which would result in differential phase shifts of $\phi_1 = 80\,\mu$rad and $\phi_2 = 30\,\mu$rad. The deviation of the roll angle from the optimum should then be (Equation 5.4) $\Delta\vartheta < 26°$. Experimentally, we should be able to construct a cavity with accuracy $\Delta\vartheta < 2°$, so this poses no problem. Assuming a state of the art dielectric coating with $F = 200000$, the overall splitting needs to be $\delta < 16\,\mu$rad. With $\phi_1 = \phi_2 = 80\,\mu$rad, we find $\Delta\vartheta < 6°$. The limit of technical feasibility for the cavity mounting would be something like $\phi_1 = 120\,\mu$rad, $\phi_2 = 130\,\mu$rad which would require $\Delta\vartheta < 3°$.

For experiments with ^{87}Rb atoms, the splitting should furthermore be small compared to the width of the D$_2$ line $\Gamma = 3\,$MHz (HWHM). The allowable round trip phase shift δ then depends on the cavity length (Equation 5.7) and for $L = 40\,\mu$m, we require $\delta < 5\,\mu$rad. Wee see from the experimental results that this is a rather stringent requirement. In terms of absolute values we have observed (in accordance with [124]) a lower limit of $20\,\mu$rad $\lesssim \phi$. For radii of curvature larger than $150\,\mu$m, we estimate reliably achievable values around $\phi \approx 80\,\mu$rad. Reaching the target δ will therefore require two fibres with well matched phases shifts so that $\delta \approx |\phi_1 - \phi_2|$. With $\phi_1 = \phi_2 = 80\,\mu$rad, the allowable deviation of the roll angle would be $\Delta\vartheta < 2°$ still within the limit of construction feasibility. We conclude that for the investigated parameter regime, from the point of

view of the technical realisation, especially the reproducibility of the fibre fabrication is important.

5.5 Outlook

We have seen in the preceding sections how the polarisation mode splitting in fibre Fabry-Perot cavities arises and how it can be controlled. Building on these insights, we have performed preliminary work to realise FFP cavities with controlled mode splitting for actual experimental use. One necessary step is to develop a method to control the roll angle between the fibres while mounting an FFP cavity in a compact way that allows integration with an atom chip. Another direction of development is to improve the CO_2 laser fabrication for better control over the geometry of the fabricated fibres.

To improve the fibre fabrication process, we have started work towards a new microfabrication apparatus which, in the meantime, has been set up successfully by colleagues in our group. The new setup was planned with the following design goals:

- Precision control over the symmetry of the the microfabricated structures. We have seen in this chapter that this is the key parameter determining the polarisation spliting which is a crucial phenomenon that can limit cQED experiments with FFP cavities.

- Precision control over the positioning of the microfabricated structures. The concave structures created with the old setup have not always been well centred on the core of the fibre. This asymmetry makes it more complicated to align the resonator in a way that optimises coupling between the fibre light mode and the TEM_{00} mode in the cavity.

- Quick and reliable production process. The old setup needed careful and time-consuming alignment of the beam shaping optics, with the observation and calibration by means of the dichroic mirror introducing a limit on the reliability of the fibre positioning. To analyse fabricated structures, it was necessary to take the sample from the fabrication to an additional profilometer setup. This step was cumbersome as it required additional manual adjustment.

The key idea to achieve these aims is to place the machining target on a high-precision motorised sample holder as shown in Figure 5.11. The holder is placed on three translation stages, first a horizontal linear motor stage with 150 mm travel [12] which carries a vertical linear motor stage with 30 mm travel[13]. Both stages feature a linear encoder with 50 nm resolution and a specified bidirectional repeatability of 0.2 μm. The vertical stage carries a slip-stick piezo stage [14] with 1 nm resolution, 50 nm bidirectional repeatability and 30 mm total travel. The sample holder is fixed to this nanopositioning stage.

---

[12]Newport GTS150.
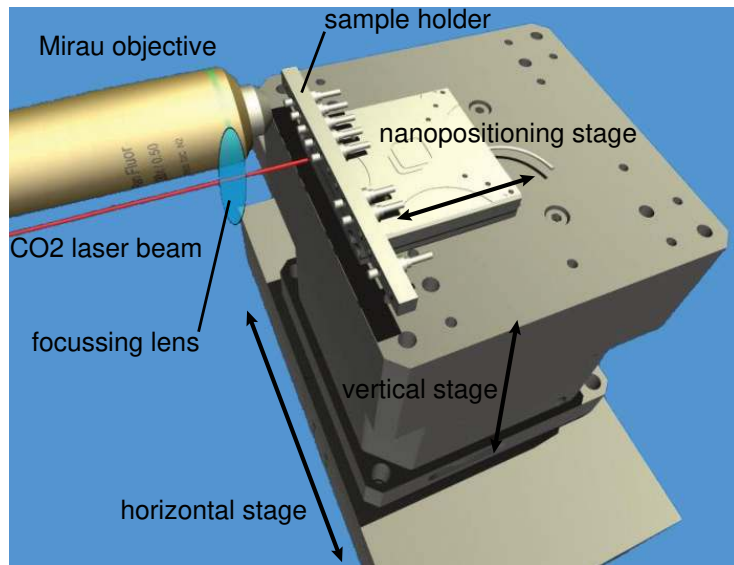[13]Newport GTS30V.
[14]Attocube ECS5050/NUM.

Figure 5.11: Schematic of the new CO_2 laser microfabrication setup.

The setup integrates the interferometry apparatus described in Section 5.4.1 which is mounted on an axis parallel to the optical axis of the CO_2 laser fabrication beam. Due to the large horizontal travel, a sample can be machined with the laser beam, then displaced to perform interferometric analysis "in situ", without any repeated handling and manual alignment. The nanopositioner makes it possible to perform scanning length profilometry to obtain the full reconstruction of the sample surface profile.

This setup is already operational and has been used to produce new fibres suitable for FFP cavities. Preliminary results are promising and show that the system indeed realises sub-micrometer position accuracy and the possibility to control fibre mirror symmetry to a high degree.

5.6 Conclusion

In this chapter, we have discussed the problem of polarisation mode splitting in fibre Fabry-Perot cavities. We have shown that this phenomenon arises from geometric asymmetry of the concave microfabricated structures which is due to imperfections in the CO_2 laser fabrication process. We have experimentally investigated the relationship between fibre geometry and frequency splitting in a cavity as well as the possibility to control the splitting by rotating one fibre around the cavity axis. The results confirm that the frequency splitting can be minimised by using symmetrically fabricated structures and controlled by adjusting the roll angle between the fibres. We expect that it is feasible in practice to mount a cavity with degenerate polarisation modes. These insights have led to preliminary work towards an improved fabrication setup that achieves greatly enhanced control over the geometry of the microfabricated structures.

Conclusion and Outlook

Multiparticle quantum entanglement and its generation are two important concepts currently studied in quantum physics, not least because they are fundamental resources for advanced quantum technology applications. In the first part of this thesis, we have shown experimentally, to our knowledge for the first time, how multiparticle entanglement can be deterministically generated by means of quantum Zeno dynamics (QZD). Our scheme exploits a non-destructive measurement to induce QZD in an ensemble of ultracold atoms strongly coupled to an optical micro-cavity.

The presented experiments give a time-resolved account of how the dynamics of the collective atomic state can be modified by a cavity-based measurement to produce multi-atom entangled quantum states. We have shown how the QZD can be engineered to generate different types of non-classical states that provide an advantage in quantum metrology applications. In an ensemble of 36 qubit atoms, we have created, despite all experimental imperfections, states with at least 3-11 entangled atoms and fidelity of up to 0.37 with respect to a W state of 36 atoms, with the preparation itself taking less than 5 μs.

So far, the generation of multiparticle entanglement by QZD is only starting to be explored. Reference [39] shows for the case of photons how, in principle, a large variety of entangled states could be produced by means of phase space tweezers based on QZD. Most other theoretical proposals focus on two-qubit systems [132, 133, 134, 135, 136]. Our results highlight that QZD can also be an experimentally feasible tool for quantum engineering of multiparticle systems. Further investigation along these lines could help to extend the scheme studied here. One possible direction would be to implement the QND measurement in a way that it does not address the pole of the Bloch sphere, but another subspace. In this way, higher order Dicke states could be produced. Similarly, combining driven Rabi oscillations with a non-demolition measurement on the equator of the Bloch sphere [137, 138] could lead to highly entangled states in the vicinity of the measurement boundary. A crucial factor to be considered will be the amount of atomic scattering due to spontaneous emission caused by the measurement.

Spontaneous emission is also the major factor limiting fidelity and purity of the created entangled states in the present experiments. This effect is exacerbated by the presence of a second polarisation mode caused by imperfections of the mirrors in the current fibre cavity setup.

Consequently, a second part of this thesis was devoted to controlling the frequency splitting of the transversal fundamental mode in fibre Fabry-Perot cavities. We have shown experimentally that the frequency splitting is determined by the symmetry of the microfabricated fibres and that it can be controlled by controlling the relative orientation of the two fibres forming a cavity.

These insights indicate several directions for future work. On the one hand, the current FFP setup could be upgraded by fitting the same atom chip with a new fibre cavity. We have performed preliminary work showing that it should be feasible to mount a cavity similar to the current one but with cancelled frequency splitting. Additionally, a state-of-the-art dielectric coating could increase the cavity finesse by a factor of four. For the QZD experiments we have performed, such an improved cavity would allow much higher state fidelity. We estimate a fidelity of up to 0.8 for the W state, before being limited by atomic scattering.

Another direct continuation of this work is the construction of an improved microfabrication setup for producing cavity fibres. This setup will enable us to reliably produce concave structures with well defined symmetry. This facilitates the construction of FFP resonators with degenerate polarisation modes, which does not only improve performance in cQED experiments but also opens up new prospects, for example coupling atomic states to the polarisation of single photons [139]. Additionally, the new setup can produce large concave structures which should allow to make high finesse, low loss FFP cavities that are one order of magnitude longer than what was previously possible. This is especially interesting for cQED experiments with trapped ions, where longer cavities reduce the detrimental effects of having dielectric surfaces close to the ions [123, 140].

Making use of these new possibilities, our group is currently building up a new experiment centred around a next-generation FFP resonator. This resonator will benefit from a state-of-the-art dielectric mirror coating which is doubly resonant at 780 nm and 1560 nm. Light at 1560 nm will create a one-dimensional intra-cavity optical lattice, where the lattice spacing is the atomic transition wavelength of 780 nm. In this way, all lattice sites are equally and maximally coupled to the resonant probe field. The lattice sites are loaded with single atoms by operating the dipole trap in the collisional blockade regime [141]. The FFP cavity will be rather long ($\sim 100\,\mu$m) to give ample optical access for transverse laser beams for advanced atom cooling schemes and it will be engineered to have a large frequency splitting between the polarisation eigenmodes. These features will make it a versatile tool to investigate not only QZD and entanglement generation, but also to implement the cavity-based effective Dicke model proposed in [142] and study the predicted entanglement close to the quantum phase transition of the Dicke system [143].

Appendix A

Rubidium 87 hyperfine structure
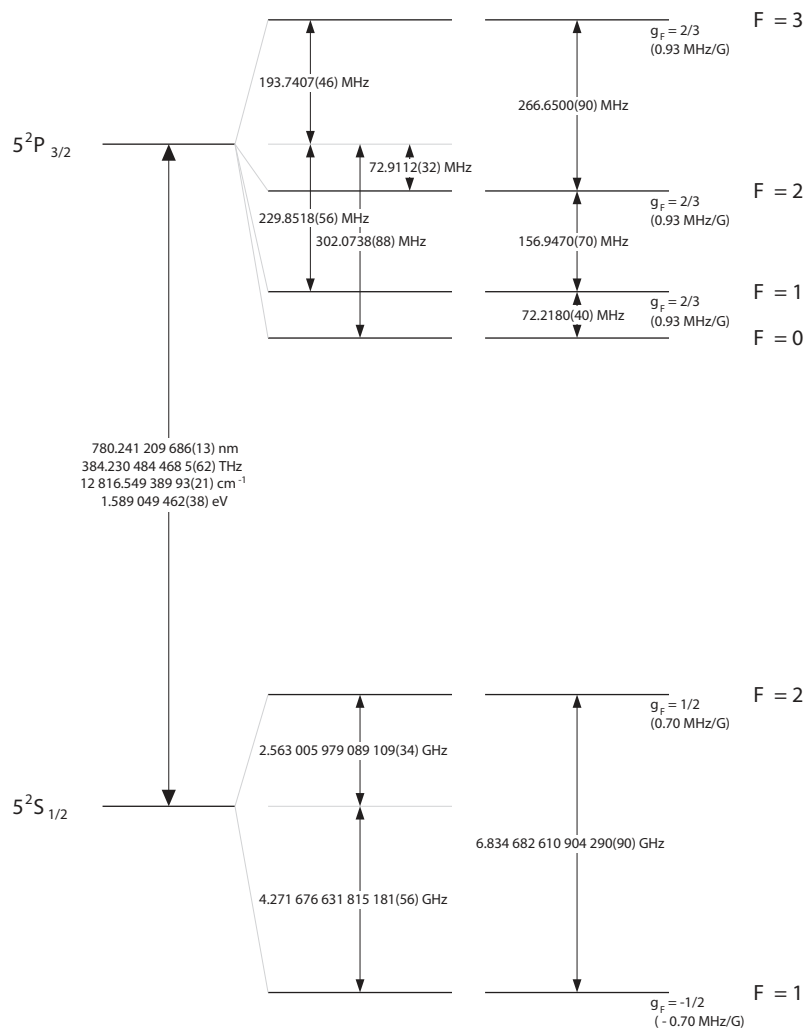

Figure A.1: Rubidium 87 D_2 transition hyperfine structure. Source: [144].

Appendix B

Probe-Main laser beat lock

The error signal between probe and main laser is generated with the components shown in Figure B.1. The scheme is similar to the ones discussed in [145, 146].
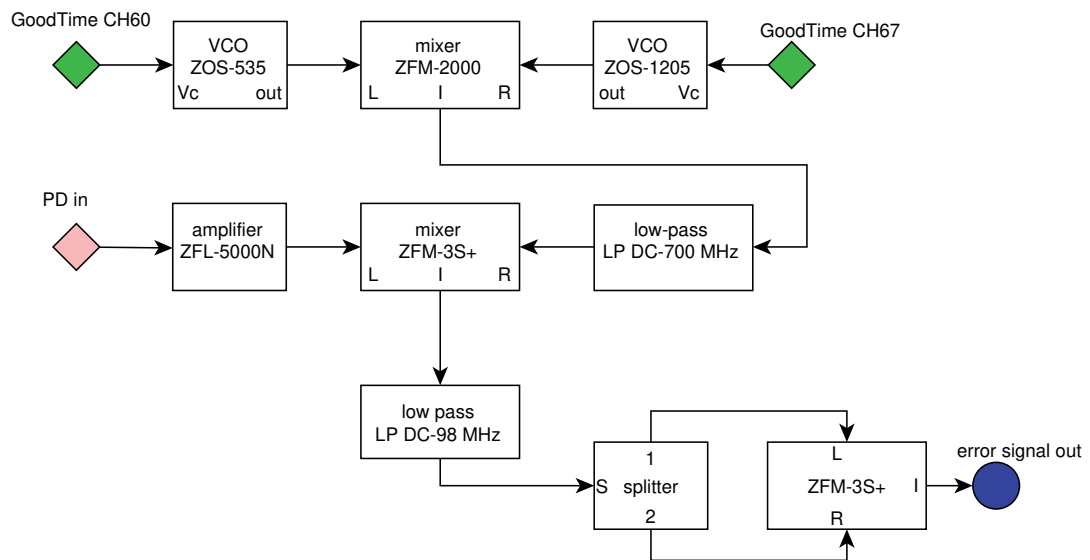
Figure B.1: Schematic of the RF electronics to generate the error signal between main and probe laser.

Appendix C

Probe and repump power control

The full schematic of the probe power control explained in Section 2.7.2 is shown in Figure C.1. The sample-and-hold (S&H) circuit controlled by the TTL "ZenoSH" is to work around the limitation that "aomvoltage" is the only analogue output available on the real-time micro-controller. The power buffer is necessary to drive the attenuator which needs up to 30 mA input current. The additional switches in the right side of the schematic are necessary because in the experiment, the repumper AOM on the main table and the probe AOM on the locking table are driven with the same RF. This was done to use the "detection" variable attenuator controlled by "aomvoltage" for both repumper and probe (more AdWin analogue outputs would simplify things). During MOT loading, the repumper is controlled via the GoodTime "Repumper TTL", with the "ZenoTTL" being set so that the switch before the amplifier lets the signal pass. Before the control is given to the micro-controller for the science phase of the experiment, the switch controlled by "Repumper TTL" is set to pass and "Zeno TTL" is set so that the "MW pulse" TTL controls the last switch to produce the light pulse.
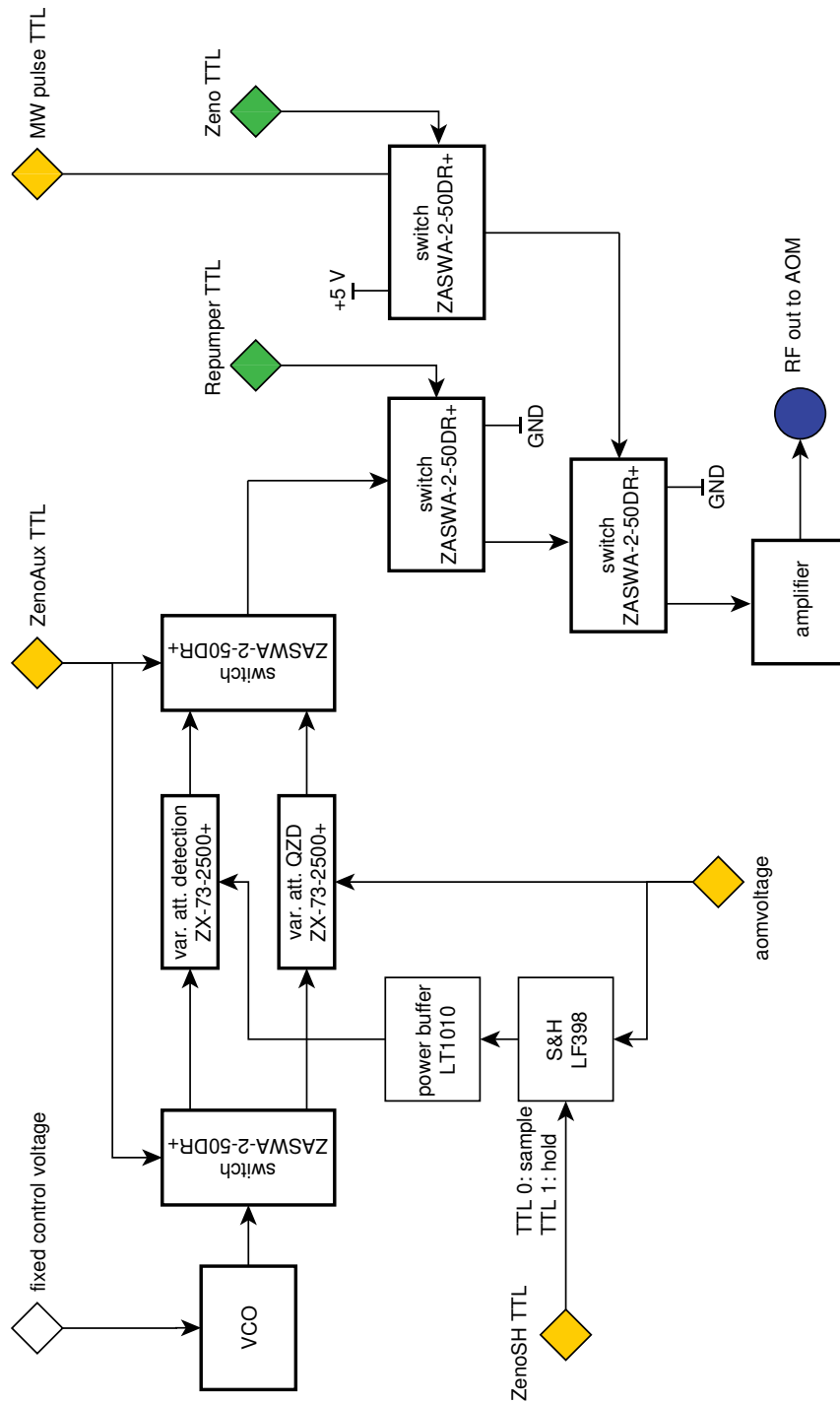
Figure C.1: Full schematic of the RF electronics to regulate the probe intensity during the QZD. Thick outlines indicate components from Minicircuits, thin outlines are electronic ICs. Yellow (green) diamonds indicate input from the real-time micro-controller (experiment control software).

Appendix D

Calculation of round trip phase shift

The total system consisting of both birefringent mirrors is described by the Jones matrix (Equation D.1):

$$
\begin{aligned}
\underline{M}_{tot} &= \underline{R}^{-1}(-\vartheta_2)\underline{M}_2(\phi_2)\underline{R}(\vartheta_2)\underline{M}_1(\phi_1) & \text{(D.1)} \\
&= \begin{pmatrix} \cos^2(\vartheta) + e^{i\phi_2}\sin^2(\vartheta) & e^{i\phi_1}\left(e^{i\phi_2}-1\right)\cos(\vartheta)\sin(\vartheta) \\ \left(e^{i\phi_2}-1\right)\cos(\vartheta)\sin(\vartheta) & e^{i\phi_1}\left(e^{i\phi_2}\cos^2(\vartheta)+\sin^2(\vartheta)\right) \end{pmatrix}. & \text{(D.2)}
\end{aligned}
$$

where $\underline{R}(\vartheta) = \begin{pmatrix} \cos(\vartheta) & -\sin(\vartheta) \\ \sin(\vartheta) & \cos(\vartheta) \end{pmatrix}$.

The matrix $\underline{M}_{tot}$ has two eigenvectors that correspond to two eigenmodes of the cavity. The eigenvalues are

$$
\begin{aligned}
\lambda_{1/2} &= \frac{1}{4}\left(\left(e^{i\phi_1}+1\right)\left(e^{i\phi_2}+1\right) + \left(e^{i\phi_1}-1\right)\left(e^{i\phi_2}-1\right)\cos(2\theta)\right) & \text{(D.3)} \\
&\pm \frac{1}{4}\sqrt{-16e^{i(\phi_1+\phi_2)} + \left((e^{i\phi_1}+1)(e^{i\phi_2}+1) + (e^{i\phi_1}-1)(e^{i\phi_2}-1)\cos(2\theta)\right)^2}.
\end{aligned}
$$

In our case $\phi_1, \phi_2 \ll 1$, so that we can expand the different terms in Equation D.3 up to quadratic terms in ϕ:

$$
\begin{aligned}
e^{i(\phi_1+\phi_2)} &= 1 + i(\phi_1+\phi_2) - \frac{1}{2}(\phi_1+\phi_2)^2 + \mathcal{O}(\phi^3) \\
\left(e^{i\phi_1}+1\right)\left(e^{i\phi_2}+1\right) &= 4 + 2i(\phi_1+\phi_2) - (\phi_1^2+\phi_2^2) - \phi_1\phi_2 + \mathcal{O}(\phi^3) \\
\left(e^{i\phi_1}-1\right)\left(e^{i\phi_2}-1\right) &= \phi_1\phi_2 + \mathcal{O}(\phi^3).
\end{aligned}
$$

Equation D.3 then becomes

$$\lambda_{1/2} = \frac{1}{4}\left(4 - (\phi_1^2 + \phi_2^2) + \phi_1\phi_2(\cos(2\theta) - 1)\right) + i\frac{1}{2}\left((\phi_1 + \phi_2) \pm \sqrt{\phi_1^2 + \phi_2^2 + 2\phi_1\phi_2\cos(2\theta)}\right).$$

(D.4)

The phase shift each each mode experiences during a round trip, is given by the complex argument of Equation D.4. The differential round trip phase shift δ is thus

$$\delta = \arg(\lambda_1) - \arg(\lambda_2) \approx \sqrt{\phi_1^2 + \phi_2^2 + 2\cos(2\theta)},$$

(D.5)

where we have used that the real part $\mathrm{Re}\{\lambda_{1/2}\} \approx 1$ for $\phi_1, \phi_2 \ll 1$.

The total system described by Equation 5.2 behaves like a waveplate with effective retardation δ with the fast axis at an angle ϑ_{eff} with respect to the optical axis. ϑ_{eff} can be found calculating the eigenvectors; in [130] it is shown that:

$$\cos(2\vartheta_{\mathrm{eff}}) = \frac{\frac{\phi_1}{\phi_2} + \cos(2\vartheta)}{\sqrt{\left(\frac{\phi_1}{\phi_2} - 1\right)^2 + 4\frac{\phi_1}{\phi_2}\cos^2(\vartheta)}}.$$

(D.6)

Appendix E

Measuring small frequency splittings

The analysis method described in Section 5.4.1 fails if the frequency splitting $\Delta\nu$ is on the order of or smaller than the linewidth κ because then the fitting routine cannot resolve the two transmission peaks.[1] Keeping the same method of measuring the cavity transmission, we have modified the analysis to determine small frequency splittings. We fit the compound peak formed by both resonances with a single Lorentzian and extract the splitting from its width which will be broadened according to $\Delta\nu$. Figure E.1 shows the calculated result obtained when fitting a single Lorentzian $\mathcal{L}(\kappa', x'_c, A')$ of the form

$$\mathcal{L}(\kappa, x_c, A) = \frac{A}{1 + (\frac{x-x_c}{\kappa})^2} \tag{E.1}$$

to the sum $L(\kappa, 0, A) + L(\kappa, \Delta\nu, A)$. We observe that the splitting $\Delta\nu$ can be extracted from the total linewidth κ' if we know κ. Determining the splitting in this way is subject to an uncertainty arising from fluctuations of κ_1/κ_2 and A_1/A_2, which become more important as $\Delta\nu$ decreases. Given our experimental uncertainties, splittings $\Delta\nu < \kappa$ can only be estimated with relative error of 40% and more. For $\kappa \lesssim \Delta\nu \lesssim 2\kappa$, however, the relative error of this simple method reduces to the order of 10%. In the present work, we therefore use it to estimate an upper bound for $\Delta\nu$ in cases where $\Delta\nu \lesssim 2\kappa$.

The transmission measurement itself requires a bit more care for small frequency splitting. We need to determine both the individual linewidth κ and the broadened total linewidth κ'. One possible way to do this is to have linear polarisation with angle ε_2 incident on the cavity. Scanning ε_2 by 90°, we will successively excite, say, only the first polarisation eigenmode, then both eigenmodes and then only the second one. The width of the transmission peak κ_{tot} will then change accordingly from κ to κ' and back to κ.

Controlling ε_2 is slightly complicated by the fact that the incoming SM fibre shows variable birefringence which changes due to unavoidable external mechanical stresses. The waveplates before the input fibre can be used to compensate this unknown birefringence, and in the case of large $\Delta\nu$, ε_2 can be scanned simply by adjusting the waveplates according to the observed transmission signal. If we cannot resolve $\Delta\nu$, the polarisation

---

[1] In this appendix, we define $\kappa \equiv \Delta\nu_{FWHM}/2$ as opposed to the rest of the thesis where $\kappa/(2\pi) \equiv \Delta\nu_{FWHM}/2$.
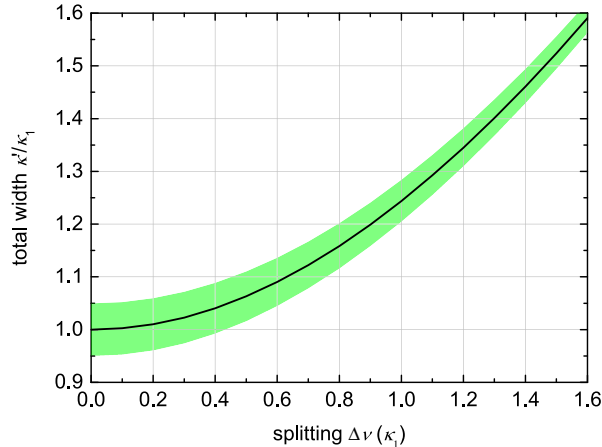
Figure E.1: Total width κ'/κ_1 of a single Lorentzian $L(\kappa', x'_c, A')$ that fits the sum $L(\kappa_1, 0, A) + L(\kappa_2, \Delta\nu, A)$. Given an experimentally measured value for κ'/κ_1, we can find the frequency splitting $\Delta\nu$. The uncertainty of κ_2/κ_1 translates into an uncertainty on the determined $\Delta\nu$ indicated by the green shaded bounds.

angle ε_2 is inaccessible to us. However, we can gain additional information from the light that is reflected from the cavity, passing forth and back through the birefringent piece of input fibre. This situation can be understood in terms of the optical reversibility theorems presented in [147] that describe how to determine the polarisation at a remote position (in our case ε_2) by measuring the polarisation angle ε_1 of the light sent towards the element of unknown birefringence (the input fibre) and the angle ε_3 of the light retro-reflected behind this element. We want the polarisation ε_2 to be linear which, according to Theorem I in [147] is the case if and only if ε_1 is linear and parallel to ε_3.

Experimentally, we ensure that this condition is met by means of the optical setup shown within dashed lines in Figure 5.7. The non-polarising beamsplitting cube can be replaced by a mirror to alternatively analyse the polarisation ε_1 or ε_3 with the setup consisting of a half wave plate, a polarising beamsplitter and the photodiodes PD2 and PD3. The waveplates after the NPBC are adjusted to ensure ε_3 is linearly orthogonally polarised with respect to ε_1. Once this is the case, the half wave plate before the NPBS can be rotated to perform the transmission measurement while scanning the angle of ε_2.

The result of such a measurement is shown in Figure E.2. As expected, changing ε_2 by $45°$ allows us to excite either one or both polarisation modes to measure κ and κ'. For the displayed measurement, we extract a maximal/minimal linewidth of $\kappa_{tot} \approx 20\,\text{MHz}/18\,\text{MHz}$ from which we calculate a splitting of $\kappa'/\kappa \approx 20/18 \approx 1.1$. Comparing with Figure E.1, we estimate the frequency splitting $\Delta\nu \approx (0.65^{+0.1}_{-0.2})\kappa$. We note that one such scan determines $\Delta\nu$ at one specific roll angle ϑ between the two fibres, changing ϑ also changes the mechanical stress on the input fibre change, so that the waveplates have to be readjusted as described above.
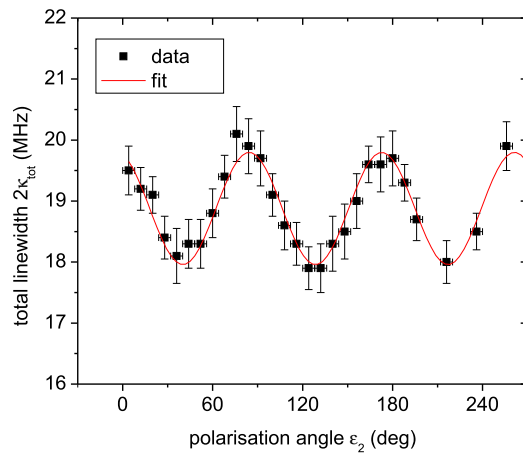
Figure E.2: Measurement of the total linewidth κ_{tot} for frequency splitting $\Delta\nu < \kappa$. The data are averaged over 20 repetitions, vertical bars show the statistical error.

Bibliography

[1] S. Haroche and J.-M. Raimond, *Exploring the Quantum* (Oxford University Press, Oxford, 2006).

[2] E. M. Purcell, "Spontaneous emission probabilities at radio frequencies," Phys. Rev. **69**, 681– (1946).

[3] M. Brune, J. Raimond, P. Goy, L. Davidovich, and S. Haroche, "Realization of a two-photon maser oscillator," Phys. Rev. Lett. **59**, 1899–1902 (1987).

[4] C. Sayrin, I. Dotsenko, X. Zhou, B. Peaudecerf, T. Rybarczyk, S. Gleyzes, P. Rouchon, M. Mirrahimi, H. Amini, M. Brune, J.-M. Raimond, and S. Haroche, "Real-time quantum feedback prepares and stabilizes photon number states," Nature **477**, 73–77 (2011).

[5] R. J. Thompson, G. Rempe, and H. J. Kimble, "Observation of normal-mode splitting for an atom in an optical cavity," Phys. Rev. Lett. **68**, 1132–1135 (1992).

[6] H. J. Kimble, "Strong interactions of single atoms and photons in cavity QED," Phys. Scr. **T76**, 127–137 (1998).

[7] P. W. H. Pinkse, T. Fischer, P. Maunz, and G. Rempe, "Trapping an atom with single photons," Nature **404**, 365–368 (2000).

[8] C. J. Hood, T. W. Lynn, A. C. Doherty, A. S. Parkins, and H. J. Kimble, "The atom-cavity microscope: single atoms bound in orbit by single photons," Science **287**, 1447–1453 (2000).

[9] J. McKeever, A. Boca, A. Boozer, R. Miller, J. Buck, A. Kuzmich, and H. Kimble, "Deterministic generation of single photons from one atom trapped in a cavity," Science **303**, 1992–1994 (2004).

[10] M. Hennrich, A. Kuhn, and G. Rempe, "Transition from antibunching to bunching in cavity QED," Phys. Rev. Lett. **94**, 053604– (2005).

[11] M. Muecke, E. Figueroa, J. Bochmann, C. Hahn, K. Murr, S. Ritter, C. J. Villas-Boas, and G. Rempe, "Electromagnetically induced transparency with single atoms in a cavity," Nature **465**, 755–758 (2010).

[12] B. Casabone, A. Stute, K. Friebe, B. Brandstätter, K. Schüppert, R. Blatt, and T. E. Northup, "Heralded entanglement of two ions in an optical cavity," Phys. Rev. Lett. **111**, 100505 (2013).

[13] A. Wallraff, D. Schuster, A. Blais, L. Frunzio, R.-S. Huang, J. Majer, S. Kumar, S. M. Girvin, and R. J. Schoelkopf, "Strong coupling of a single photon to a superconducting qubit using circuit quantum electrodynamics," Nature **431**, 162–167 (2004).

[14] J. P. Reithmaier, G. Sek, A. Loffler, C. Hofmann, S. Kuhn, S. Reitzenstein, L. V. Keldysh, V. D. Kulakovskii, T. L. Reinecke, and A. Forchel, "Strong coupling in a single quantum dot-semiconductor microcavity system," Nature **432**, 197–200 (2004).

[15] E. Schrödinger, "Discussion of probability relations between separated systems," Math. Proc. Camb. Phil. Soc. **31**, 555 563 (1935).

[16] E. Schrödinger, "Die gegenwärtige Situation in der Quantenmechanik," Die Naturwissenschaften **23**, 823 (1935).

[17] R. Horodecki, P. Horodecki, M. Horodecki, and K. Horodecki, "Quantum entanglement," Rev. Mod. Phys. **81**, 865 (2009).

[18] P. Zoller, T. Beth, D. Binosi, R. Blatt, H. Briegel, D. Bruss, T. Calarco, J. I. Cirac, D. Deutsch, J. Eisert, A. Ekert, C. Fabre, N. Gisin, P. Grangiere, M. Grassl, S. Haroche, A. Imamoglu, A. Karlson, J. Kempe, L. Kouwenhoven, S. Kröll, G. Leuchs, M. Lewenstein, D. Loss, N. Lütkenhaus, S. Massar, J. E. Mooij, M. B. Plenio, E. Polzik, S. Popescu, G. Rempe, A. Sergienko, D. Suter, J. Twamley, G. Wendin, R. Werner, A. Winter, J. Wrachtrup, and A. Zeilinger, "Quantum information processing and communication," EPJ D **36**, 203–228 (2005).

[19] N. Gisin, G. Ribordy, W. Tittel, and H. Zbinden, "Quantum cryptography," Rev. Mod. Phys. **74**, 145 (2002).

[20] S. Tanzilli, A. Martin, F. Kaiser, M. P. De Micheli, O. Alibart, and D. B. Ostrowsky, "On the genesis and evolution of integrated quantum optics," Laser & Photonics Reviews **6**, 115–143 (2012).

[21] C. H. Bennett and D. P. DiVincenzo, "Quantum information and computation," Nature **404**, 247–255 (2000).

[22] V. Giovannetti, S. Lloyd, and L. Maccone, "Quantum-enhanced measurements: Beating the standard quantum limit," Science **306**, 1330–1336 (2004).

[23] C. A. Sackett, D. Kielpinski, B. King, C. Langer, V. Meyer, C. Myatt, M. Rowe, Q. Turchette, W. Itano, D. Wineland, and C. Monroe, "Experimental entanglement of four particles," Nature **404**, 256–259 (2000).

[24] D. Leibfried, E. Knill, S. Seidelin, J. Britton, R. B. Blakestad, J. Chiaverini, D. B. Hume, W. M. Itano, J. D. Jost, C. Langer, R. Ozeri, R. Reichle, and D. J. Wineland, "Creation of a six-atom 'Schrödinger' cat state," Nature **438**, 639–642 (2005).

[25] L. DiCarlo, M. D. Reed, L. Sun, B. R. Johnson, J. M. Chow, J. M. Gambetta, L. Frunzio, S. M. Girvin, M. H. Devoret, and R. J. Schoelkopf, "Preparation and measurement of three-qubit entanglement in a superconducting circuit," Nature **467**, 574–578 (2010).

[26] J. A. Mlynek, J. Abdumalikov, A. A., J. M. Fink, L. Steffen, M. Baur, C. Lang, A. F. van Loo, and A. Wallraff, "Demonstrating W-type entanglement of Dicke states in resonant cavity quantum electrodynamics," Phys. Rev. A **86**, 053838– (2012).

[27] M. H. Schleier-Smith, I. D. Leroux, and V. Vuletić, "States of an Ensemble of Two-Level Atoms with Reduced Quantum Uncertainty," Phys. Rev. Lett. **104**, 073604– (2010).

[28] C. Gross, T. Zibold, E. Nicklas, J. Estève, and M. K. Oberthaler, "Nonlinear atom interferometer surpasses classical precision limit," Nature **464**, 1165–1169 (2010).

[29] M. F. Riedel, P. Böhi, Y. Li, T. W. Hänsch, A. Sinatra, and P. Treutlein, "Atom-chip-based generation of entanglement for quantum metrology," Nature **464**, 1170 (2010).

[30] B. Lücke, M. Scherer, J. Kruse, L. Pezzé, F. Deuretzbacher, P. Hyllus, O. Topic, J. Peise, W. Ertmer, J. Arlt, L. Santos, A. Smerzi, and C. Klempt, "Twin matter waves for interferometry beyond the classical limit," Science **334**, 773 (2011).

[31] F. Verstraete, M. M. Wolf, and J. I. Cirac, "Quantum computation and quantum-state engineering driven by dissipation," Nat. Phys. **5**, 633–636 (2009). 1745-2473.

[32] B. Kraus, H. Büchler, S. Diehl, A. Kantian, A. Micheli, and P. Zoller, "Preparation of entangled states by quantum Markov processes," Phys. Rev. A **78**, 042307 (2008).

[33] I. D. Leroux, M. H. Schleier-Smith, and V. Vuletić, "Implementation of cavity squeezing of a collective atomic spin," Phys. Rev. Lett. **104**, 073602 (2010).

[34] H. Krauter, C. A. Muschik, K. Jensen, W. Wasilewski, J. M. Petersen, J. I. Cirac, and E. S. Polzik, "Entanglement generated by dissipation and steady state entanglement of two macroscopic objects," Phys. Rev. Lett. **107**, 080503 (2011).

[35] J. T. Barreiro, M. Muller, P. Schindler, D. Nigg, T. Monz, M. Chwalla, M. Hennrich, C. F. Roos, P. Zoller, and R. Blatt, "An open-system quantum simulator with trapped ions," Nature **470**, 486–491 (2011). 0028-0836.

[36] Y. Lin, J. P. Gaebler, F. Reiter, T. R. Tan, R. Bowler, A. S. Sorensen, D. Leibfried, and D. J. Wineland, "Dissipative production of a maximally entangled steady state of two quantum bits," Nature **504**, 415 (2013).

[37] S. Shankar, M. Hatridge, Z. Leghtas, K. M. Sliwa, A. Narla, U. Vool, S. M. Girvin, L. Frunzio, M. Mirrahimi, and M. H. Devoret, "Autonomously stabilized entanglement between two superconducting quantum bits," Nature **504**, 419 (2013). 0028-0836.

[38] B. Misra and E. C. G. Sudarshan, "The Zeno's paradox in quantum theory," J. Math. Phys. **18**, 756–763 (1977).

[39] J. M. Raimond, C. Sayrin, S. Gleyzes, I. Dotsenko, M. Brune, S. Haroche, P. Facchi, and S. Pascazio, "Phase space tweezers for tailoring cavity fields by quantum Zeno dynamics," Phys. Rev. Lett. **105**, 213601– (2010).

[40] F. Schäfer, I. Herrera, S. Cherukatti, C. Lovecchio, F. S. Cataliotti, F. Caruso, and A. Smerzi, "Experimental realization of quantum Zeno dynamics," Nature Communications **5**, 3194 (2014).

[41] A. Signoles, A. Facon, D. Grosso, I. Dotsenko, S. Haroche, J.-M. Raimond, M. Brune, and S. Gleyzes, "Confined quantum Zeno dynamics of a watched atomic arrow," Nat. Phys. **10**, 715–719 (2014).

[42] B. Huard et al., "Quantum dynamics of an electromagnetic mode that cannot have n photons," (2014). Accepted for publication in Science.

[43] J. Volz, R. Gehr, G. Dubois, J. Estève, and J. Reichel, "Measurement of the internal state of a single atom without energy exchange," Nature **475**, 210–213 (2011).

[44] F. Haas, J. Volz, R. Gehr, J. Reichel, and J. Esteve, "Entangled states of more than 40 atoms in an optical fiber cavity," Science **344**, 180 (2014).

[45] F. Haas, "Création d'états intriqués d'un ensemble d'atomes dans une cavité optique," Ph.D. thesis, Université Pierre et Marie Curie - Paris VI (2014).

[46] D. Hunger, T. Steinmetz, Y. Colombe, C. Deutsch, T. W. Hänsch, and J. Reichel, "A fiber Fabry-Perot cavity with high finesse," New J. Phys. **12**, 065038 (2010).

[47] P. Facchi and S. Pascazio, "Quantum zeno dynamics: mathematical and physical aspects," Journal of Physics: Conference Series **196**, 012017 (2009).

[48] W. M. Itano, D. J. Heinzen, J. J. Bollinger, and D. J. Wineland, "Quantum Zeno effect," Phys. Rev. A **41**, 2295– (1990).

[49] P. G. Kwiat, A. G. White, J. R. Mitchell, O. Nairz, G. Weihs, H. Weinfurter, and A. Zeilinger, "High-Efficiency Quantum Interrogation Measurements via the Quantum Zeno Effect," Phys. Rev. Lett. **83**, 4725–4728 (1999).

[50] C. Balzer, R. Huesmann, W. Neuhauser, and P. E. Toschek, "The Quantum Zeno Effect - Evolution of an Atom Impeded by Measurement," Opt. Commun. **180**, 115 (2000).

[51] M. C. Fischer, B. Gutiérrez-Medina, and M. G. Raizen, "Observation of the Quantum Zeno and Anti-Zeno Effects in an Unstable System," Phys. Rev. Lett. **87**, 040402– (2001).

[52] E. W. Streed, J. Mun, M. Boyd, G. K. Campbell, P. Medley, W. Ketterle, and D. E. Pritchard, "Continuous and Pulsed Quantum Zeno Effect," Phys. Rev. Lett. **97**, 260402 (2006).

[53] P. Facchi and S. Pascazio, "Quantum Zeno subspaces," Phys. Rev. Lett. **89**, 080401 (2002).

[54] R. H. Dicke, "Coherence in spontaneous radiation processes," Phys. Rev. **93**, 99–110 (1954).

[55] E. Jaynes and F. Cummings, "Comparison of quantum and semiclassical radiation theories with application to the beam maser," Proc. IEEE **51**, 89–109 (1963).

[56] C. Gardiner and P. Zoller, *Quantum Noise* (Springer, 1991).

[57] H. Carmichael, *An Open Systems Approach to Quantum Optics* (Springer-Verlag, 1992).

[58] M. J. Collett and C. W. Gardiner, "Squeezing of intracavity and traveling-wave light fields produced in parametric amplification," Phys. Rev. A **30**, 1386–1391 (1984).

[59] G. Dubois, "Preparation, manipulation et detection d'atomes uniques sur une puces à atome," Ph.D. thesis, Université Pierre et Marie Curie - Paris VI (2009).

[60] G. Hechenblaikner, M. Gangl, P. Horak, and H. Ritsch, "Cooling an atom in a weakly driven high-Q cavity," Phys. Rev. A **58**, 3030– (1998).

[61] M. Tavis and F. W. Cummings, "Exact solution for an n-molecule radiation-field hamiltonian," Phys. Rev. **170**, 379–384 (1968).

[62] R. Gehr, "Cavity based high-fidelity and non-destructive single atom detection on an atom chip," Ph.D. thesis, Université Pierre et Marie Curie - Paris VI (2011).

[63] T. Steinmetz, "Resonator-Quantenelektrodynamik auf einem Mikrofallenchip," Ph.D. thesis, Ludwig-Maximilians-Universitat München (2008).

[64] D. A. Steck, "Rubidium 87 D Line Data (rev. 2.1.4 Dec. 2010)," .

[65] J. Weinstein and K. Libbrecht, "Microscopic magnetic traps for neutral atoms," Phys. Rev. A **54**, 4004–4009 (1995).

[66] J. Reichel, W. Hänsel, and T. W. Hänsch, "Atomic micromanipulation with magnetic surface traps," Phys. Rev. Lett. **83**, 3398–3401 (1999).

[67] R. Folman, P. Krüger, D. Cassettari, B. Hessmo, T. Maier, and J. Schmiedmayer, "Controlling Cold Atoms using Nanofabricated Surfaces: Atom Chips," Phys. Rev. Lett. **84**, 4749– (2000).

[68] J. Reichel, W. Hänsel, P. Hommelhoff, and T. Hänsch, "Applications of integrated magnetic microtraps," Appl. Phys. B: Lasers Opt. **72**, 81–89 (2001).

[69] W. Hänsel, J. Reichel, P. Hommelhoff, and T. W. Hänsch, "Magnetic Conveyor Belt for Transporting and Merging Trapped Atom Clouds," Phys. Rev. Lett. **86**, 608– (2001).

[70] R. Folman, P. Kruger, J. Schmiedmayer, J. Denschlag, and C. Henkel, "Microscopic atom optics: From wires to an atom chip," Adv. At. Mol. Opt. Phys. **48**, 263–356 (2002).

[71] W. Hänsel, P. Hommelhoff, T. W. Hansch, and J. Reichel, "Bose-Einstein condensation on a microelectronic chip," Nature **413**, 498–501 (2001).

[72] J. Reichel, "Microchip traps and Bose-Einstein condensation," Appl. Phys. B **74**, 469–487 (2002).

[73] J. Reichel and V. Vuletic, eds., *Atom chips* (Wiley-VCH, 2011).

[74] E. Raab, M. Prentiss, A. Cable, S. Chu, and D. Pritchard, "Trapping of Neutral Sodium Atoms with Radiation Pressure," Phys. Rev. Let. **59**, 2631–2634 (1987).

[75] E. Saleh and M. Teich, *Fundamentals of Photonics* (Wiley, 1991).

[76] R. Grimm, M. Weidemüller, and Y. B. Ovchinnikov, "Optical dipole traps for neutral atoms," Adv. At. Mol. Opt. Phys. **42**, 95–170 (2000).

[77] L. Ricci, M. Weidemüller, T. Esslinger, A. Hemmerich, C. Zimmermann, V. Vuletic, W. König, and T. W. Hänsch, "A compact grating-stabilized diode laser system for atomic physics," Opt. Commun. **117**, 541–549 (1995).

[78] G. C. Bjorklund, "Frequency-modulation spectroscopy: a new method for measuring weak absorptions and dispersions," Opt. Lett. **5**, 15–17 (1980).

[79] G. C. Bjorklund, M. D. Levenson, W. Lenth, and C. Ortiz, "Frequency modulation (FM) spectroscopy," Appl. Phys. B: Lasers Opt. **32**, 145–152 (1983-11-01).

[80] E. A. Donley, T. Heavner, F. Levi, M. Tataw, and S. Jefferts, "Double-pass acousto-optic modulator system," Rev. Sci. Instrum. **76**, 063112 (2005).

[81] R. Drever, J. Hall, F. Kowalski, J. Hough, G. Ford, A. Munley, and H. Ward, "Laser phase and frequency stabilization using an optical resonator," Appl. Phys. B: Lasers Opt. **31**, 97–105 (1983).

[82] D. Shaddock, M. Gray, and D. McClelland, "Frequency locking a laser to an optical cavity using spatial mode interference," Opt. Lett. **24**, 1499–1501 (1999).

[83] C. Monroe, W. Swann, H. Robinson, and C. Wieman, "Very cold trapped atoms in a vapor cell," Phys. Rev. Let. **65**, 1571–1574 (1990).

[84] K. Lindquist, M. Stepehens, and C. Wieman, "Experimental and theoretical study of the vapor-cell Zeeman optical trap," Phys. Rev. A **46**, 4082–4090 (1992).

[85] R. Long, T. Rom, W. Hänsel, T. W. Hänsch, and J. Reichel, "Long distance magnetic conveyor for precise positioning of ultracold atoms," Eur. Phys. J. D **35**, 125 (2005).

[86] A. Fuhrmanek, R. Bourgain, Y. R. P. Sortais, and A. Browaeys, "Study of light-assisted collisions between a few cold atoms in a microscopic dipole trap," Phys. Rev. A **85**, 062708 (2012).

[87] Radcliffe, "Some properties of coherent spin states," J. Phys. A **4**, 313–323 (1971).

[88] F. Arecchi, E. Courtens, R. Gilmore, and H. Thomas, "Atom coherent states in quantum optics," Phys. Rev. A. **6**, 2211–2237 (1972).

[89] W. Zhang, D. H. Feng, and R. Gilmore, "Coherent states: Theory and some applications," Rev. Mod. Phys. **62**, 867–927 (1990).

[90] K. Husimi, "Some Formal Properties of the Density Matrix," Proc. Phys. Math. Soc. Jpn **22**, 264–314 (1940).

[91] C. Lee, "Q representation of the atomic coherent states and the origin of fluctuations in superfluorescence," Phys. Rev. A. **30**, 3308–3310 (1984).

[92] M. Paris and J. Rehacek, eds., *Quantum State Estimation (Lecture Notes in Physics, vol.649)*, vol. 649 (Springer, 2004).

[93] G. S. Agarwal, "State reconstruction for a collection of two-level systems," Phys. Rev. A **57**, 671–673 (1998).

[94] G. Klose, G. Smith, and P. Jessen, "Measuring the quantum state of a large angular momentum," Phys. Rev. Let. **86**, 4721 (2001).

[95] J. Rehacek, Z. Hradil, and M. Jezek, "Iterative algorithm for reconstruction of entangled states," Phys. Rev. A **63**, 040303– (2001).

[96] A. Lvovsky, "Iterative maximum-likelihood reconstruction in quantum homodyne tomography," J. Opt. B: Quantum Semiclass. Opt. **6**, 556–559 (2004).

[97] B. Efron and R. Tibshirani, *An Introduction to the Bootstrap* (Chapman & Hall/CRC, 1993).

[98] R. Jozsa, "Quantum effects in algorithms," Chaos, Solitons and Fractals **10**, 1657 (1999).

[99] M. Greenberger, D.M.and Horne and Z. A., *Bell's Theorem, Quantum Theory, and Conceptions of the Universe* (Kluwer, 1989), chap. Going beyond Bell's theorem.

[100] O. Gühne, G. Toth, and H. Briegel, "Multipartite entanglement in spin chains," New J. of Phys. **7**, 299 (2005).

[101] M. Seevinck and J. Uffink, "Sufficient conditions for three-particle entanglement and their tests in recent experiments," Phys. Rev. A **65**, 012107 (2001).

[102] A. S. Sorensen and K. Molmer, "Entanglement and extreme spin squeezing," Phys. Rev. Lett. **86**, 4431–4434 (2001).

[103] W. Dür, G. Vidal, and J. I. Cirac, "Three qubits can be entangled in two inequivalent ways," Phys. Rev. A **62**, 062314 (2000).

[104] S. Braunstein and C. M. Caves, "Statistical distance and the geometry of quantum states," Phys. Rev. Lett. **72**, 3439 (1994).

[105] W. K. Wootters, "Statistical distance in Hilbert space," Phys. Rev. D. **23**, 357 (1980).

[106] L. Pezze and A. Smerzi, "Entanglement, Nonlinear Dynamics, and the Heisenberg Limit," Phys. Rev. Lett. **102**, 100401– (2009).

[107] P. Hyllus, W. Laskowski, K. R., S. C., W. Wieczorek, W. H., L. Pezzé, and A. Smerzi, "Fisher information and multiparticle entanglement," Phys. Rev. A **85**, 022321 (2012).

[108] D. Petz and C. Ghinea, "Introduction to quantum fisher information," in "Quantum Probability and Related Topics," , vol. 1 (2011), vol. 1, pp. 261–281.

[109] G. Tóth and I. Apellaniz, "Quantum metrology from a quantum information science perspective," Journal of Physics A: Mathematical and Theoretical **47**, 424006 (2014).

[110] H.-N. Xiong, J. Ma, W.-F. Liu, and X. Wang, "Quantum fisher information for superpositions of spin states," Quantum Info. Comput. **10**, 498–508 (2010).

[111] M. Kitagawa and M. Ueda, "Squeezed spin states." Phys.Rev. A **47**, 5138–5143 (1993).

[112] J. Ma, X. Wang, C. Sun, and F. Nori, "Quantum spin squeezing," Physics Reports **509**, 89–165 (2011).

[113] D. J. Wineland, J. J. Bollinger, W. M. Itano, and D. J. Heinzen, "Squeezed atomic states and projection noise in spectroscopy," Phys. Rev. A **50**, 67–88 (1994).

121

[114] V. Erol, F. Ozaydin, and A. Altintatas, "Analysis of entanglement measures and locc maximized quantum fisher information of general two qubit systems," Sci. Rep. **4**, 5422 (2014).

[115] A. Sen(De), U. Sen, M. Wiesniak, D. Kaszlikowski, and M. Zukowski, "Multiqubit W states lead to stronger nonclassicality than Greenberger-Horne-Zeilinger states," Phys. Rev. A **68**, 062306– (2003).

[116] J. Joo and Y.-J. Park, "Quantum secure communication via a W state," J. Korean Phys. Soc. **46**, 763–768 (2005).

[117] H. Häffner, W. Hänsel, C. F. Roos, J. Benhelm, D. Chek-al kar, M. Chwalla, T. Körber, U. D. Rapol, M. Riebe, P. O. Schmidt, C. Becher, O. Gühne, W. Dür, and R. Blatt, "Scalable multiparticle entanglement of trapped ions," Nature **438**, 643–646 (2005).

[118] A. Gaetan, Y. Miroshnychenko, T. Wilk, A. Chotia, M. Viteau, D. Comparat, P. Pillet, A. Browaeys, and P. Grangier, "Observation of collective excitation of two individual atoms in the Rydberg blockade regime," Nat Phys **5**, 115–118 (2009).

[119] W. Wieczorek, R. Krischek, N. Kiesel, P. Michelberger, G. Toth, and H. Weinfurter, "Experimental Entanglement of a Six-Photon Symmetric Dicke State," Phys. Rev. Lett. **103**, 020504– (2009).

[120] J. Volz, R. Gehr, G. Dubois, J. Esteve, and J. Reichel, "Measurement of the internal state of a single atom without energy exchange," Nature **475**, 210–213 (2011).

[121] L. M. K. Vandersypen and I. L. Chuang, "NMR techniques for quantum control and computation," Rev. Mod. Phys. **76**, 1037–1069 (2005).

[122] A. Muller, E. B. Flagg, J. R. Lawall, and G. S. Solomon, "Ultrahigh-finesse, low-mode-volume Fabry–Perot microcavity," Opt. Lett. **35**, 2293–2295 (2010).

[123] B. Brandstätter, A. McClung, K. Schuppert, B. Casabone, K. Friebe, A. Stute, P. O. Schmidt, C. Deutsch, J. Reichel, R. Blatt, and T. E. Northup, "Integrated fiber-mirror ion trap for strong ion-cavity coupling," Rev. Sci. Instr. **84**, 123104 (2013).

[124] M. Uphoff, M. Brekenfeld, G. Rempe, and S. Ritter, "Frequency splitting of polarization eigenmodes in microscopic Fabry-Perot cavities," New J. Phys. **17**, 013053 (2015).

[125] H. Mabuchi, J. Ye, and H. Kimble, "Full observation of single-atom dynamics in cavity QED," Applied Physics B: Lasers and Optics **68**, 1095–1108 (1999).

[126] F. Bielsa, A. Dupays, M. Fouche, R. Battesti, C. Robiliard, and C. Rizzo, "Birefringence of interferential mirrors at normal incidence," Appl. Phys. B. **97**, 457–463 (2009).

[127] T. W. Lynn, "Measurement and Control of individual Quanta in Cavity QED," Ph.D. thesis, California Institute of Technology (2003).

[128] D. Hunger, "Herstellung und Charakterisierung von Faserresonatoren hoher Finesse," Master's thesis, Ludwig-Maximilians-Universitat Muenchen (2005).

[129] D. Hunger, C. Deutsch, J. Barbour, , R. Warburton, and J. Reichel, "Laser microfabrication of concave, low-roughness features in silica," AIP Advances **2**, 012119 (2012).

[130] F. Brandi, F. Della Valle, A. De Riva, P. Micosse, F. Perrone, C. Rizzo, G. Ruoso, and G. Zavattini, "Measurement of the phase anisotropy of very high reflectivity interferential mirrors," Appl. Phys. B. **65**, 351–355 (1997).

[131] S. Moriwaki, H. Sakaida, T. Yuzawa, and N. Mio, "Measurement of the residual birefringence of interferential mirrors using fabry-perot cavity," Appl. Phys. B. **65**, 347–350 (1997).

[132] X. B. Wang, J. Q. You, and F. Nori, "Quantum entanglement via two-qubit quantum Zeno dynamics," Phys. Rev. A **77**, 062339 (2008).

[133] S. Maniscalco, F. Francica, R. L. Zaffino, N. L. Gullo, and F. Plastina, "Protecting Entanglement via the Quantum Zeno Effect," Physical Review Letters **100**, 090503 (2008).

[134] R. Rossi, K. M. Fonseca Romero, and M. C. Nemes, "Semiclassical dynamics from Zeno-like measurements," Phys. Lett. A **374**, 158 (2009).

[135] X. Q. Shao, L. Chen, S. Zhang, and K.-H. Yeon, "Fast CNOT gate via quantum Zeno dynamics," J. Phys. B **42**, 165507 (2009).

[136] Z. Shi, Y. Xia, W. H.Z., and J. Song, "One-step preparation of three-particle Greenberger-Horne-Zeilinger state via quantum Zeno dynamics," Eur. Phys. J. D **66**, 127 (2012).

[137] M. H. Schleier-Smith, I. D. Leroux, and V. Vuletić, "Squeezing the collective spin of a dilute atomic ensemble by cavity feedback," Phys. Rev. A **81**, 021804– (2010).

[138] J. Appel, P. J. Windpassinger, D. Oblak, U. B. Hoff, N. Kjærgaard, and E. S. Polzik, "Mesoscopic atomic entanglement for precision measurements beyond the standard quantum limit," PNAS **106**, 10960–10965 (2009).

[139] T. Wilk, S. C. Webster, A. Kuhn, and G. Rempe, "Single-Atom Single-Photon Quantum Interface," Science **317**, 488–490 (2007).

[140] M. Steiner, H. Meyer, C. Deutsch, J. Reichel, and M. Köhl, "A single ion coupled to an optical fiber cavity," Phys. Rev. Lett. **110**, 043003 (2013).

[141] N. Schlosser, G. Reymond, and P. Grangier, "Collisional blockade in microscopic optical dipole traps," Phys. Rev. Lett. **89**, 023005 (2002).

[142] F. Dimer, B. Estienne, A. S. Parkins, and H. J. Carmichael, "Proposed realization of the Dicke-model quantum phase transition in an optical cavity QED system," Phys. Rev. A **75**, 013804–14 (2007).

[143] N. Lambert, C. Emary, and T. Brandes, "Entanglement and the phase transition in single mode superradiance," Phys.Rev.Lett **92**, 073602 (2004).

[144] D. Steck, "Rubidium 87 D line data," http://steck.us/alkalidata (revision2.1.4, 23 December 2010) (2001).

[145] U. Schünemannn, H. Engler, R. Grimm, W. M., and Z. M., "Simple scheme for tunable frequency offset locking of two lasers," Rev. Sci. Instr. **70**, 242–243 (1999).

[146] G. Ritt, G. Cennini, C. Geckeler, and M. Weitz, "Laser frequency offset locking using a side of filter technique," Applied Physics B **79**, 363–365(3) (2004).

[147] N. Vansteenkiste, P. Vignolo, and A. Aspect, "Optical reversibility theorems for polarization: application to remote control of polarization," J. Opt. Soc. Am. A **10**, 2240–2245 (1993).

Acknowledgements

This thesis is the result of over three years of teamwork and I would like to give credit to all those who have contributed to its success.

First of all, I thank my supervisor Jakob Reichel who has provided feedback, ideas and inspiration at all stages of the thesis. I have highly appreciated his curiosity, hands-on approach and the constant challenge to comprehend.

The QZD experiments were carried out together with my post-doc Giovanni Barontini. It is a pleasure to acknowledge the commitment, motivation and direction he brought to this part of my work. Without him, making and keeping the FFP setup run would certainly have been less successful and not as much fun.

I am very grateful to Jérôme Estève whose insight and knowledge (and programming) have helped greatly, especially throughout the QZD work.

Special thanks go to my predecessor Florian Haas for getting us started on the FFP setup and the QZD experiments.

My very special thanks go to Konstantin Ott. We have shared both the highlights and low points of working with fibre cavities and his attentiveness, resourcefulness and humour have helped at all times. I am happy to see our efforts continue with the impressive progress he and Sébastien have achieved in terms of fibre fabrication.

The time of my PhD (just as the master's thesis before) was spent in the company of amazing colleagues. Thanks to all the members of the atom chips group, past and present, and especially Sébastien Garcia, Claire Lebouteiller, Benjamin Besga, Cyril Vaneph, Francesco Ferri, Eckhard Wallis as well as Romain Long, for their help and the good times.

I thankfully acknowledge Jean Hare for his help and advice in organisational matters throughout the doctorate.

The administrative and technical services of the lab deserve recognition for having given their best to facilitate our work.

Finally, I would like to thank my family for having given me all the opportunities and support I could wish for.

I offer my thanks to my wonderful wife Mira for her love, support, help and patience throughout the years.